Chem Soc Rev

ROYAL SOCIETY OF CHEMISTRY

REVIEW ARTICLE

View Article Online
View Journal

Cite this: DOI: 10.1039/c9cs00806c

Advances in metal–organic framework coatings: versatile synthesis and broad applications

Jiashen Meng,†[a] Xiong Liu,†[a] Chaojiang Niu,[a] Quan Pang,[b] Jiantao Li,[a] Fang Liu,[a] Ziang Liu[a] and Liqiang Mai*[a]

Metal–organic frameworks (MOFs) as a new kind of porous crystalline materials have attracted much interest in many applications due to their high porosity, diverse structures, and controllable chemical structures. However, the specific geometrical morphologies, limited functions and unsatisfactory performances of pure MOFs hinder their further applications. In recent years, an efficient approach to synthesize new composites to overcome the above issues has been achieved, by integrating MOF coatings with other functional materials, which have synergistic advantages in many potential applications, including batteries, supercapacitors, catalysis, gas storage and separation, sensors, drug delivery/cytoprotection and so on. Nevertheless, the systemic synthesis strategies and the relationships between their structures and application performances have not been reviewed comprehensively yet. This review emphasizes the recent advances in versatile synthesis strategies and broad applications of MOF coatings. A comprehensive discussion of the fundamental chemistry, classifications and functions of MOF coatings is provided first. Next, by modulating the different states (*e.g.* solid, liquid, and gas) of metal ion sources and organic ligands, the synthesis methods for MOF coatings on functional materials are systematically summarized. Then, many potential applications of MOF coatings are highlighted and their structure–property correlations are discussed. Finally, the opportunities and challenges for the future research of MOF coatings are proposed. This review on the deep understanding of MOF coatings will bring better directions into the rational design of high-performance MOF-based materials and open up new opportunities for MOF applications.

Received 29th December 2019

DOI: 10.1039/c9cs00806c

rsc.li/chem-soc-rev

1. Introduction

Metal–organic frameworks (MOFs) as a new class of porous crystalline materials have attracted tremendous interest in recent decades.[1,2] Generally, MOFs consist of two main components of metal ions or clusters and organic ligands, which are assembled *via* well-defined coordination bonds.[3] By converting

[a] State Key Laboratory of Advanced Technology for Materials Synthesis and Processing, Wuhan University of Technology, Wuhan 430070, China. E-mail: mlq518@whut.edu.cn

[b] Department of Energy and Resources Engineering, and Beijing Innovation Center for Engineering Science and Advanced Technology, Peking University, Beijing 100871, China

† These authors contributed equally to this work.

Jiashen Meng

Jiashen Meng received his BS degree from Wuhan University of Technology in 2015 and he is currently working toward his PhD degree in Materials Science at Wuhan University of Technology. From 2018 to 2019, he was a visiting PhD student in Prof. Donald Sadoway's group at Massachusetts Institute of Technology. His current research focuses on developing new nanomaterials and chemistry for energy conversion and storage devices.

Xiong Liu

Xiong Liu obtained his BS degree from Wuhan University of Technology in 2016. He is now a PhD candidate with Prof. Dongyuan Zhao and Prof. Liqiang Mai. His research interests focus on the controllable structure design for energy storage/conversion and reconstruction chemistry in electrocatalysis.

the species of metal ions or clusters and organic ligands, thousands of MOFs have been successfully created by researchers.[4–7] Due to their unique structures, the MOF materials possess ultrahigh porosity (around 90% free volume) and surface area (up to 6000 $m^2 g^{-1}$), uniform but tunable pores (0.5 to 2 nm), fully exposed active sites, tunable morphologies and abundant compositions, which show great significance in many applications.[8–11] For example, by rationally modulating their size and affinity of these pores, MOFs are used as selective molecular sieves for gas separation, which allow specific molecules to pass but not others. Furthermore, choosing specific metal ions and/or functionalized organic linkers endows new MOFs with unique properties, such as catalytic MOFs based on active metal ions and/or organic linkers, photoactive MOFs based on light-harvesting linkers, magnetic MOFs based on magnetic metal ions, bio-mimicking MOFs based on biomolecule-based linkers, and conductive MOFs based on conductive linkers.[12–20] These functional MOFs show great potential in the areas of catalysis, gas separation and storage, supercapacitors and drug delivery. Besides, because of their intrinsic low chemical stability and poor electronic conductivity, most MOFs have also been selected as precursors or templates to synthesize various carbon-based structures for electrochemical energy-related applications.[21–28] However, the specific geometrical morphologies, limited functions and unsatisfactory performances of pure MOFs hinder their further applications. Therefore, constructing unique MOF-based composite materials with high performance is a great challenge for future fundamental research and practical applications.

In recent years, intensive efforts have been made to combine MOFs with other functional materials (*e.g.* inorganic compounds, carbon materials, substrates, metal nanocrystals, polymers, biomolecules) to form novel composites.[2,29–32] The obtained composites not only inherit the merits of MOFs and other materials, but also have additional advantages from the interactions between them. It is believed to be one of the most effective ways to design and construct well-defined MOF coated functional composites to achieve synergistic properties of core materials and MOF coatings for multifunctional applications, including batteries, supercapacitors, catalysis, gas storage and separation, sensors, hydrogenation, drug delivery/cytoprotection and so on.[30,33–38] For example, Lu *et al.* achieved a controlled and efficient strategy to encapsulate various nanoparticles (*e.g.* Pt, Fe_3O_4, $NaYF_4$ and CdTe) within a zeolitic imidazolate framework (ZIF-8).[39] The obtained nanoparticle/ZIF-8 composites exhibited outstanding catalytic, magnetic and optical properties compared to the single component, which were attributed to the synergistic effect of porous molecular sieving behavior from the ZIF-8 matrix and functional characteristics of isolated nanoparticles. Li *et al.* reported unique Pd nanocrystals confined in a MOF (HKUST-1, copper(II) 1,3,5-benzenetricarboxylate), displaying much higher capacity and speed of hydrogen storage than pure Pd nanocrystals.[40] The unique MOF coating can significantly enhance the surface/bulk reactivity of Pd nanocrystals, thus accelerating their reactivity with hydrogen. Recently, Falcaro *et al.* reported crystalline MOF (ZIF-8) protective coatings for living cells, and further demonstrated that functional MOF coatings efficiently controlled molecular trafficking to the cell cytoplasm and simultaneously induced an artificial hibernation state to prevent cell division.[41] These cases demonstrate that MOF coatings play important roles in the application performances of the prepared integrated composites. Therefore, developing efficient strategies to combine high-quality functional MOF coatings with other materials is highly desired and of great significance to achieve the as-prepared composites with excellent application properties. It is also noted that several recent reviews have focused on the synthesis methods and/or specific applications of pure MOFs and MOF-derived materials.[34,42–49] To our best knowledge, the systemic synthesis strategies for MOF coatings on functional materials and the relationships between their structures and application performances are not yet reviewed comprehensively at present.

According to the statistical analysis in Fig. 1, the number of publications involving 'metal organic frameworks' has rapidly increased, which indicates that the research on MOFs is in full swing during the past decade. Meanwhile, the number of publications on MOF coatings or shells has similarly increased especially in the last five years. Despite being in their infancy in terms of the number of published papers, the recent research progress has already shown that MOF coatings are promising for many potential applications. In this regard, this review aims to systematically summarize the recent advances in the versatile synthesis strategies and broad potential applications of MOF coatings. Particular emphasis is first placed on deep understanding of the fundamental chemistry, classifications and functions of MOF coatings. According to the different states (*e.g.* solid, liquid and gas) of metal ion sources and organic linkers, several synthesis strategies for MOF coatings are summarized and discussed. Then, many potential applications of MOF coatings are highlighted and their structure–property correlations are discussed in detail. Finally, a summary and an outlook are proposed to

Liqiang Mai

Liqiang Mai is Changjiang Scholar Chair Professor of Materials Science and Engineering at Wuhan University of Technology (WUT). He is the winner of the National Natural Science Fund for Distinguished Young Scholars and Fellow of the Royal Society of Chemistry. He received his PhD from WUT in 2004 and carried out his postdoctoral research with Prof. Zhong Lin Wang at Georgia Institute of Technology in 2006–2007. He worked as an advanced research scholar with Prof. Charles M. Lieber at Harvard University in 2008–2011 and Prof. Peidong Yang at University of California, Berkeley in 2017. His current research interests focus on new nanomaterials for electrochemical energy storage and micro/nano energy devices.

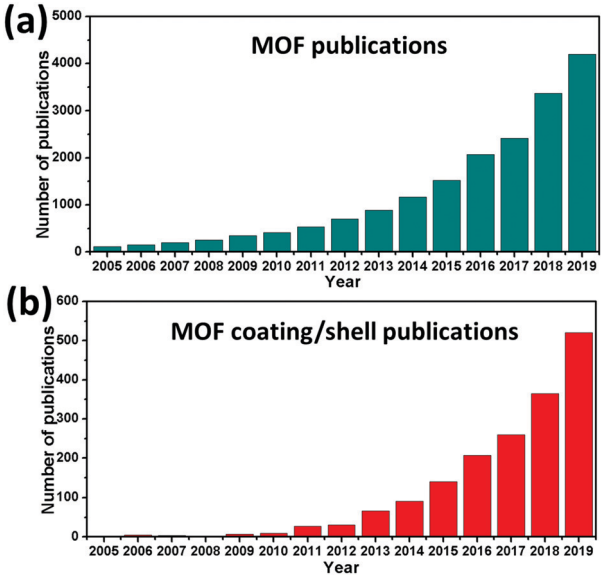

Fig. 1 The number of publications per year from Web of Science: (a) "MOF" and (b) "MOF coating/shell".

provide a full picture of the future developments of MOF coatings within the field.

2. Fundamental chemistry, classifications and functions of MOF coatings

MOF coatings play an important role in the whole performances of the new composites. Moreover, their macroscopic geometrical morphologies which are distinguishable from bulk MOFs endow the obtained composites with new synergistic advantages for many potential applications. In this section, the fundamental chemistry of MOF coatings is described firstly, and their structural characteristics are also highlighted. On the basis of different kinds of the incoming materials, the classifications of MOF coatings are then discussed. Finally, the comprehensive functions of MOF coatings are summarized.

2.1 Fundamental chemistry of MOF coatings

Generally, MOFs are constructed from bridging organic linkers and metal ions or clusters by coordination bonds. The organic linkers commonly contain carboxylates, phosphonates, sulfonates, and heterocyclic compounds, which can be bi-, tri-, tetratopic or other linkers.[3] Notably, it has been experimentally reported that metal ions or clusters can perform as secondary building units (SBUs), mainly including transition metals, main-group metals, alkali metals, alkaline earth metals, lanthanides and actinides. In addition, the number of metal atoms in these SBUs varies from one to eight or more. Combining diverse organic linkers and various metal ions or SBUs endows the resulting MOFs with a wide range of framework topologies. During the past few decades, more than 20 000 different MOFs have been reported and studied. MOF coatings inherit all the merits of MOFs. Several specific and important properties of MOF coatings are discussed as follows:

(1) Tunable species and structures. By using different metal ions/clusters and organic ligands, a series of MOF coatings with rich species and precise structures can be obtained *via* well-defined coordination reactions. In addition, abundant functional groups in organic ligands facilitate the heterogeneous nucleation and growth of MOF coatings on other core materials by weak interactions in solutions.

(2) Uniform and controlled pore size. Owing to their crystallinity, MOF coatings simultaneously consist of uniform and periodic cavities distributed throughout their three-dimensional (3D) matrices. For example, a typical MOF-5 is assembled *via* coordination bonds between Zn_4O tetrahedra and 1,4-benzenedicarboxylate (1,4-BDC) ligands, and possesses a 3D cubic network structure with interconnected pores of 12 Å diameter. By simply altering the organic ligands from 1,4-BDC to 2-methylimidazole (Hmim), the corresponding transformation of the MOF product is from MOF-5 to ZIF-8 due to different connection ways. ZIF-8 shows an extended 3D open framework with topologies similar to that of inorganic zeolites, which has large pores of 11.6 Å diameter connected through small apertures of 3.4 Å. On the other hand, modulating the SBUs from Zn_4O to Cr_3O results in the formation of material sofistitute Lavoisier frameworks (MIL-101), which exhibit a zeotype cubic structure and a hierarchy of extra-large pore size of approximately 30 to 34 Å diameter. Therefore, the atomic-level uniformity, tunability and accuracy of the pore size endow MOF coatings with precise control in practical applications.

(3) Ultrahigh surface area. The surface area of MOFs generally ranges from 1000 to 10 000 $m^2\ g^{-1}$ by altering the organic linkers and metal ions/clusters. The surface area values of the representative MOF-5, ZIF-8 and MIL-101 are about 3800, 1947 and 5900 $m^2\ g^{-1}$, respectively.[50,51] Therefore, such MOF coatings can efficiently endow the composites with high surface area.

(4) Multifunctional and abundant exposed active sites. Based on the previous discussions, tuning functional metal ions/clusters and/or organic linkers results in MOF coatings with multifunctional properties, such as catalytic selectivity and activity, photoactivity, conductivity and magnetism. For example, Jahan *et al.* reported an efficient oxygen reduction electrocatalyst based on an iron–porphyrin framework coating on pyridine-functionalized graphene.[52] The introduction of pyridine-functionalized graphene can improve the electron conductivity and enhance the electrochemical charge transfer rate of iron–porphyrin framework coatings. Moreover, the porous structure of MOF coatings facilitates the diffusion of reactants and products through MOF channels, making MOFs an ideal platform to efficiently expose their catalytic active sites.

(5) Good contact with other functional materials. Good contact with other functional materials in MOF coatings has a great influence on the practical performances of composites. Lu *et al.* demonstrated that a catalyst of uniform Pd nanocrystals confined in ZIF-8 coating (Pd/ZIF-8) exhibited hydrogenation of linear *n*-hexene molecules and no catalytic activity of the sterically more demanding *cis*-cyclooctene owing to the small pore aperture (3.4 Å) of ZIF-8, indicating its high selectivity.[39] However, the Pd/ZIF-8 hybird composite had a residual activity for *cis*-cyclooctene

hydrogenation, showing poor selectivity. This difference was mainly attributed to the formation of naked Pd nanoparticles on the surfaces of the Pd/ZIF-8 hybird composite, thus confirming the importance of good contact within MOF coatings. Therefore, developing mild, operationally simple, low-cost, and high-yield methods is highly desired and of great importance for practical applications of MOF-based materials. The systemic synthesis strategies of MOF coatings are summarized and discussed in detail in Section 3.

2.2 Classifications of MOF coatings

As discussed above, MOF coatings have abundant species and diverse structures. It seems difficult to classify them just based on their species and structures. However, the species of the integrated functional materials are much less than those of MOF coatings. Currently, the already reported integrated functional materials include inorganic compounds, carbon materials, hard substrates, metal nanocrystals, MOF crystals, polymers, molecules, biomaterials and so on, which endow the MOF-based composites with multifunctional practical applications. For example, Huang *et al.* achieved uniform MOF coatings on MoS_2 nanosheets as a memory device, which displayed a write-once-read-many-times memory effect with a high ON/OFF ratio and a long operating lifetime.[53] He *et al.* constructed uniform MOF shell-derived carbon confined SnO_2/Co nanocubes with highly reversible and stable lithium storage.[54] Therefore, the introduction of uniform and thin MOF coatings on diverse nanostructured inorganic compounds endows the obtained composites with excellent application properties. In addition, Tang *et al.* designed and constructed core–shell ZIF-8@ZIF-67 crystals as precursors to obtain selectively functionalized hybrid carbon materials with a distinguishing specific capacitance, demonstrating an efficient "MOF plus MOF" strategy.[55] In this review, based on the different features of other functional materials, the MOF coatings have been classified into six main groups: MOF coatings on inorganic compounds, MOF coatings on carbon materials, MOF coatings on substrates, MOF coatings on metal nanocrystals, MOF coatings on molecules and polymers and MOF coatings on biomaterials (Fig. 2). Furthermore, these functional MOF-coated composites show great potential in many practical applications, including batteries, supercapacitors, electrocatalysis, gas separation, gas adsorption and storage, sensors, photocatalysis, hydrogenation and drug delivery/cyto-protection. These detailed applications will be discussed and commented in Section 4.

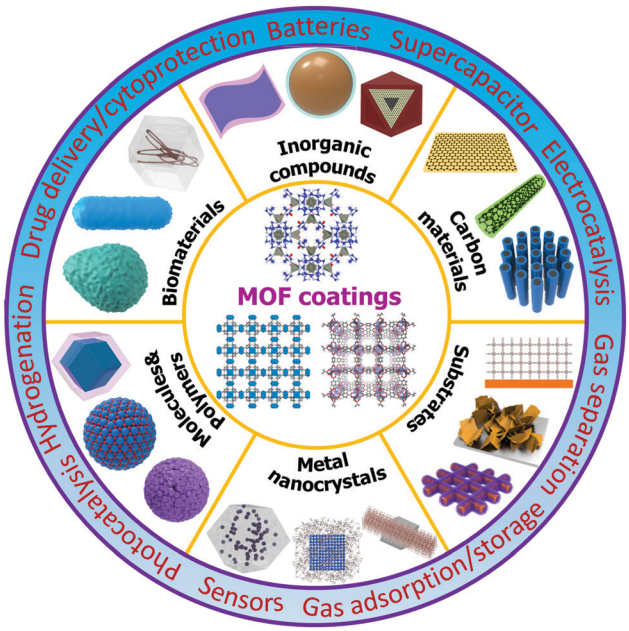

Fig. 2 A summary of the classifications and potential applications of MOF coatings based on different integrated materials (*e.g.* inorganic compounds, carbon materials, substrates, metal nanocrystals, polymers, molecules and biomaterials).

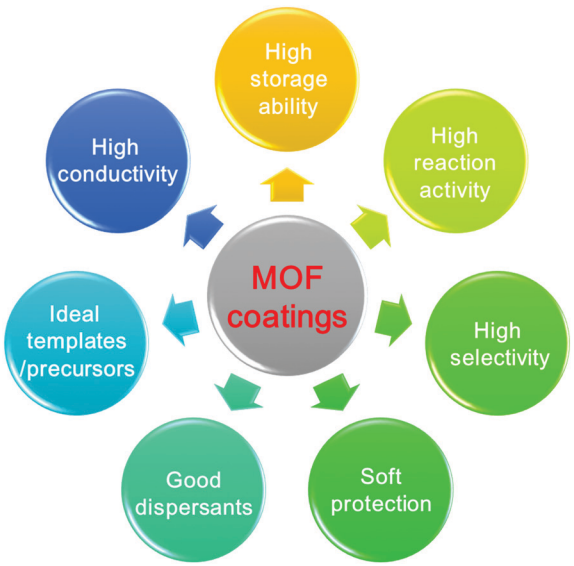

Fig. 3 A summary of the functions of MOF coatings.

2.3 Functions of MOF coatings

At present, state-of-the-art MOF materials still manifest themselves as better than other porous materials in terms of specific surface area, species, precise structures and porosity. Because of their different species and structures, different MOF coatings endow the resulting composites with multifunctional properties, which have a great influence on their practical applications. Therefore, the main functions of MOF coatings are summarized and discussed in detail in this section (Fig. 3).

(1) High storage ability. Generally, the gas storage capacity of porous materials is directly proportional to their pore volume and/or specific surface area. MOFs possess an intrinsic high surface area and high porosity, thus showing high storage ability. For example, two typical MOF-210 and Al-soc-MOF-1 exhibited extremely high Brunauer–Emmett–Teller (BET) surface areas of 6240 and 5585 $m^2\ g^{-1}$, thus resulting in high gravimetric storage capacities of 0.410 and 0.414 $g\ g^{-1}$ at room temperature and 65 bar, respectively. In addition, the introduction of functional groups into the pore surfaces of MOFs has been demonstrated to greatly improve their storage ability. Li *et al.* achieved a new and well-designed MOF, namely, UTSA-76, with pyrimidine groups on

the linkers, exhibiting high volumetric methane storage capacity.[56] The high uptake property is mainly attributed to the immobilized Lewis basic N sites and dynamic linkers in UTSA-76. Moreover, Sheberla *et al.* developed a new type of conductive MOF (Ni_3(2,3,6,7,10,11-hexaiminotriphenylene)$_2$ with high electron conductivity, an open porous structure and a high surface area, $Ni_3(HITP)_2$), exhibiting an ultrahigh areal capacity that exceeded that of most carbon-based materials.[57] Therefore, unique MOF coatings with delicate structures and functional groups show high storage ability in practical applications, such as gas storage, energy storage, catalysis, and drug/cell delivery.

(2) High reaction activity. MOFs are a class of promising materials for diverse heterogeneous catalysis. Their intrinsic open frameworks, tunable species and fully exposed active sites endow these functional MOFs with high reaction activity. Recently, Li *et al.* successfully synthesized a series of Fe/Ni-based MOFs with modulated molar ratios directly adopted as efficient oxygen evolution reaction (OER) catalysts.[58] After component optimization, the obtained trimetallic Fe/$Ni_{2.4}$/$Mn_{0.4}$-MIL-53 displayed excellent OER performance compared with most reported OER electrocatalysts, confirming high reaction activity. The synergistic effect of the mixed metals in MOFs was demonstrated to efficiently modulate the electronic environment of the active metal sites, thus resulting in high reaction activity for the catalytic OER. Furthermore, Duan *et al.* fabricated a nickel–iron-based MOF array grown on substrates with superior OER performance.[59] In addition, the abundant pores and tunable pore structures give access to even large reactant molecules diffusing into the pores of MOFs, and then large molecular products can move out of the network. Henschel *et al.* demonstrated a chromium based MOF (MIL-101) consisting of m3-oxo bridged chromium(III)-trimers crosslinked by terephthalate groups, exhibiting a high product yield of 98.5% towards the addition of trimethylsilylcyanide to benzaldehyde.[60] The high reaction activity is attributed to unsaturated pseudo-octahedral coordination structures around each chromium atom in MIL-101, making chromium accessible for potential reactants. The difficult reduction of chromium(III) also results in the stability of MIL-101 during the reaction processes. Therefore, MOF coatings with specific active sites possess high reaction activity for many applications.

(3) High selectivity. MOFs are a class of crystalline nanoporous materials with well-defined pore structures and tunable chemical properties. The nanopores in MOFs provide efficient confinement effects and shape selectivity. Furthermore, encapsulating well-defined nanoparticle catalysts within nanoporous MOF coatings to form a core–shell nanostructure can efficiently enhance the selectivity and/or reactivity of catalysts. Generally, the nanopores in MOF coatings ensure the accessibility of small-sized reactant molecules to the active metal surfaces rather than large-sized molecules. For example, Khajavi *et al.* introduced homogeneous Pt nanoparticles of $\sim$4 nm diameter into MIL-101 with good contact with the Cr trimers in a core–shell configuration.[61] The obtained catalyst was applied in the selective hydrogenation of olefin mixtures. 1-Octene is selectively hydrogenated over 1-hexadecene (the octene/hexadecane selectivity ratio is calculated to be 28). This high selectivity is mainly attributed to the difference in the chain length of substrate molecules and the relative molecular masses, thus resulting in different mass transport limitations in the MOF pores. In addition, Ma *et al.* successfully constructed ZIF-8 membranes on a porous support, exhibiting a high mixture separation factor for propylene over propane and a high propylene flux.[62] Therefore, the high selectivity of MOF coatings provides precise chemistry and control for their catalytic and separation applications.

(4) Soft protection. Compared with other traditional drug carriers (*e.g.* inorganic mesoporous silica, quantum dots, metal nanoparticles and organic micelles), MOFs possess significant advantages of tunable pore size, tailorable composition and structure, high porosity and high drug loading, improved biocompatibility and easy biodegradation. These merits make MOFs promising and flexible protective coatings for drug/cargo delivery. Liang *et al.* encapsulated biomacromolecules (*e.g.* proteins, enzymes and DNA) within protective MOF coatings.[63] The obtained biocomposite was stable under normal conditions. Furthermore, by simply modulating the environmental pH, the biomacromolecules as a bioactive cargo can controllably be released from their protective MOF coatings. Therefore, MOF coatings provide flexible protection to deliver functional biomacromolecules for many bioapplications.

(5) Good dispersants. The incorporation of nanoparticles into MOF coatings attracts much attention because of their synergistic chemical and physical properties. As discussed above, it is important to obtain well-defined nanoparticle/MOF composites with good contact for practical applications. Due to their abundant and periodic cavities, MOFs are used as templates and good dispersants to store small and naked nanoparticles or clusters in their cavities, thus resulting in the formation of nanoparticle/MOF composites. On the other hand, the grown MOFs act as good dispersants to spatially confine the presynthesized large-sized nanoparticles in their framework matrix rather than their cavities. For example, Lu *et al.* reported surfactant-capped nanostructures of various sizes, shapes and compositions encapsulated in ZIF crystals.[39] In addition, the variation of the synthesis conditions efficiently controls the spatial distribution of nanoparticles within the MOF matrix.

(6) Ideal templates/precursors for MOF derivatives. Because of their both organic and inorganic species, MOFs emerged as ideal templates and/or precursors for nanostructured materials such as porous metal oxides, metal nanoparticles, porous carbons, and their composites. For example, Li *et al.* developed an ordered bcc copper–palladium nanoalloy through the direct decomposition of a Pd nanoparticle@HKUST-1 composite material under H_2. Such starting composite possesses the intimate mixing of the Pd and Cu atoms, efficiently accelerating the alloy reaction. Moreover, Wang *et al.* prepared ZIF-8 with single ferrocene molecules confined within its cavities (Fc@ZIF-8), and directly utilized the as-prepared Fc@ZIF-8 as a precursor to obtain porous single-atom Fe embedded nitrogen-doped carbon frameworks during the high-temperature pyrolysis.[64] The resulting single-atom catalyst exhibited excellent oxygen reduction performance, outperforming the commercial Pt/C. Therefore, thermal conversions

of MOF coatings offer a promising tool for synthesizing these functional nanomaterials compared with conventional methods.

(7) High conductivity. Generally, MOFs are porous materials with tunable structures and high surface areas, which are thought as promising candidates for high-capacitance electrochemical capacitors. However, the poor conductivity in most MOFs significantly limits their further practical applications. To improve the high electron conductivity of MOF-based materials, there are two common approaches as follows. One typical method is to design and construct conductive MOFs by choosing conjugated conductive linkers. Sheberla *et al.* reported conductive $Ni_3(HITP)_2$ with bulk electrical conductivity higher than 5000 S m^{-1}, displaying high areal capacitance and good stability.[57] Furthermore, Li *et al.* fabricated conductive MOF nanowire arrays on carbon paper to make full use of its nanostructure, high porosity and high conductivity, and demonstrated its highest areal capacitance and best rate performance for supercapacitors.[65] Conductive MOFs show great potential in their direct applications in energy storage and conversion.[66] The electron-conducting mechanism of conductive MOFs is based on the delocalization of charge in their frameworks. To realize the rational design of conductive MOFs, effective overlap between the frontier orbitals of the redox-active metal centres and the bridging ligands (*e.g.* π–π and π–d) is highly desired.[67] Generally, the selected organic ligands possess abundant π-conjugated groups. Another efficient strategy is to convert MOFs into MOF-derived carbon-based materials after high-temperature pyrolysis. Recently, our group developed a facile two-step solid-state reaction method to construct uniform MOF shell-derived carbon confined SnO_2/Co nanocubes, exhibiting fast and stable lithium storage performance.[54] In brief, developing high-conductivity MOF coatings is of great significance for high-performance energy related applications.

3. Versatile synthesis strategies for MOF coatings

The performances of the obtained MOF coatings are strongly influenced by their spatial distribution and nanostructures of the incorporated functional materials as well as their guest–host interactions. Different from conventional MOF nanoparticles, constructing high-quality and uniform MOF coatings on functional materials requires more science and technology. One straightforward approach is to use the presynthesized MOF matrices to confine reduced or decomposed metal nanoparticles in their cavities.[68] For example, Zhu *et al.* reported a liquid-phase concentration-controlled reduction strategy to introduce the AuNi alloy nanoparticles (NPs) into the pores of MIL-101 and control their size and location by reduction of the Au^{3+} and Ni^{2+} precursors.[69] The obtained architecture displayed the uniform 3D distribution of the ultrafine AuNi NPs encapsulated in the pores of MIL-101, which exhibited exceedingly high activity for hydrogen generation. Although this "ship-in-a bottle" approach is relatively simple and results in good contact and high dispersibility of metal nanoparticles, the control of shape and composition of the incorporated metal nanoparticles is greatly challenging.[70] Even, this method is more difficult to apply to other large-sized, complex structured incorporated materials. Another efficient approach is to control the assembly of MOF precursors to realize the formation of MOF coatings on other functional materials.[26,71–73] During the MOF formation process, the size, shape, and composition of the incorporated materials can be fully preserved and well defined, confirming the great potential of this "bottle-around-ship" approach for MOF coatings. Therefore, considering its superiority, this general and efficient "bottle-around-ship" approach is emphasized in this review. In this section, according to the modulation of different states of metal ion sources (*e.g.* solid, liquid and gas) and organic ligands (*e.g.* solid, liquid and gas), five main methods for the synthesis of MOF coatings have been systematically summarized and highlighted, including liquid–liquid, solid–liquid, solid–solid, solid–gas and gas–gas synthesis methods (Fig. 4). Furthermore, these strategies are discussed in detail in the following subsections. Because of difficult control of solid nanostructured organic ligands, other methods, including liquid–solid or gas–solid synthesis methods, are not suited for the synthesis of nanostructured MOF coatings. Even though the core–shell nanostructures with solid organic ligand cores and MOF coatings can be obtained, their further applications are still limited by their inactive and unstable cores. In addition, liquid–gas or gas–liquid synthesis methods for MOF coatings are too difficult to control because of their unstable interfacial coordination reactions.

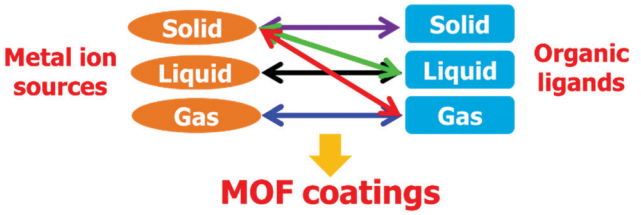

Fig. 4 A summary of the synthesis strategies of MOF coatings based on different states of metal ion sources and organic ligands, including liquid–liquid, solid–liquid, solid–solid, solid–gas and gas–gas synthesis methods.

3.1 Liquid–liquid synthesis method

The liquid–liquid synthesis method is a main approach to obtain MOF coatings, in which the as-prepared other functional materials are introduced into the precursor solution of a MOF. In the precursor solution, because of the coordination reactions between metal ions and organic ligands in liquid solution, the homogeneous nucleation and growth of MOF crystals occur on the surfaces of the incorporated materials, resulting in the formation of well-defined MOF coatings.[74–76] The incorporated materials have diverse structures and belong to abundant categories, including inorganic compounds, carbon materials, hard substrates, metal nanocrystals, MOF crystals, polymers, molecules, biomaterials and so on.[77–83] The size, structure, chemical composition and specific property of the incorporated materials are well preserved in the resulting composites. The synergistic effects between core incorporated materials and MOF coatings endow the composites with great potential in

practical applications. This straightforward liquid–liquid synthesis method provides a facile approach towards the synthesis of MOF coatings, which exhibits many advantages of simple manipulation, abundant MOF coatings, various incorporated materials and low cost. However, because the MOFs tend to self-nucleate and form individual particles in precursor solutions, accurately controlling the heterogeneous nucleation and growth of MOFs on the surfaces of the incorporated materials is still a great challenge, especially for multilevel and complex nanostructures. To obtain high-quality and uniform MOF coatings, there are many synthetic parameters to be considered, mainly including solvents, precursor concentration, surface modification, temperature, and treatment time.

The above-mentioned comprehensive synthesis conditions play an important role in the successful formation of MOF coatings on other integrated materials in the precursor solution. Huang *et al.* reported a facile liquid–liquid synthesis method to realize the formation of a uniform ZIF-8 coating on various two-dimensional nanomaterials, including MoS_2 nanosheets, graphene oxide (GO), and reduced GO (rGO). Moreover, ternary core–shell nanostructures, including Pt–MoS_2@ZIF-8, Pt–GO@ZIF-8, and Pt–rGO@ZIF-8, have also been synthesized using the same procedures.[53] The formation process of nanosheet@MOF and metal NP–nanosheet@MOF hybrid structures is shown in Fig. 5a. First, the selected MoS_2 nanosheets and Pt–MoS_2 composite as examples were synthesized and then used as two-dimensional (2D) templates for MOF coatings. Second, the aqueous solutions of Hmim and zinc acetate dihydrate were mixed with the as-prepared 2D templates under ambient conditions. Because of the coordination reaction between Zn ions and Hmim, the heterogeneous nucleation and growth of MOFs occur on the surfaces of the 2D templates. This process is driven by the reduction of Gibbs free energy in the reaction system. Subsequently, the mixture was kept undisturbed for 2 h. Finally, after centrifugation, washing, and vacuum drying, uniform

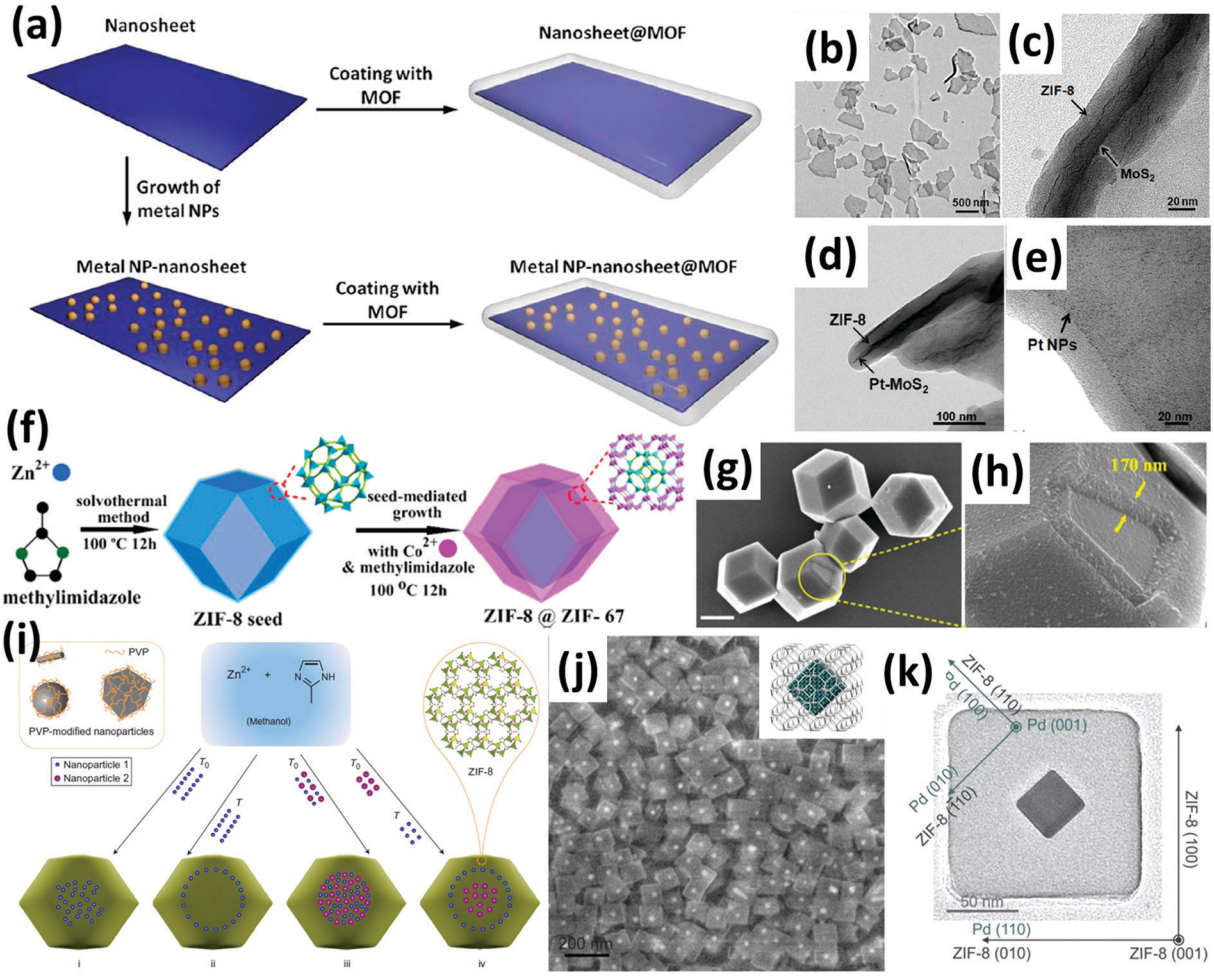

Fig. 5 (a) Schematic illustration of the formation process of nanosheet@MOF and metal NP–nanosheet@MOF hybrid structures. (b and c) TEM images of MoS_2@ZIF-8 hybrid structures. (d and e) TEM images of Pt–MoS_2@ZIF-8 hybrid structures. (f) Synthetic scheme for the preparation of core–shell ZIF-8@ZIF-67 crystals. (g and h) SEM images of core–shell ZIF-8@ZIF-67 crystals. Scale bar: 2 μm. (i) Scheme of the controlled encapsulation of nanoparticles in ZIF-8 crystals. (j) SEM image of core–shell Pd@ZIF-8 nanocomposites. The inset of (j) is a 3D modeling projection of single core–shell Pd@ZIF-8 crystals. (k) TEM image of Pd cube@ZIF-8 in [001] and [100] view directions. (a–e) Reproduced with permission from ref. 53. Copyright 2014, American Chemical Society. (f–h) Reproduced with permission from ref. 55. Copyright 2015, American Chemical Society. (i) Reproduced with permission from ref. 39. Copyright 2012, Nature Publishing Group. (j and k) Reproduced with permission from ref. 86. Copyright 2014, American Chemical Society.

ZIF-8 shell coated MoS_2 and Pt–MoS_2 nanosheets (denoted as MoS_2@ZIF-8 and Pt–MoS_2@ZIF-8) were successfully obtained. Transmission electron microscopy (TEM) was further carried out to identify the obtained structures. The low-magnification TEM image showed well-dispersed morphology-preserved nanosheets and no individual ZIF crystals, indicating the successful formation of all ZIF products on nanosheet substrates (Fig. 5b). TEM images of the curled composites displayed the embedded MoS_2 and Pt–MoS_2 cores and ZIF-8 shell, directly demonstrating their well-defined core–shell structures (Fig. 5c–e). In addition, by using this method, uniform ZIF coatings were also successfully formed on various graphene-based materials (for example, GO@ZIF-8, rGO@ZIF-8, Pt–GO@ZIF-8, and Pt–rGO@ZIF-8), confirming its wide adaption.

Besides 2D templates, Tang *et al.* reported a facile seed-mediated growth method to construct core–shell ZIF-8@ZIF-67 crystals with a 3D well-defined rhombic dodecahedral shape.[55] Because of their isoreticular structures and similar unit cell parameters, the Zn-based ZIF-8 and Co-based ZIF-67 are good candidates for the formation of the core–shell structure. First, uniform ZIF-8 seeds were synthesized by the coordination reaction of Zn^{2+} ions and Hmim in methanol solution during the solvothermal process (Fig. 5f). The good dispersion of the as-prepared ZIF-8 seeds plays an important role in the formation of uniform ZIF-67 coatings. The well-dispersed ZIF-8 crystals with a diameter of 500 nm or 4 μm were used as seeds. Subsequently, the selected ZIF-8 seeds were added into a methanol solution of $CoCl_2$. Meanwhile, the Co^{2+} preferentially bonded with Hmim units exposed on the surfaces of ZIF-8 crystals *via* the coordinative interaction, and then coordinated with additive Hmim linkers, resulting in the successful formation of ZIF-8 shells on ZIF-8 seeds. Furthermore, by modulating the feeding ratio of Co^{2+}/Zn^{2+}, the thickness of the ZIF-67 shell can be easily controlled. The core–shell ZIF-8@ZIF-67 crystals show rhombic dodecahedral morphology, which is similar to the original morphology of ZIF-8 seeds (Fig. 5g). The broken crystal indicated the uniform ZIF-67 shell with a thickness of 170 nm on the ZIF-8 seed, clearly confirming the core–shell structure (Fig. 5h). The unique well-defined core–shell structure is mainly attributed to the good lattice match between ZIF-67 and ZIF-8, which is beneficial for epitaxial growth. However, the requirement of good lattice match between cores and shells greatly restricts further generalization of such a seed-mediated growth method.

To realize the general formation of uniform MOF coatings on numerous classifications of functional substrates, providing a proper interaction between MOF coatings and integrated materials in the solution system is of great importance for the liquid–liquid synthesis method. The surface modification strategy is usually used to efficiently modulate the interaction between the reaction interfaces, including surfactants, organic macromolecules, metal phenolic networks (MPNs) and so on.[80,84,85] There are three main advantages of surface modification to obtain uniform MOF coatings on the selected substrates: (1) to stabilize various integrated materials in polar solvents (*e.g.* methanol, ethanol, *N*,*N*-dimethylformamide (DMF)), especially for small-size nanocrystals; (2) to act as a capping agent to control the size and shape of the obtained composites during their synthesis processes; (3) to induce the growth of MOF coatings on the integrated materials by a weak interaction. For example, Lu *et al.* demonstrated an efficient encapsulation strategy to implant various surfactant-capped nanostructured materials with different sizes, shapes and compositions into ZIF-8 crystals (Fig. 5i).[39] First, the surfaces of various as-prepared nanoparticles were functionalized with polyvinylpyrrolidone (PVP). Subsequently, the methanolic solutions of PVP-modified nanoparticles, zinc nitrate and Hmim were fully mixed together and then kept for 24 hours without stirring. Finally, after centrifugation and washing, the selected nanoparticles were encapsulated in a well-dispersed fashion in ZIF-8 crystals. In addition, the spatial distribution of embedded metal nanoparticles within ZIF-8 hosts (in the central areas or off the central areas) can be controlled by simply modulating their addition sequence. During the MOF synthesis, the addition of PVP-modified nanoparticles at the beginning (T_0) results in their spatial distribution in the central areas of ZIF-8 crystals, while the addition of nanoparticles after a certain time (T) led to their distribution off the central areas of ZIF-8 crystals. Furthermore, Hu *et al.* demonstrated that ethyltrimethylammonium bromide (CTAB) as an efficient ionic surfactant bridged the as-prepared metal and ZIF-8 surfaces and thus facilitated the controlled alignment.[86] The resulting metal@MOF core–shell nanocomposites displayed single metal nanocrystals individually confined in single-crystalline MOF cubes (Fig. 5j). In addition, by modulating the CTAB amount, the ZIF-8 shell thickness was easily controlled from 35 to 60 nm. The TEM image exhibited a good alignment between the [100] planes of metal nanocubes and the [110] planes of MOFs (Fig. 5k). This controlled alignment effect is mainly attributed to the self-assembled CTAB molecules between metal nanoparticles and MOFs, which is not observed for the addition of other polymer molecules.

Besides the above surfactants, Long *et al.* used MPN thin films to bridge ZIF-8 and core materials to construct core@shell materials in the methanol solution.[87] The Fe^{3+} and residual catechol/galloyl groups in MPNs can react with the ZIF-8 precursor *via* coordination and hydrophobic interactions, thus inducing the heterogeneous nucleation and further growth of ZIF-8 crystals on MPNs. This MPN film has two main advantages, such as the rapid assembly process and non-sensitivity to substrates, which endow this novel strategy with saving time and wide adaption for various nanostructures. In addition, by using organic macromolecules (*e.g.*, (3-aminopropyl)trimethoxysilane and poly(sodium 4-styrene-sulfonate)) for surface medication, Huang *et al.* reported a versatile strategy to uniformly coat various components with diverse shapes and sizes (carbon nanotubes (CNTs), hydroxides, oxides, polymers and MOFs) with an elaborately controlled ZIF-8 shell.[88]

With the assistance of electrochemical processes, MOF thin films can also be controllably deposited on the electrode surfaces in electrolytic tanks.[89–92] During the electrochemical process, the formation mechanisms of MOF shells mainly include two kinds as follows: one is based on the coordination reaction of anodic oxidized ions from metal substrates with organic ligands in the electrolyte; the other is the coordination reaction of deprotonated

organic ligands with metal ions in the electrolyte because of the increase of pH near the cathodic electrode surface.[93] For example, Li *et al.* synthesized dense $Zn_3(BTC)_2$ MOF films on Zn plates in a H_3BTC-contained solution by a facile electrochemical plating method.[94] By applying a voltage, the Zn^{2+} was first generated *via* the anodic dissolution of Zn plates and then coordinated with H_3BTC. Interestingly, simply increasing the voltage from 0.5 V to 2 V resulted in the formation of much denser and thicker MOF coatings. In addition, Li *et al.* synthesized MOF-5 thin films *via* the deprotonation of neutral ligands triggered by pH increase under cathodic bias and subsequent coordination reaction with metal ions.[95] Therefore, this electrochemistry-induced liquid–liquid synthesis method shows some advantageous features of mild preparation, short growth time, being easy to scale up and controlled phase/morphology/thickness of deposited MOF coatings *via* altering voltages and reaction time.

3.2 Solid–liquid synthesis method

The solid–liquid synthesis method involves the coordination reaction between solid metal ion sources and liquid organic ligands. The selected solid precursors play important roles in the successful formation of uniform and high-quality MOF coatings, which act as the metal ion sources and orient the interfacial growth of MOF coatings on their surfaces. The solid precursors include metal oxides, metal hydroxides, metal carbonates, *etc.* In addition, the liquid organic ligands can be in a solution or molten state, which show high mobility, good contact with solid precursors, and relatively fast reaction kinetics.[96–98] The formation mechanism of MOF coatings is a dissolution–regrowth process at solid–liquid interfaces. This solid–liquid synthesis method is featured by simple manipulation, uniform MOF coatings, and low cost, which shows great potential for the synthesis and application of MOF coatings. By contrast, in the above liquid–liquid synthesis method, the surface modification with specific functional groups on templates can usually confine the growth of MOFs on their surfaces, but the direct nucleation and growth of MOF crystals in solution cannot be prevented. Some typical examples based on this solid–liquid synthesis method are discussed in detail.

To realize the controlled conversion of MOF nanocrystals into well-aligned MOF superstructures, Zhan *et al.* proposed this solid–liquid synthesis method to successfully fabricate freestanding core–shell ZnO@ZIF-8 nanorod arrays and nanotube arrays based on the selected ZnO self-templates.[99] The formation process of the core–shell ZnO@ZIF-8 nanorod array is illustrated in Fig. 6a. First, freestanding ZnO nanorod arrays grown on a fluorine-doped tin oxide (FTO) coated glass were pre-synthesized as sacrificial templates. Then, Hmim was dissolved in the mixed solvent of DMF and H_2O, and added together with the as-prepared sacrificial templates into the Teflon-lined autoclave. In this mixture, the ZnO templates slowly released the Zn ions, and coordinated with abundant organic ligands to preferentially grow MOF coatings on their surfaces. After heat treatment (24 h, 70 °C) and ethanol washing, uniform core–shell ZnO@ZIF-8 nanorod arrays were obtained. As shown in Fig. 6b, the TEM image shows the inner ZnO nanorods with an average diameter of 400 ± 25 nm and the outer ZIF-8 shells with 300 ± 25 nm thickness. The high-angle annular dark-field scanning TEM (HAADF-STEM) image directly demonstrates the core–shell structure because of different core and shell contrasts. Furthermore, as shown in Fig. 6d–g, the N and C elements are almost all distributed in the outer layer of the nanorod, while the Zn element is mainly concentrated in the core and diluted in the MOF shell. In addition, a series of contrast experiments demonstrated that the key points to successfully fabricate well-defined ZnO@ZIF-8 heterostructures were the hybrid solvent composition and reaction temperature. To extend this solid–liquid synthesis strategy, Cai *et al.* used metal oxide and hydroxide nanostructured arrays as self-sacrificing templates to construct metal oxide@MOF or metal hydroxide@MOF hybrid arrays on various substrates.[100,101] In detail, different nanostructured metal oxides and hydroxides (such as CoO nanorods/nanowalls, NiO nanorods, and $Cu(OH)_2$ nanorods) with well-aligned array structures were first grown on various substrates (Ni foam, Cu mesh, Fe mesh, or Cu foil), and then coordinated with organic ligands in the solutions, thus resulting in the formation of the corresponding MOF coatings (such as ZIF-67, MOF-74 and HKUST-1) on their surfaces. In this regard, this proposed solid–liquid synthesis method opens a new pathway for developing functional MOF coatings.

Recently, Song *et al.* demonstrated a facile and general approach to construct a series of unique core–shell ZnO@ZIF heterostructures with various ZIF shells (Fig. 6h).[102] During the formation process, the addition sequence of Hmim and metal ions (*e.g.* Zn^{2+}, Co^{2+} and Fe^{2+}) played a crucial role in the formation of high-quality ZIF coatings. In the mixed solvent, the preferential addition of Hmim leads to its coordination with the Zn^{2+} from ZnO nanowires to form a thin ZIF-8 seed layer on their surfaces within a short time *via* a dissolution–regrowth process. The subsequent addition of Co^{2+} into the above mixture with superfluous Zn^{2+} and Hmim results in the formation of Co/Zn-ZIF by a coordination reaction. In this reaction, a ZIF-8 seed layer played an important role in achieving epitaxial growth of different ZIFs. The Zn/Co-ZIF nanocrystals uniformly nucleated and grew onto the ZIF-8 seed surface due to their good lattice match. Meanwhile, the slow dissolution of ZIF-8 seed coated ZnO can retard the reaction kinetics among precursors, thus resulting in the formation of uniform core–shell ZnO nanowire (NW)@ZIF-8@Zn/Co-ZIF heterostructures. As shown in Fig. 6i, SEM and TEM images clearly demonstrated the well-defined core–shell structure of the ZnO NW@ZIF-8@Zn/Co-ZIF product. This growth strategy can be widely extended to obtain various ZIFs with different morphologies and components, including 2D ZnO NP@Zn/Co-ZIF nanoplates, 3D ZnO NF@Zn/Co-ZIF nanoflowers, one-dimensional (1D) ZnO NW@ ZIF-8@Zn/Fe-ZIF nanowires, 1D ZnO NW@ZIF-8@ZIF-7 nanowires and 2D ZnO NP@ZIF-8@Zn/Fe-ZIF nanoplates. A series of structural characterization experiments were also carried out to confirm their core–shell structures. Therefore, this present general strategy and in-depth insights provide good directions for the design and synthesis of uniform MOF coatings on self-sacrificing templates.

Besides the organic linkers in the solutions, molten organic ligands are also used in the solid–liquid synthesis method.[103,104]

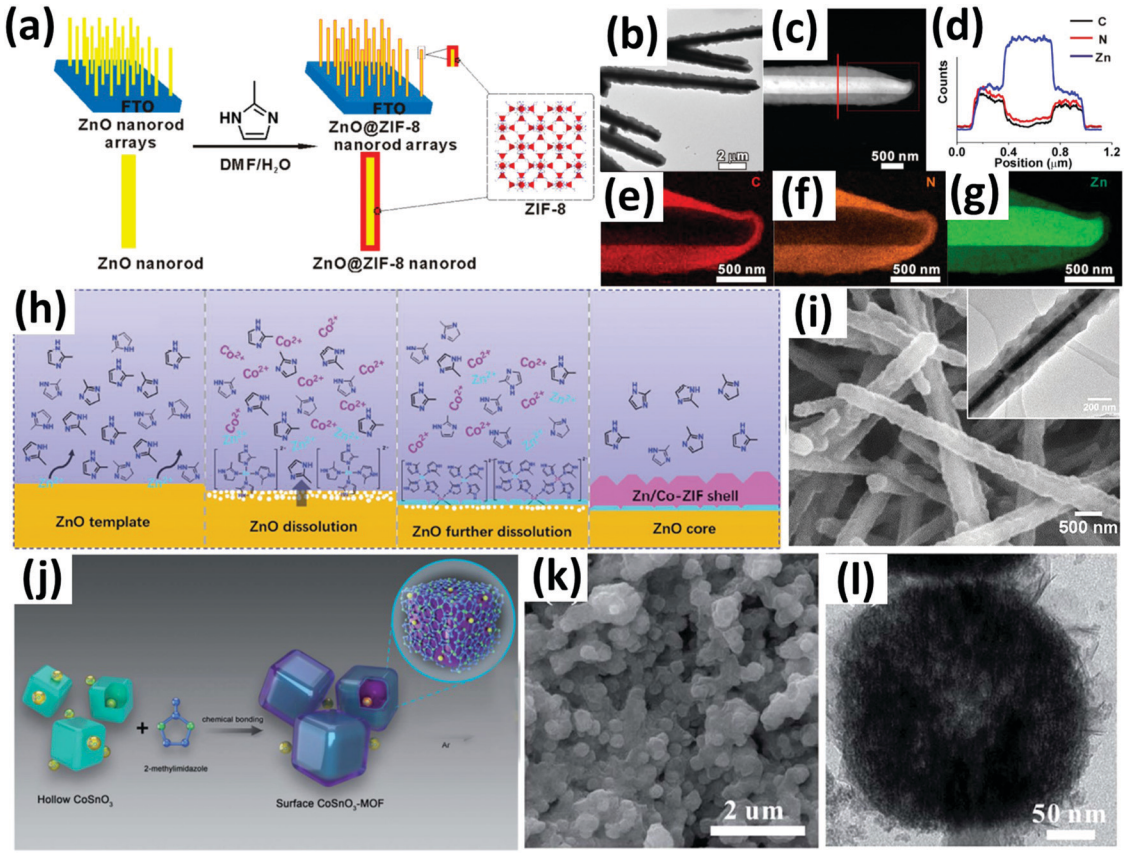

Fig. 6 (a) Schematic illustration of ZnO@ZIF-8 nanorods synthesized *via* the self-template strategy. (b) TEM image of ZnO@ZIF-8 nanorods. (c) HAADF-STEM image of an individual ZnO@ZIF-8 nanorod. (d) Cross sectional compositional line profiles of ZnO/ZIF-8. (e–g) Elemental maps of C, N, and Zn distributions in the ZnO@ZIF-8 nanorod. (h) Schematic representation of the growth of bimetallic Zn/Co-ZIF using ZnO NWs as a template. (i) SEM and the corresponding TEM images (inset) of one-dimensional (1D) ZnO NW@ZIF-8@Zn/Co-ZIF. (j) The design process for the preparation of $CoSnO_3$-MOFs. (k and l) SEM and TEM images of $CoSnO_3$-MOFs nanoboxes. (a–g) Reproduced with permission from ref. 99. Copyright 2013, American Chemical Society. (h and i) Reproduced with permission from ref. 102. Copyright 2018, Wiley-VCH. (j–l) Reproduced with permission from ref. 105. Copyright 2018, Royal Society of Chemistry.

Recently, Zou *et al.* reported a facile and solvent-free method to fabricate MOF-coated $CoSnO_3$ ($CoSnO_3$-MOF) nanoboxes *via* a coordination reaction between solid templates and liquid organic ligands during the solvothermal process.[105] Because of its low melting point of 136 °C, the Hmim powder is considered as an ideal kind of organic ligands. The formation process of $CoSnO_3$-MOF nanoboxes is clearly illustrated in Fig. 6j. First, the as-prepared Zn_2SiO_4 nanowire powders and Hmim powders (1 : 1 w/w) were fully ground to form a mixture and transferred into a Teflon autoclave. Subsequently, after being treated at 200 °C, the molten Hmim reacted with $CoSnO_3$ nanowires by breaking the Co–O bonds at their solid–liquid interfaces. In this reaction, the as-prepared $CoSnO_3$ nanoboxes as the Co^{2+} source oriented the superassembly of the molten Hmim *via* coordination reactions, resulting in the formation of MOF shells. Furthermore, SEM and TEM images demonstrated the thin ZIF shell on core $CoSnO_3$ nanoboxes (Fig. 6k and l). In addition, by modulating the amount of Hmim introduced, the content of MOFs in $CoSnO_3$-MOF composites can be controlled. Therefore, the above-mentioned results demonstrated this facile and efficient solid–liquid synthesis strategy for MOF coatings on diverse functional nanostructures.

3.3 Solid–solid synthesis method

The solid–solid synthesis method refers to an interfacial coordination reaction between solid metal precursors and solid organic ligands in certain conditions, which is featured by simple operation, no solvents and high yield. In this reaction, the solid metal precursors are used as metal ion sources and further orient the *in situ* formation of MOF coatings on their surfaces *via* a well-defined coordination reaction with solid organic ligands.[106,107] The whole process involves the breaking of the bonds in metal-based precursors and the formation of new coordination bonds. The bonding energy in metal precursors plays an important role in controlling the release of metal ions and thus determining the formation of MOF coatings. Generally, some low-binding-energy metal-containing precursors are selected as ideal candidates, including metal oxides, metal hydroxides, metal carbonates, metal salts, *etc.* The residual organic ligands can be completely removed by subsequent heat treatment or solvent washing, resulting in the formation of clean and uniform MOF coatings on solid metal precursors. Different from common soluble metal salts in a homogeneous solution, the diffusion rate of metal ions within solid metal precursors is generally very low.

Normally, these coordination reactions cannot occur spontaneously *via* simple physical mixing of solid metal precursors and solid organic ligands. Nevertheless, the metal ions can be efficiently released *via* additional treatments, mainly including mechanochemistry (*e.g.*, mortar grinding or high-energy ball milling), oven heating, hot pressure and microwave heating, *etc.* Some typical examples of this solid–solid synthesis of MOF coatings are discussed in detail as follows.

Mechanochemistry triggered by mechanical actions (*e.g.*, mortar grinding or high-energy ball milling) is an efficient solid–solid synthesis method with specific advantages of short reaction time and low temperature.[108–112] Tanaka *et al.* reported the successful solvent/additive-free mechanochemical dry conversion of ZnO to ZIF-8 by a dynamical milling process, resulting in the formation of polycrystalline ZIFs and/or a core–shell ZnO@ZIF-8 structure.[113] The two conversion processes based on different sized ZnO particles are illustrated in Fig. 7a. A ball mill acts as an efficient additional treatment. The kinetic energy during milling can provide several advantages on accelerating the coordination reaction, including particle size reduction, defect/dislocation formation in crystal lattices, local heating and local melting. For example, when using nano-sized ZnO powders of around 24 nm as solid metal precursors, the complete conversion occurred from ZnO nanoparticles to polycrystalline ZIF crystals (Case I). The possible reaction equation was proposed as follows:

$$ZnO(s) + 2Hmim(s) \rightarrow Zn(mim)_2(s) + H_2O(l)$$

ZnO reacts with solid Hmim and then releases liquid water as the sole byproduct. In addition, while using large ZnO particles in this synthesis, the coordination reaction with Hmim preferentially occurred on their surfaces (Case II). As the reaction went on to some extent, a relatively thick ZIF-8 shell was completely coated on the surface of large ZnO particles, and hindered the release of Zn^{2+} from internal ZnO cores, thus terminating the coordination reaction. Finally, a core–shell ZnO@ZIF-8 structure was successfully obtained. As shown in Fig. 7b and c, TEM images exhibited a clear ZIF-8 shell with about 20 nm thickness, confirming its core–shell structure. This green mechanochemical strategy can also be applied for other ZIF-related nanocomposites.

To further accelerate the solid–solid synthesis process, Cliffe *et al.* demonstrated a conceptually novel approach to accelerate the coordination reaction between solid imidazoles and ZnO *via* the addition of ammonium sulfate (under 4 mol%).[114] The "accelerated aging" mechanism is further revealed in Fig. 7d. First, the mixtures of $(NH_4)_2SO_4$ and imidazole (Him) rapidly deliquesced at high humidity at 45 °C, which can greatly enhance the molecular diffusion. Because of the loss of gaseous NH_3 at 45 °C, the formation of $(H_2im)_2SO_4{\cdot}2H_2O$ from Him and $(NH_4)_2SO_4$ occurred. Then, the formed H_2im^+ as protonated imidazolium cations reacted with solid ZnO. After reaction with ZnO and fresh Him, the H_2im^+ could be regenerated, which offers a rational explanation for the catalysis of the whole accelerated process. This proof-of-principle strategy can also be

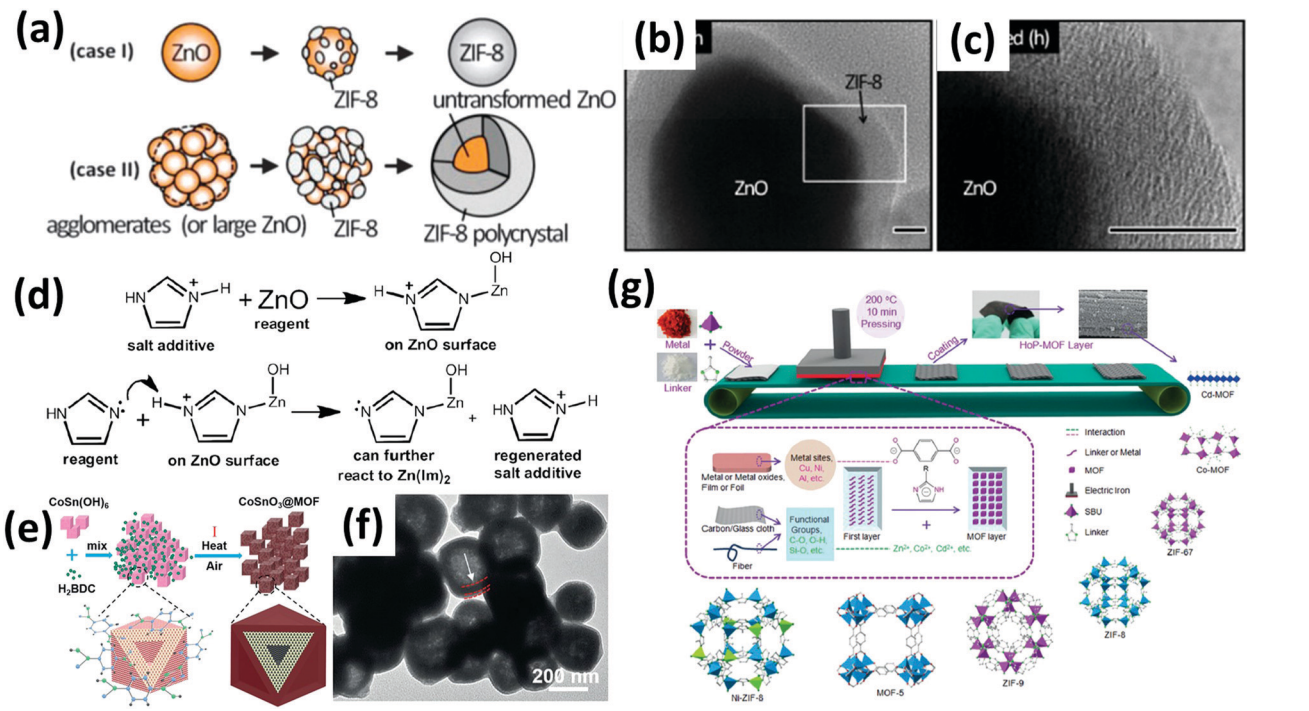

Fig. 7 (a) Proposed mechanism for mechanochemical dry conversion of ZnO to ZIF-8. (b and c) TEM images of ZnO@ZIF-8 nanoparticles. Scale bar: 20 nm. (d) Tentative mechanism illustrating the potential role of imidazolium ions as catalysts for ZIF synthesis. (e) Schematic illustration of the solvent-free synthesis process of $CoSnO_3$@MOF hollow nanocubes. (f) TEM image of $CoSnO_3$@MOF hollow nanocubes. (g) Schematic representation of the hot-pressing method for MOF coatings on substrates. (a–c) Reproduced with permission from ref. 113. Copyright 2013, Royal Society of Chemistry. (d) Reproduced with permission from ref. 109. Copyright 2012, Royal Society of Chemistry. (e and f) Reproduced with permission from ref. 54. Copyright 2017, Wiley-VCH. (g) Reproduced with permission from ref. 115. Copyright 2016, Wiley-VCH.

extended to accelerate the reactivity of other imidazole ligands, including Hmim, 2-ethylimidazole and benzimidazole. The reactivity is readily scaled up in 10 gram amounts, confirming the great potential of this novel, green and large-scale synthesis strategy for MOFs.

In addition, the oven heating treatment is also an important approach to trigger and accelerate the coordination reaction between solid inorganic metal precursors and solid organic ligands, thus resulting in the successful formation of uniform MOF coatings. Our group constructed uniform MOF-coated $CoSnO_3$ hollow nanocubes by a heat-induced coordination reaction between $CoSn(OH)_6$ hollow nanocubes and 1,4-benzenedicarboxylic acid (H_2BDC), demonstrating a novel solvent-free solid–solid synthesis method (Fig. 7e).[54] First, the as-prepared $CoSn(OH)_6$ hollow nanocubes and abundant H_2BDC were mixed by hand grinding. Then, the mixture was treated at 300 °C for 1 h in air. During this process, the interfacial coordination reaction between $CoSn(OH)_6$ hollow nanocubes and H_2BDC occurred. In the meantime, $CoSn(OH)_6$ was converted into stable $CoSnO_3$ because of its pyrolysis. Subsequently, after being treated at 320 °C for 0.5 h, the residual solid H_2BDC was sublimated into gaseous H_2BDC. Finally, the uniform MOF-coated $CoSnO_3$ hollow nanocubes were obtained. As shown in Fig. 7f, the resulting nanocubes displayed a hollow interior and a thin shell. Furthermore, this solid–solid synthesis method can also be extended to synthesize ZnO@MOF microflowers and $Zn_3V_2O_8$@MOF nanoplates. Therefore, this simple and scalable strategy to introduce a MOF coating layer on diverse nanostructured materials shows great potential for practical applications.

Recently, to obtain stable MOF devices with tunable flexibility, Chen *et al.* reported a solvent-/binder-free solid–solid synthesis approach for producing stable MOF coatings onto desired substrates (*e.g.* metal foil, cloth, and fibers) by a unique hot-pressing method under 200 °C for only 10 minutes (Fig. 7g).[115] During this process, the temperature and pressure are applied simultaneously on the powdered mixture of solid metal precursors, organic ligands and polyethylene glycol (PEG). First, metal ions and organic linkers rapidly form the first MOF layer on the substrates *via* coordination reaction due to the existence of functional groups. Then, the nucleation and growth of MOF nanocrystals were induced on the as-formed layer, consequently forming uniform MOF coatings. It is noted that PEG during this synthesis process can enhance the initial diffusion of metal ions, which is beneficial for the rapid growth of MOF crystals on the substrates. This versatile method can successfully be applied to obtain carboxylate-based (MOF-5, Co-MOF, and Cd-MOF), imidazolate-based (ZIF-8, ZIF-67, and ZIF-9), and mixed-metal MOF (nickel-doped Ni-ZIF-8) coatings on desired substrates. In addition, by modulating the layer-by-layer pressing process, the superhydrophobic and "Janus" MOF films can be well designed and constructed, including 1*H*,1*H*,2*H*,2*H*-perfluorooctyltriethoxysilane modified ZIF-8@carbon cloth and "Janus" ZIF-8@carbon cloth@ZIF-67. This hot-pressing method can easily be scaled up *via* a roll-to-roll hot-pressing machine, in which many synthesis conditions, such as hot-pressing temperature, pressure, and working speed, can be adjusted. Therefore, this approach opens up a new avenue to develop diverse MOF coatings on desirable substrates for a wide range of industrial applications.

3.4 Solid–gas synthesis method

The solid–gas synthesis method for MOF coatings involves the coordination reaction between solid metal precursors and gaseous organic ligands.[116–118] During this process, the solid metal precursors, acting as metal ion sources, react with the incoming gaseous organic ligands to form thin MOF coatings on them.[119,120] Similar to the above-mentioned solid–solid synthesis method, this solid–gas interfacial reaction process also experiences the breaking of previous bonds in solid metal precursors and the subsequent formation of MOFs *via* new coordination bonds. Therefore, to realize the successful formation of MOF coatings, three main requirements should be considered: (1) selected metal precursors, (2) easily volatilable organic ligands, and (3) system reaction conditions. In more detail, the selected metal precursors should fulfil low bonding energy to easily release metal ions and well-defined coordination reaction between released metal ions and organic ligands to form crystalline MOFs. To date, the selected metal precursors include metal ion salts, metal-contained coordination polymers, metal oxides, metal hydroxides, metal carbonates, *etc.* In addition, the volatile organic ligands are highly demanded for this solid–gas reaction, which can greatly improve the concentration of gaseous organic ligands in the whole reaction system. The volatile organic ligands usually consist of small molecules, such as Him and Hmim. The system reaction conditions (*e.g.* high temperature, low pressure) play an important role in accelerating the sublimation of organic ligands and the coordination reaction kinetics. Furthermore, the solid–gas synthesis method for MOF coatings has the advantages of precise control, high quality coatings, no solvent consumption, simple manipulation, high yield and low cost. Some typical examples of this solid–gas synthesis of MOF coatings are discussed in detail as follows.

To integrate MOFs in microelectronics, Stassen *et al.* demonstrated a novel solid–gas synthesis approach towards high-quality ZIF-8 coatings with a uniform controlled thickness and high-aspect-ratio features *via* a chemical vapour deposition (CVD) process for the first time.[121] As shown in Fig. 8a, this CVD method involves two steps: a metal oxide deposition step and an interfacial solid–gas reaction step between metal oxides and gaseous organic ligands. In detail, atomic layer deposition (ALD) was carried out to precisely deposit metal oxide films with nanometer thickness on the substrates, which provides an ideal platform to investigate the relation between precursor film thickness and the oxide film conversion efficiency. After exposing to Hmim vapor at 100 °C for 30 min, the as-prepared zinc oxide films (3–15 nm in thickness) were fully transformed to uniform ZIF-8 coatings. This conversion mechanism from ZnO films to ZIF-8 coating is illustrated in Fig. 8b. During this process, the neutralization/coordination reaction between zinc oxide and gaseous Hmim spontaneously occurred. This phenomenon was greatly driven by the stabilization of the zinc coordination spheres. Simultaneously, this reaction led to the replacement of Zn–O bonds by Zn–N bonds and the formation of gaseous water.

In addition, this synthesis strategy also exhibited high-aspect-ratio features. Due to the advantages of the ALD method, the zinc oxide films were well deposited on the as-prepared silicon pillars with a 25 : 1 aspect ratio. After the above-mentioned treatment, the resulting ZIF-8 thin films homogeneously covered the pillars (Fig. 8c and d). Furthermore, combining the soft lithography technique, functionalized elastomeric pillar arrays with uniform ZIF-8 coatings and well-designed structures were fabricated *via* this solid–gas synthesis method. Therefore, this versatile strategy can achieve the precise integration of MOF materials in microelectronic devices.

Besides the metal oxides as solid precursors, Li *et al.* recently chose a Zn-based gel precursor to fabricate nanometre-thick MOF coatings on hollow fibers by combining sol–gel coating and the following scalable solid–gas route (Fig. 8e).[119] First, the Zn-based gel was prepared by heating the mixture of $Zn(CH_3COO)_2$ and ethanolamine in ethanol, and then was coated onto ammoniated polyvinylidene fluoride (PVDF) hollow fibers. Subsequently, after the vapor deposition of Hmim, the gel layer was directly transformed to the ZIF coating under heat treatment at 150 °C. As shown in Fig. 8f, the gaseous organic ligands interacted with the sensitive Zn-based gel by a coordination reaction,

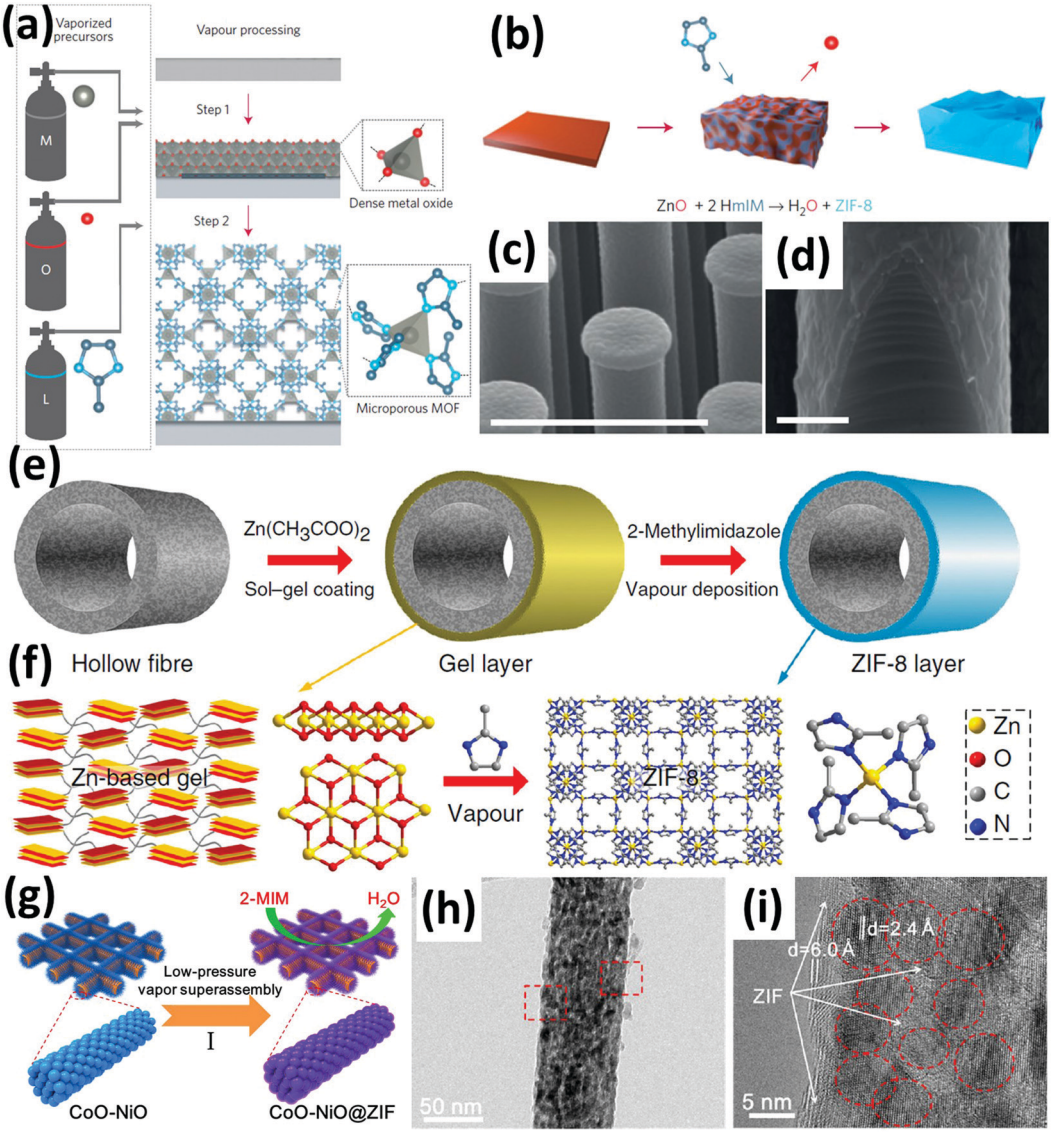

Fig. 8 (a) Chemical vapor deposition of ZIF-8 thin films. The procedure consists of metal oxide vapor deposition (Step 1) and a consecutive solid–gas reaction (Step 2). (b) Schematic overview of the transformation mechanism. (c) SEM image of the ZIF-8-coated silicon pillar array. Scale bar: 5 μm. (d) High-magnification SEM image showing the homogeneous coverage at the base of the pillars. Scale bar: 2 μm. (e) Schematic of the MOF membrane formation process. (f) Schematic illustration and chemical structure of the Zn-based gel and the crystalline structure of ZIF-8. (g) Schematics of the formation process of ZIF-confined CoO–NiO nanowire arrays on carbon cloth *via* a low-pressure vapor superassembly process. (h and i) TEM images of a single ZIF-confined CoO–NiO nanowire. (a–d) Reproduced with permission from ref. 121. Copyright 2016, Nature Publishing Group. (e and f) Reproduced with permission from ref. 119. Copyright 2017, Nature Publishing Group. (g–i) Reproduced with permission from ref. 122. Copyright 2017, American Chemical Society.

thus forming more stable ZIF-8. The resulting ZIF-8 coating exhibited a very thin thickness of ~87 nm. The thickness and position of ZIF-8 coating can be easily modulated by controlling the sol concentration and coating time as well as the gel coating process. Uniform ZIF-8 coatings selectively deposited on the outer and/or inner surfaces of the hollow fiber. This solid–gas synthesis method displayed some significant synthesis features of being solvent-/modification-free and precursor-/time-saving for MOF coatings.

Recently, our group reported a novel solid–gas method for the general synthesis of tunable and uniform MOF coatings on diverse nanostructured inorganic materials *via* a low-pressure vapor superassembly process (Fig. 8g).[122] During the formation process, the selected solid metal precursors acting as metal ion sources coordinated with the gaseous organic ligands, thus forming a controlled and uniform MOF shell. For example, the CoO–NiO mesoporous nanowire arrays were prepared as precursors, displaying uniform nanoparticle-assembled nanowires with ~60 nm diameter and ~2 μm length. After being treated at 120 °C and ~100 Pa, the volatile Hmim became gaseous and filled the whole system, and then reacted with the as-prepared CoO–NiO nanowires to form ZIF coatings on their surfaces. As shown in Fig. 8h and i, the TEM images confirmed the obvious thin ZIF shell and assembled nanoparticles in a single nanowire. Therefore, the reaction equation was proposed as follows:

$$\mathrm{CoO–NiO(s)} + \mathrm{Hmim(g)} \rightarrow \mathrm{CoO–NiO@ZIF(s)} + \mathrm{H_2O(g)}$$

During this process, the generated gaseous water volatilized away from the reaction interfaces, which facilitated this forward reaction. Furthermore, this strategy was successfully extended to obtain various precise MOF-coated nanostructures, including $CoSn(OH)_6$@MOF hollow nanocubes, ZnO@ZIF nanorods, $Zn_3Mo_2O_9$@ZIF nanosheets, and $MnCo_2O_4$@ZIF mesoporous nanotubes. More importantly, to realize the precise formation of MOF coatings, three main design principles were summarized, including low-bonding-energy metal oxides, volatile organic ligands, and relatively low-pressure condition. In brief, this synthetic approach and proposed requirements provide insights and directions into the synthesis of MOF coatings on diverse metal precursors.

3.5 Gas–gas synthesis method

Distinct from the above-mentioned synthesis methods for MOF coatings, this novel gas–gas synthesis strategy involves the coordination reaction between gaseous metal precursors and gaseous organic ligands on desirable substrates, mainly including the combined molecular and atomic layer deposition (MLD and ALD) techniques.[123,124] As clearly indicated by their names, these MLD and ALD techniques can efficiently control the material growth at the molecular and atomic levels.[125] ALD is a vapor-phase surface-controlled thin inorganic film technique based on alternative self-terminating surface reactions, while MLD is usually used to synthesize polymeric films. Therefore, the strongly emerging (ALD/MLD) technique combined two merits, developing new hybrid organic–inorganic materials especially MOFs with amazing properties. During the formation process of MOF coatings, the metal precursors and organic ligands as the reactants are carried to the reaction chamber in the form of gas pulse on the basis of respective ALD/MLD treatments, and then the coordination reaction occurs on the upper surface preferentially. After a single cycle, always a constant thickness (generally several atomic layers) can be acquired. By controlling the number of cycles, an expectant thickness can be easily achieved. What's more, profiting from the high diffusivity of gas used in the whole system, uniform MOF coatings can be synthesized on the target material surface or in the nanopores. Therefore, beneficial for complementary MLD and ALD techniques, this novel gas–gas synthesis strategy is featured by some advantages of excellent uniform coverage over large-scale or high-aspect-ratio substrates as well as precise atomic/molecular level control of the film thickness and composition.[126,127]

Using this ALD/MLD technique, Ahvenniemi *et al.* fabricated well-crystalline calcium terephthalate (Ca-TP) coordination network thin films on substrates in a wide deposition temperature range.[125] The volatile $Ca(thd)_2$ (thd: 2,2,6,6-tetramethyl-3,5-heptanedione) and benzene-1,4-dicarboxylic acid (terephthalic acid, TPA) were selected as metal and organic ligand precursors, respectively. Because the sublimation temperatures were set to 190 °C for $Ca(thd)_2$ and 180 °C for BDC, the deposition temperature was above 190 °C. The detailed formation process is shown in Fig. 9a, including two successive steps. First, one monolayer of volatile $Ca(thd)_2$ precursor was deposited on the substrate by ALD. Then, on the basis of MLD, the second layer of volatile organic linkers was deposited and reacted with the former $Ca(thd)_2$ layer *via* coordination bonds. The detailed procedure for one ALD/MLD cycle is 5 s $Ca(thd)_2$ pulse → 2 s N_2 purge → 10 s TPA pulse → 20 s N_2 purge. After repeating ALD/MLD cycles, thin MOF films with the desired thickness can be easily obtained. As shown in Fig. 9b, the growth of the resulting films is in a highly linear manner (R^2 = 0.9983) in the thickness range of 15–180 nm. In addition, the surface roughness also displays a nearly linear relationship (R^2 = 0.910) with increasing cycles. The resulting Ca-TP thin film is composed of 3D coordination networks, where the calcium atoms are coordinated to the organic molecules *via* oxygen atoms (Fig. 9c). More interestingly, under humid conditions, the introduction of absorbed water into crystal structures led to the transformation from "dry" Ca-TP to"trihydrated" Ca-TP without the change of the roughness value.

To further extend this ALD/MLD approach to other MOF thin films, Lausund *et al.* reported uniform thin-film deposition of stable UiO-66 in an all-gas-phase process with the assistance of acetic acid vapour.[128] The *in situ* quartz-crystal microbalance (QCM) technique was carried out to study the real-time mass variation in the $ZrCl_4$ and 1,4-BDC system at a deposition temperature of 265 °C. During this process, the typical sequence of gaseous precursors was programmed as follows: 4 s $ZrCl_4$ pulse, 6 s purge, 5 s 1,4-BDC pulse and 6 s purge (Fig. 9d). In contrast, the addition of the acetic acid pulse had no effect on the overall growth rate increase per cycle. The overall growth rate was about 100.8 ng cm^{-2} $cycle^{-1}$. On the basis of mass analysis from QCM, a 66% mass increase after one $ZrCl_4$ pulse and the remaining 34% increase for the 1,4-BDC and acetic acid

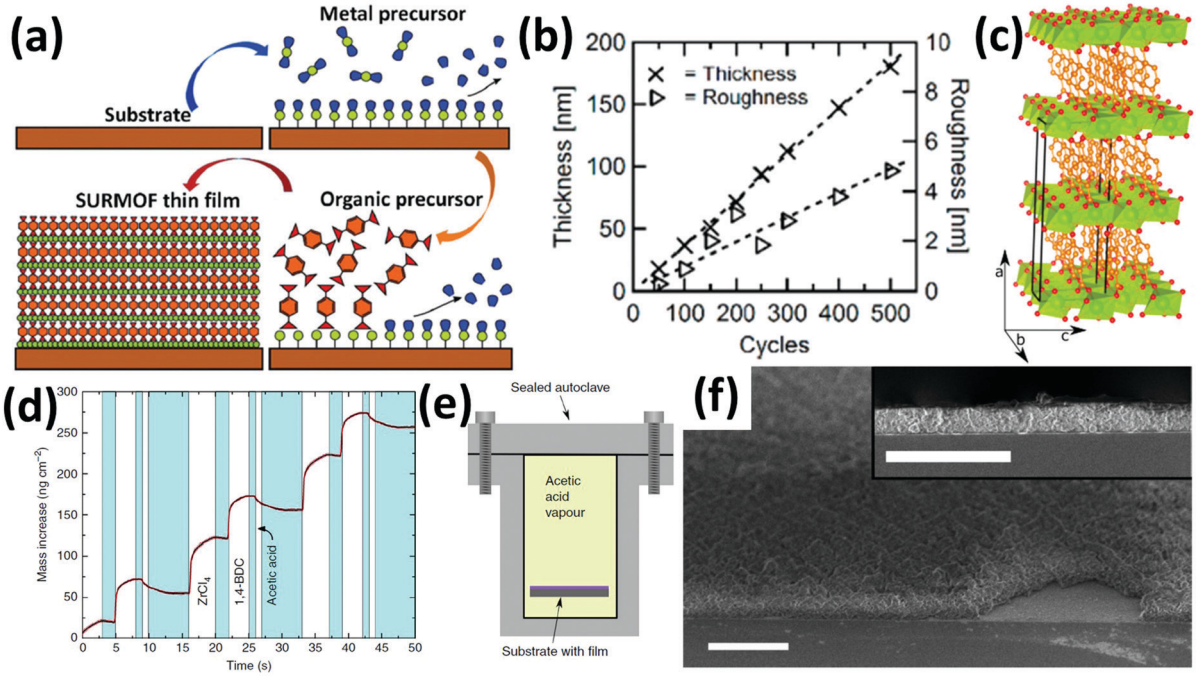

Fig. 9 (a) Schematics of the ALD/MLD process for inorganic–organic coordination network thin films, where the process consists of inert-gas-separated pulses of metal (here $Ca(thd)_2$) and organic (here TPA) precursors to yield a monolayer of the hybrid material (here Ca-TP). (b) The film thickness and roughness increase linearly with the number of ALD/MLD cycles. (c) Dry (space group *C*2/*c*) Ca-TP structures viewed along the layer-piling direction. (d) QCM measurements showing mass increase (and loss) as the precursors and the modulator are pulsed. The blue panels indicate inert gas (N_2) purging. The red lines show the standard deviations for the QCM data (n = 16). (e) Experimental setup for heat treatment of the films in acetic acid vapor. (f) Cross-sectional SEM images of the same surface viewed at 45° and 90°. Scale bar: 2 μm. (a–c) Reproduced with permission from ref. 125. Copyright 2016, American Chemical Society. (d–f) Reproduced with permission from ref. 128. Copyright 2016, Nature Publishing Group.

pulse were observed. However, the resulting UiO-66 has a 1 : 1 stoichiometry between $Zr_6O_4(OH)_4^{12+}$ clusters and 12–COO^- functional groups. The possible reaction equations were proposed as follows:

$ZrCl_4$ pulse:

$$-(OH)_{1.75} + ZrCl_4(g) \rightarrow -O_{1.75}ZrCl_{2.25} + 1.75HCl(g)$$

1,4-BDC pulse:

$$-O_{1.75}ZrCl_{2.25} + C_6H_4(COOH)_2(g) \rightarrow -O_{1.75}Zr(C_6H_4O_{2.25})(OH)_{1.75} + 2.25HCl(g)$$

After repeating ALD/MLD cycles, amorphous organic–inorganic hybrid films were obtained. Subsequently, the as-prepared films were sealed in an autoclave and treated in acetic acid vapour at 160 °C for 24 h (Fig. 9e). As shown in Fig. 9f, the thickness of the target UiO-66 film increased from 229 to ~500 nm because of the reconstruction of 3D crystalline open frameworks. In addition, the stoichiometry between metal clusters and organic linkers was easily controlled by modulating the ALD/MLD process with additional acetic acid pulses. Therefore, this approach provides precise thickness control over MOF coatings even on irregular high-aspect-ratio substrates.

In brief, this part highlights the synthesis chemistry of MOF coatings and summarizes the above-mentioned five important strategies based on different states of metal precursors and the corresponding organic linkers. Table 1 makes a detailed comparison of these synthetic methods for MOF coatings. The formation mechanisms, controlled parameters, advantages and disadvantages of each synthesis method are systemically summarized and compared. These versatile strategies endow the MOF coatings with abundant compositions, delicate morphologies, and broad applications. On the one hand, it is highly desired to develop more new, economic and sustainable synthetic strategies or efficient modifications to obtain high-quality MOF coatings. On the other hand, low cost is crucial for large-scale applications in industry. The costs from MOF precursor sources and the fabrication process should be simultaneously considered. In addition, precise control, a solvent-free and time-saving process, and large-scale synthesis are highly desired for MOF coatings. By contrast, the solid–solid synthesis method and the solid–gas synthesis method possess similar characteristics of simple manipulation, high yield, no solvent consumption and low cost, which are beneficial for large-scale practical applications. Besides, due to their unique characteristics, solid–gas and gas–gas synthesis strategies for MOF coatings show great potential in microelectronics.

4. Broad applications of MOF coatings

4.1 Batteries

Lithium ion batteries (LIBs) have been widely studied for energy storage in numerous electronic devices. Nowadays, exploring

Table 1 A comparison of different synthesis strategies for MOF coatings

Synthesis strategy	Formation mechanism	Controlled parameters	Advantages	Disadvantages	Typical examples
Liquid–liquid synthesis method	Heterogeneous nucleation growth	Solvents; concentration; surface modification; temperature; time	• Simple manipulation • Abundant MOF coatings • Low cost • Relatively high yield • Without limited substrates • Relatively fast reaction kinetics	• Solvent consumption • Hard control on uniform coatings	MoS_2@ZIF-8; Pt-GO@ZIF-8; Pt-MoS_2@ZIF-8; ZIF-8@ZIF-67; Pd@ZIF-8
Solid–liquid synthesis method	Dissolution-then-regrowth	Concentration; temperature; time	• Simple manipulation • Uniform MOF coatings • Low cost	• Limited metal precursors • Solvent consumption • Low yield	ZnO@ZIF-8; ZnONW@ZIF-8@Zn/Co-ZIF; Zn_2SiO_4@ZIF-8
Solid–solid synthesis method	Interfacial coordination reaction	Heating conditions (*e.g.* oven heating, microwave heating); external mechanical force; time	• Simple manipulation • High yield • No solvent consumption • Low cost	• Limited metal precursors • Hard control on uniform coatings • Relatively slow reaction kinetics	ZnO@ZIF-8; $CoSnO_3$@MOF; ZIF-8@Carbon cloth
Solid–gas synthesis method	Interfacial coordination reaction	Low pressure; temperature; gas concentration; time	• Precise control • High quality coatings • No solvent consumption • High yield • Low cost • Simple manipulation	• Limited metal precursors • Relatively slow reaction kinetics	ZIF-8@silicon pillars; ZIF-8@hollow fiber; CoO-NiO@ZIF; $CoSn(OH)_6$@MOF; ZnO@ZIF
Gas–gas synthesis method	Layer-by-layer coordination reaction	Temperature; time; flow condition	• Precise control • No solvent consumption • High quality coatings • Without limited substrates	• High cost • Low yield • Complex manipulation • Limited MOF species	Ca-TP@substrates; UiO-66@substrates

new electrode materials with high energy and power densities as well as good stability is still highly recommended.[129–134] MOF coating-based composites have gradually received much attention owing to their unique discovered properties.[135–145] For example, Sun *et al.* demonstrated the greatly enhanced cycling performances of Fe_3O_4 by coating HKUST-1 (Fe_3O_4@HKUST-1) (Fig. 10a and b).[146] The special Fe_3O_4@HKUST-1 composite displays a microspheric core and a porous shell, and the latter is beneficial for electrolyte penetration and shows excellent capacity retention during battery cycles. Besides, the π-conjugated benzene ring and the carboxylates in HKUST-1 endow the whole electrode with good conductivity. As a result, compared to bare Fe_3O_4, the Fe_3O_4@HKUST-1 composite displays greatly enhanced rate performance ($\sim$400 mA h g^{-1} increment at 1 A g^{-1}) and excellent cycling stability with a remained capacity of $\sim$1002 mA h g^{-1} after 100 cycles at 0.1 A g^{-1} (Fig. 10c). MOF coatings can also reduce the direct contact between electrode material and electrolyte, and thus improve the initial coulombic efficiency (CE) of electrodes, especially for Li-rich layered oxides. Meanwhile, the efficient suppression of the oxygen loss issue is beneficial for practical battery systems.[147] Qiao *et al.* reported the 2–3 nm-thickness Mn-based MOF coating modified layered $Li(Li_{0.17}Ni_{0.20}Co_{0.05}Mn_{0.58})O_2$ electrode (Fig. 10d).[148] The initial coulombic efficiency was remarkably improved from 80.0% to 91.1% and the capacity was enhanced by $\sim$50 mA h g^{-1} after Mn-MOF coating (Fig. 10e). The enhanced CE was attributed to the strengthened

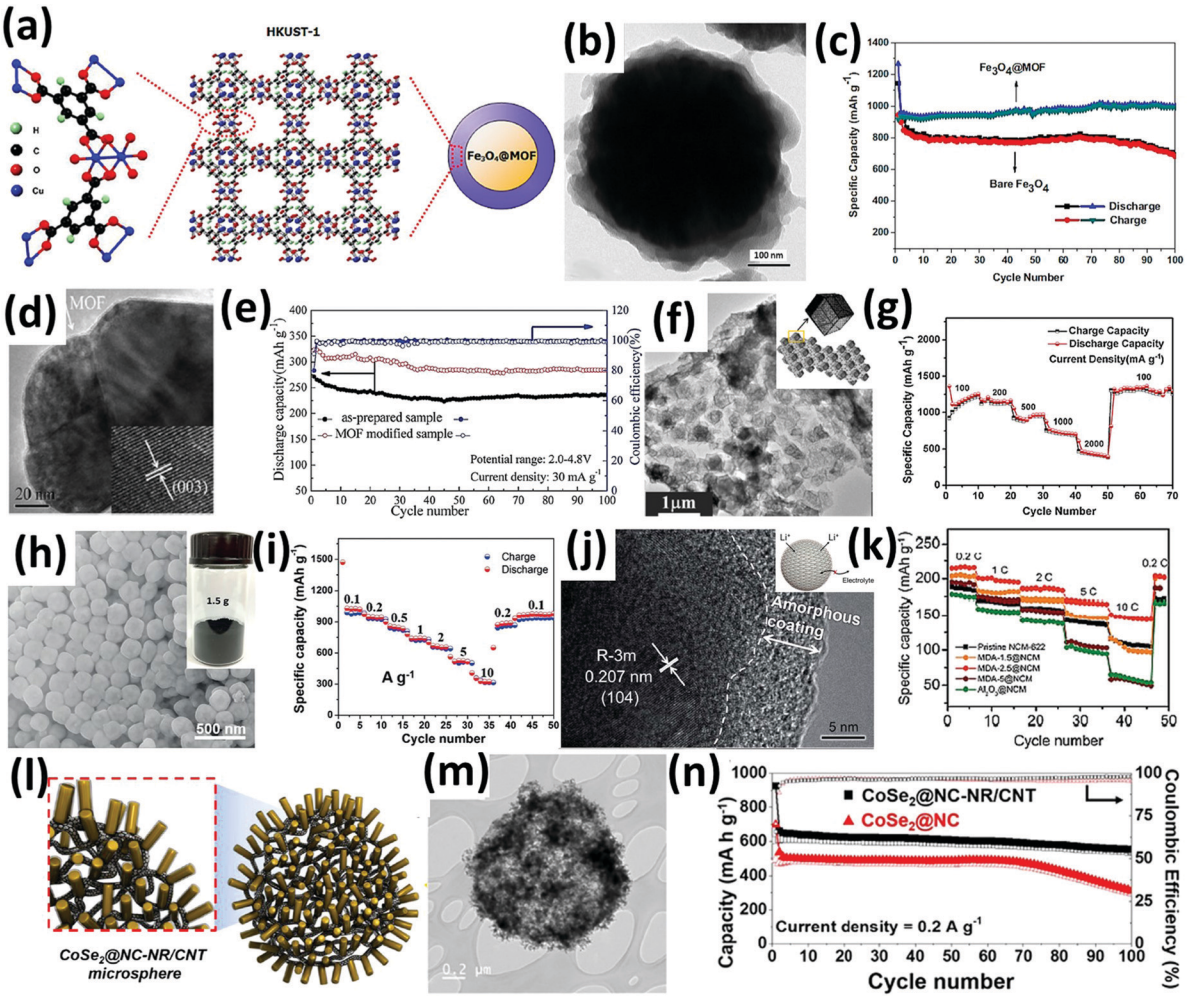

Fig. 10 (a) Schematic diagram of the core–shell Fe_3O_4@MOF composite structure, showing a microspheric core and a porous HKUST-1 shell. (b) TEM image of the Fe_3O_4@MOF composite. (c) Cycling performances of bare Fe_3O_4 and Fe_3O_4@MOF at 100 mA g^{-1}. (d) TEM and (inset) HRTEM images of MOF-modified $Li(Li_{0.17}Ni_{0.20}Co_{0.05}Mn_{0.58})O_2$ particles. (e) Cycling performances and coulombic efficiencies of $Li(Li_{0.17}Ni_{0.20}Co_{0.05}Mn_{0.58})O_2$ and MOF-modified $Li(Li_{0.17}Ni_{0.20}Co_{0.05}Mn_{0.58})O_2$ samples at 30 mA g^{-1}. (f and g) TEM image, (inset) schematic diagram and rate performance of the Co_3O_4–rGO–Co_3O_4 composite as the LIB anode. (h) SEM image of SnO_2/Co@C nanocubes and (i) the corresponding rate performance in LIBs. (j) HRTEM image and (inset) schematic diagram of MOF-derived alumina (MDA)-2.5@NCM. (k) Rate performances in LIBs. (l) Schematic diagram and (m) TEM image of the $CoSe_2$@NC-NR/CNT microsphere. (n) Cycling performances at a current density of 0.2 A g^{-1} for 100 cycles in SIBs. (a–c) Reproduced with permission from ref. 146. Copyright 2013, Elsevier Ltd. (d and e) Reproduced with permission from ref. 148. Copyright 2016, Royal Society of Chemistry. (f and g) Reproduced with permission from ref. 154. Copyright 2016, Elsevier Ltd. (h and i) Reproduced with permission from ref. 54. Copyright 2017, Wiley-VCH. (j and k) Reproduced with permission from ref. 155. Copyright 2016, Royal Society of Chemistry. (l–n) Reproduced with permission from ref. 167. Copyright 2018, American Chemical Society.

Table 2 A summary of functional electrode materials based on MOF coatings for lithium ion batteries

Electrode materials	Morphologies	Species of MOF coatings	Synthesis strategies	Working voltage range (V)	Current density (mA g^{-1})	Capacity retention (%)	Ref.
Fe_3O_4@MOF	Microspheres	HKUST-1	Liquid–liquid method	0.01–3.0	100	108.8% after 100 cycles	146
Fe-MOF/RGO	Nanosheets	Fe-MIL	Liquid–liquid method	0.01–3.0	500	111.9% after 200 cycles	156
C/Si/ZIF-8	Film	ZIF-8	Liquid–liquid method	0.01–2.0	265 μA cm^{-2}	48.2% after 50 cycles	157
ZIF-8/TiN/Ti/Si	Nanowire array	ZIF-8	Liquid–liquid method	0.13–2.8	10 μA cm^{-2}	600% after 40 cycles	158
MOF-modified $Li(Li_{0.17}Ni_{0.2}Co_{0.05}Mn_{0.58})O_2$	Nanoparticles	Mn-Based MOF	Liquid–liquid method	2.0–4.8	30	82.5% after 100 cycles	148
UiO-66@$LiCoO_2$-600	Microparticles	UiO-66	Solid–solid method	3.0–4.5	2325	89.5% after 100 cycles	159
LLO@C&NiCo	Nanoparticles	Ni,Co-ZIF	Solid–gas method	3.0–4.8	120	95% after 100 cycles	120
MND@NCM	Microspheres	NH_2-MIL53	Liquid–liquid method	3.0–4.5	140	92.7% after 100 cycles	155
Co_3O_4–rGO–Co_3O_4	Nanosheets	ZIF-67	Liquid–liquid method	0.01–3.0	100	70% after 100 cycles	154
Si@ZIF-8-700N	Nanoparticles	ZIF-8	Liquid–liquid method	0.02–3.0	200	99% after 500 cycles	160
C–$ZnCo_2O_4$–ZnO	Nanorod array	ZIF-8	Liquid–liquid method	0–3.0	100	144% after 300 cycles	161
C/Co–MnO	Nanowires	ZIF-67	Liquid–liquid method	0.01–3.0	500	90% after 50 cycles	162
NPCGS	Nanosheets	ZIF-8	Liquid–liquid method	0.01–3.0	500	119% after 200 cycles	163
SnO_2@C	Nanoparticles	ZIF-8	Liquid–liquid method	0.01–3.0	100	96% after 150 cycles	164
SnO_2/Co@C	Nanocubes	ZIF-67	Solid–solid method	0.01–3.0	5000	81% after 1800 cycles	54
MnO@$ZnMn_2O_4$/N–C	Nanorods	ZIF-8	Liquid–liquid method	0.01–3.0	50	135% after 100 cycles	165
LFP/C_{ZIF-8}	Nanoparticles	ZIF-8	Liquid–liquid method	2.5–4.2	850	99% after 150 cycles	166

bonding interaction between transition metals and oxygen, thus alleviating the oxygen evolution and stabilizing the host lattice in Li-rich layered oxides. Besides, the MOF materials possessed rich ion diffusion channels, which facilitated lithium ion migration and thus enhanced the capacity of the electrode. Prussian blue analogues with stable three-dimensional ionic channels as a typical class of MOFs show excellent performance as battery cathode materials.[149–151] To combine the merits of both Prussian blue (PB) and 2D layered materials, Morant-Giner *et al.* constructed PB nanocrystals coated on 2D MoS_2 sheets, displaying excellent electrochemical performances as cathodes for sodium- and potassium-ion batteries.[152]

The stable MOF coating could enhance battery performances. However, some MOF materials are unstable in the electrolyte during battery reaction, leading to poor battery performances. Considering that the MOF-derived materials also possess high specific surface area, porous structure properties and much higher electron conductivity, these MOF materials are also treated to carbonize to *in situ* form carbon-based materials.[153] For example, Yin *et al.* obtained RGO/Co_3O_4 composites through direct pyrolysis of the GO-MOF precursor, exhibiting good electrochemical performance for advanced lithium-ion batteries (LIBs, Fig. 10f and g).[154] He *et al.* reported the MOF shell-derived carbon confined SnO_2/Co (SnO_2/Co@C) nanocubes, exhibiting high rate and long-term cycling performance in LIBs (400 mA h g^{-1} at 5 A g^{-1} for 1800 cycles, Fig. 10h and i).[54] Besides, these carbon coatings suppress the side reactions of the electrolyte and stabilize the electrode. Li *et al.* used an Al-based MOF (NH_2-MIL-53) precursor to obtain a well-defined amorphous protecting layer on NCM-622, and demonstrated enhanced rate performance and long-term cycles in LIBs (Fig. 10j and k).[155] The improved electrochemical performance was attributed to the suppression of the side reactions, the amorphous coating layer without blocking the Li^+ diffusion pathways as well as the stable crystalline structure of NCM-622 from the coating protection. We systematically summarized the electrochemical performances of the functional electrode materials based on MOF or MOF-derived coatings applied in LIBs (Table 2), which suggests the potential lithium storage application of these composite materials.[54,120,148,154–166] Beyond good applications in LIBs, the MOF-derived carbon coating also endows the electrode materials with good electrochemical performances in sodium ion batteries (SIBs). Park *et al.* reported the MOF-derived nitrogen-doped carbon-coated $CoSe_2$ nanorods on 3D porous CNT microspheres ($CoSe_2$@NC-NR/CNT) applied in SIBs (Fig. 10l–n).[167] This work highlighted the significance of a 3D continuous conductive network, in which the MOF-derived carbon-based materials were connected by CNTs. The well-designed CNT framework provided a highly conductive pathway, fast mass transfer and enhanced structural integrity of the composites, thus endowing the resulting $CoSe_2$@NC-NR/CNT with excellent sodium-ion storage performance.

In brief, the above-mentioned part highlights the good battery applications of composite electrodes containing MOF coatings or MOF-derived carbon coatings for enhanced energy storage performances in terms of CE, specific capacity, rate capability and cycling stability. Furthermore, the superior electrochemical properties of MOF-coated or MOF-derived carbon-coated composites for batteries are summarized as follows: (1) the well-defined MOF or MOF-derived carbon coating layers effectively avoid the direct contact between electrode materials and electrolytes, thus reducing the side reactions of the electrolyte and resulting in high CE values, especially for high-voltage materials such as Li-rich layered oxides. (2) MOF or MOF-derived carbon coatings possess a porous structure and rich ion diffusion channels, which facilitate ion migration. (3) MOF-derived carbon coatings show high electron conductivity, which endows the resulting composites with fast electron transportation and high rate capability. (4) MOF or MOF-derived carbon coating layers could avoid the aggregation, buffer the volume variation and stabilize the structure of electrode materials during continuous charging/discharging processes, guaranteeing good cycling performance. Therefore, when modified by MOF coating or MOF-derived carbon coating, the composite electrodes can achieve high rate capacity and good cyclic capacity in batteries,

which provides good directions for the design and construction of functional composite materials towards high-performance energy storage.

Beyond univalent ion batteries, the MOF coatings can also be utilized in other new battery systems, such as lithium–sulfur batteries (LSBs), aqueous batteries, lithium metal batteries, and multivalent ion batteries.[168–171] For LSBs, the dissolution of the charge/discharge intermediate products (*i.e.* various polysulfides) in organic electrolytes results in rapid capacity fading of the sulfur cathode and poor cycling life.[172–176] To solve this issue, Bai *et al.* developed the HKUST-1-coated graphene oxide (HKUST-1@GO) separator to selectively sieve Li ions while blocking the polysulfides (Fig. 11a).[177] The selected HKUST-1 possessed 3D channels with highly ordered 9 Å-sized micropores, and was suited for blocking lithium polysulfide (Li_2S_n, $4 < n < 8$). To fabricate a mechanically flexible and robust composite separator, the HKUST-1 layer was *in situ* grown on the GO layer to form a tightly adhered membrane by parallel arrangement (Fig. 11b). As a result, the HKUST-1@GO separator endowed the LSBs with high efficiency in blocking polysulfides and excellent stability (Fig. 11c). In addition, due to their intrinsic properties of rich porosity, abundant exposed functional groups, and high surface areas, MOFs such as ZIF-8, MIL-53(Al), MIL-101(Cr), PCN-224 and MOF-5 provide strong physical confinement and chemisorption to suppress polysulfide migration.[178–182] Therefore, these MOF-based composites with carbon substrates or conductive polymers are widely used as sulfur hosts for Li–S battery cathodes. Rechargeable aqueous zinc-ion batteries (ZIBs) have also been considered as one of highly promising energy storage devices due to their low cost, high capacity, low flammability, inherent safety and so on.[183–186] However, exploring suitable cathode materials is necessary and important to lower the polarization of Zn^{2+} and widen the applicable voltage window, which are the key to realize high-energy and highly stable ZIBs. Very recently, Fu *et al.* reported the MOF-coating derived composites as Zn-storage cathode materials.[187] PVP-modified ZIF-8 coated MnO_2 nanowires were first obtained and then were transformed to N-doped carbon coated MnO_x (MnO_x@NC) nanowires *via* direct pyrolysis (Fig. 11d). Numerous nanopores caused by the high-temperature evaporation of Zn from ZIF-8 could significantly shorten the ion diffusion pathways, and the carbon coating enhanced the

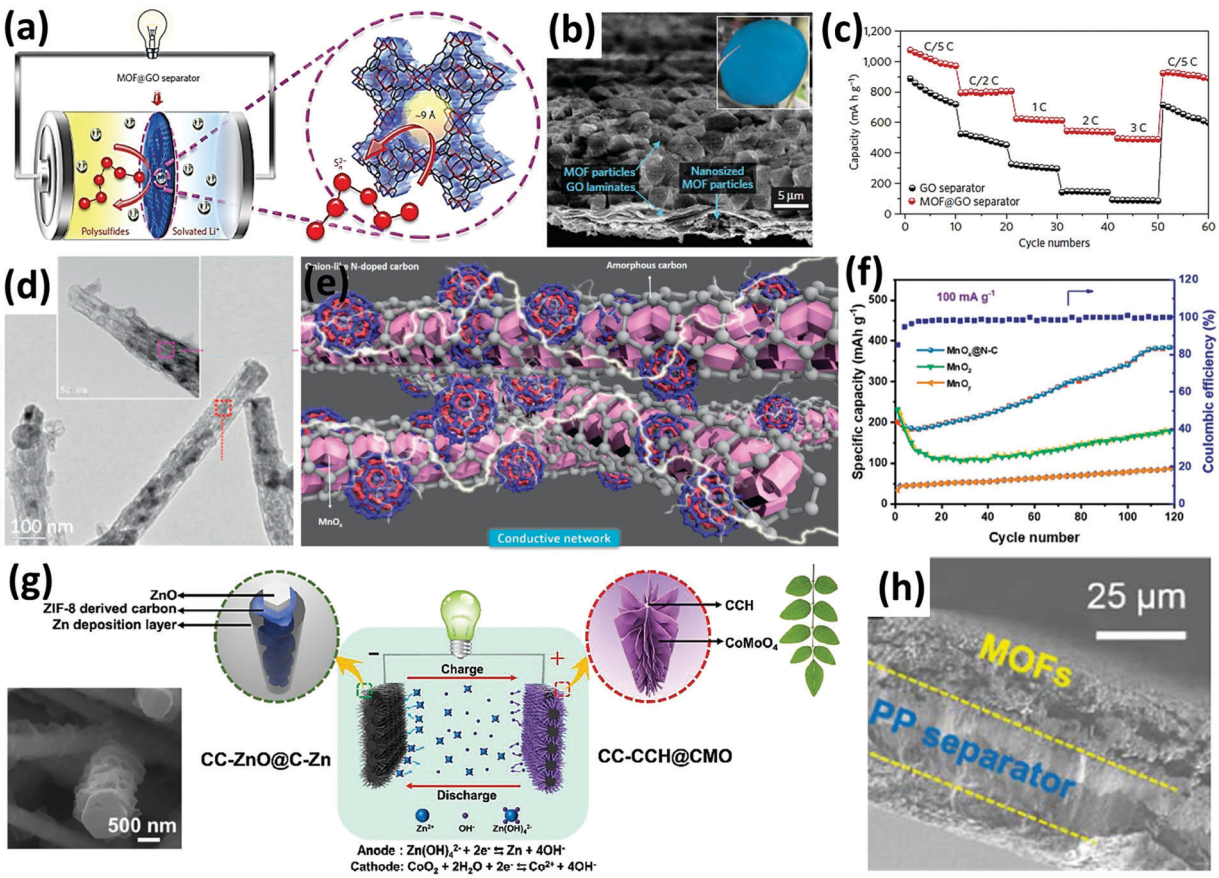

Fig. 11 (a) Schematic diagram of MOF@GO separators in lithium–sulfur batteries. (b) SEM image of the multilayered MOF@GO separator. The inset is a digital photo along the MOF side. (c) Rate performances with MOF@GO and GO separators. (d) TEM images of the MnO_x@N-C composite. (e) Schematic diagram of the interconnected part of three MnO_x@N-C nanorods. (f) Cycling performances of MnO_x@N-C, MnO_2, and MnO_y electrodes at 100 mA g^{-1}. (g) SEM image of core/shell CC-ZnO@C skeletons and schematic diagram of the Zn–Co full battery using the CC-ZnO@C-Zn anode and the CC-CCH@CMO cathode. (h) Cross-sectional view of the MOF-decorated separator. (a–c) Reproduced with permission from ref. 177. Copyright 2016, Nature Publishing Group. (d–f) Reproduced with permission from ref. 187. Copyright 2018, Wiley-VCH. (g) Reproduced with permission from ref. 188. Copyright 2018, Wiley-VCH. (h) Reproduced with permission from ref. 189. Copyright 2017, Royal Society of Chemistry.

electron conductivity of entire materials and buffered the volume variation of electrode materials upon cycling. Besides, the carbon coating could form a conductive network as schematically shown in Fig. 11e. The as-fabricated MnO_x@NC exhibits excellent cycling stability, higher capacity, and better rate capability in ZIBs (Fig. 11f).

Recently, our group applied MOF coating-derived composites in Zn–Co battery applications.[188] As schematically shown in Fig. 11g, the Zn–Co full battery was assembled by the anode of ZIF-8 coating-derived carbon coated ZnO with a Zn deposition layer (CC-ZnO@C-Zn) and the cathode of $CoMoO_4$ coated $Co(CO_3)_{0.5}(OH)_x{\cdot}0.11H_2O$ hierarchical structure grown on the carbon cloth (CC-CCH@CMO). The unique reconfiguration using functional electrodes showed the highest energy density and powder density compared with most recently reported flexible energy storage devices. In addition, Liu *et al.* developed a MOF-decorated separator for boosting the stable performance of Li metal electrodes.[189] The used MOF layer, NH_2-MIL-125(Ti), was coated onto a commercial polypropylene (PP) separator membrane to form a composite separator (Fig. 11h). Due to the interactions between the amine groups in NH_2-MIL-125(Ti) and the ions in the electrolyte, uniform electrochemical deposition of Li could be achieved. Therefore, when using the NH_2-MIL-125(Ti) MOF coated separator, the assembled Li|Cu cells exhibited greatly enhanced CE and stability.

4.2 Supercapacitors

Supercapacitors (SCs) are one of the most promising devices for next-generation high-performance energy storage. They can instantaneously provide a higher power density than batteries and store more energy than conventional capacitors, and thus have attracted intense investigations. Compared with conventional electrode materials, MOF materials have been widely studied as a newly emerging type of electrode materials.[45,46,190,191] Although bare MOFs can provide abundant active sites and thus facilitate fast ion diffusion, the supercapacitor performance is largely hindered by their intrinsically poor electrical conductivity. Generally, two strategies, forming composites with conductive materials and synthesizing conductive MOFs, are adopted to solve this problem.[192–197] For instance, Wang *et al.* designed ZIF-67 coated on conductive polyaniline (PANI) grown on the carbon cloth (PANI-ZIF-67-CC, Fig. 12a).[198] After interweaving MOF particles with conductive PANI, an obvious electrochemical double-layer was obtained, which was due to the simultaneous existence of ions and electrons on MOF surfaces (Fig. 12b). Therefore, the PANI-ZIF-67 composite exhibited unprecedented high areal capacitance, surpassing most previously reported SCs that are based on graphene, conductive polymers, metal oxides and so on. Directly coating conductive MOFs on substrates could also obtain high SC performances. Li *et al.* reported conductive Cu-CAT (conductivity as high as 20 S m^{-1}) grown on the carbon fiber paper (CFP, Fig. 12d and e).[65] As shown in Fig. 12f, the SC performance of the conductive MOF coated CFP obviously outperformed the low conductive MOF materials such as UiO-66, ZIF-8, and ZIF-67, which was attributed to the high electron transport of such a conductive framework and fast ion diffusion inside the pores, which induces its high capacitance. In addition, Nguyen *et al.* reported 2D conductive $Ni_3(HITP)_2$ nanosheets on nickel foam substrates by electrophoretic deposition, exhibiting extraordinary cycling stability of 84% retention after 100 000 cycles in a supercapacitor.[199] Recently, to combine the merits of both conductive MOFs and conductive polymers, Hou *et al.* integrated the hybrid architecture of conductive Cu-CAT MOF nanowire arrays into the freestanding polypyrrole substrate, displaying exceptional areal capacitance, excellent cycling capability and mechanical flexibility for all-solid-state flexible supercapacitors.[200] Therefore, based on the above-mentioned results, the electrochemical performances are attributed to these all-in-one electrodes without any binder or conductive additives, which show great potential in the direct application of MOFs in supercapacitors.

Despite the fact that excellent SC performances have been achieved based on conductive MOF coated composites, their practical applications is hindered by their high cost unless cheap conductive MOF materials are discovered. Therefore, the MOF coating-derived carbon-based materials have gained more attention. Tang *et al.* designed the functionalized nanoporous hybrid carbon composite by direct pyrolysis of core/shell ZIF-8@ZIF-67 (Fig. 12g and h).[55] The obtained carbon composite consisted of high-content nitrogen-doped carbon (NC) cores and highly graphitic carbon (GC) shells. This unique architecture endowed the NC@GC composite with integrated functions and synergistic advantages, providing a distinguished electrochemical performance in SCs (Fig. 12i). Another application of MOF coating derived carbon materials is to serve as a modified layer on traditional inorganic materials and synergistically realize high SC performances. For example, Weng *et al.* fabricated MOF (ZIF-8)-derived microporous carbon coated on MoS_2 nanosheets (MoS_2@MPC) for supercapacitors (Fig. 12j and k).[201] This resulting composite takes the advantages of the electrostatic double-layer electrolyte ion storage on the carbon coating and the high-capacitance pseudocapacitive properties of the MoS_2 core. The MoS_2@MPC exhibited higher SC performance with high specific capacitance and rate capability, which were superior to those of individual MoS_2 or MPC, suggesting the advantages of MOF coating-derived carbon composites in SC applications (Fig. 12l).

4.3 Electrocatalysis

By virtues of their tunable porous structure, ultrahigh specific surface area, monodispersed active centers in the well-defined crystalline frameworks and combined advantages of both heterogeneous and molecular catalysts, MOFs have been receiving increasing attention as a highly versatile platform for various important electrocatalytic applications, such as oxygen evolution reaction (OER), hydrogen evolution reaction (HER) and CO_2 electrochemical reduction.[202–209] Generally, these MOF-based composites are hybridized with a secondary conductive phase, such as conductive metal foam, graphene sheets and MXenes. For example, as shown in Fig. 13a and b, Duan *et al.* fabricated nickel–iron-based MOF (NiFe-MOF) arrays coated on the nickel foam, and such a NiFe-MOF consisted of an organic hydrocarbon (2,6-naphthalenedicarboxylic group) and inorganic metal–oxygen-layers.[59] The obtained NiFe-MOF arrays possessed an ultrathin

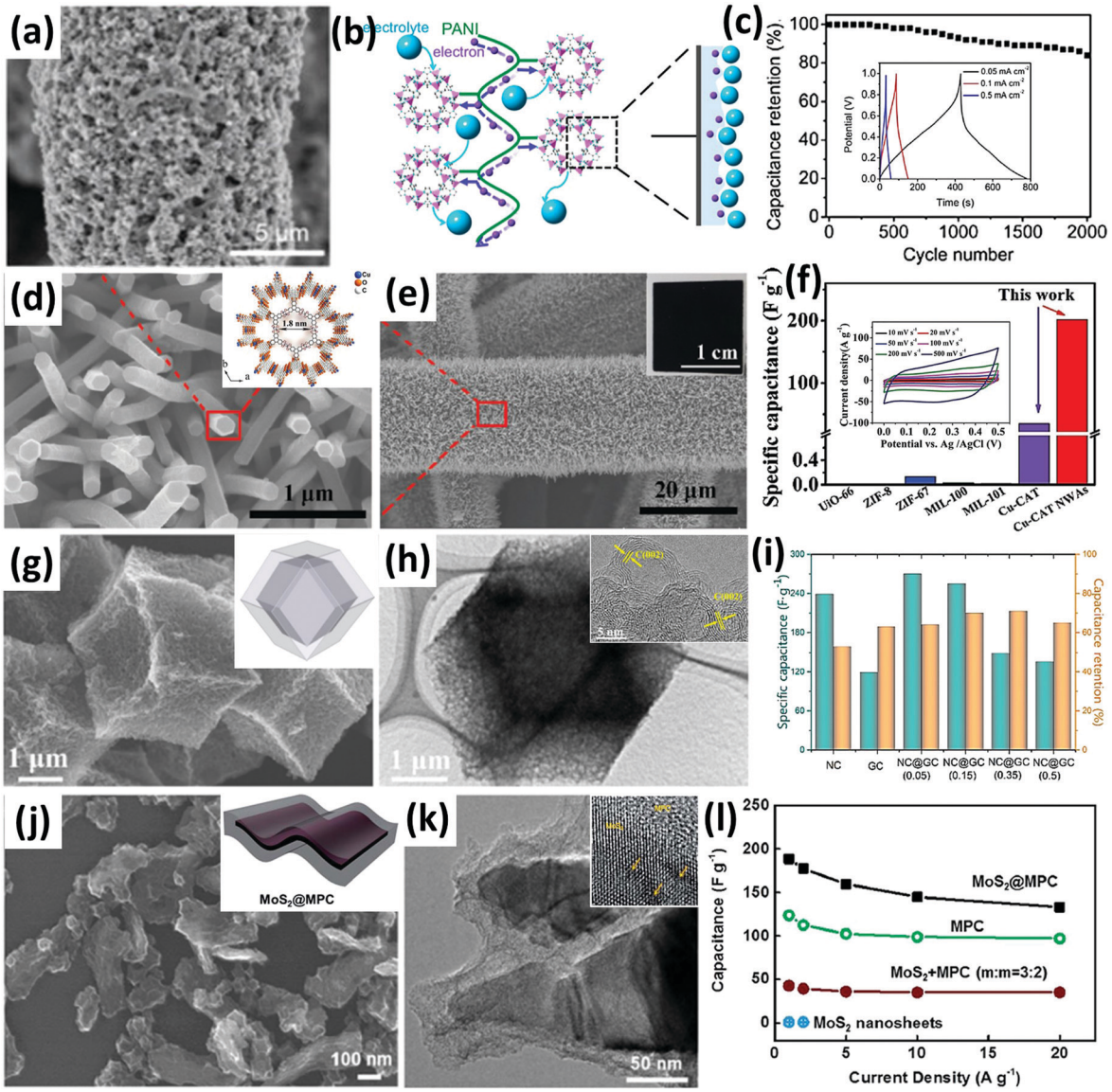

Fig. 12 (a) SEM image of carbon fibers after coating with ZIF-67 and after electro-polymerization of aniline. (b) Schematic representation of electron and electrolyte conduction in a MOF interwoven by PANI. (c) Cycling performance of the solid-state supercapacitor device measured at 0.1 mA cm^{-2} for 2000 cycles and (inset) galvanostatic charge/discharge curves of the solid-state supercapacitor device at different current densities. (d and e) SEM images of the Cu-CAT NWAs growing on carbon fiber paper. The insets in (c) and (d) are the crystal structure of Cu-CAT and the photographic image, respectively. (f) Comparison of the specific capacitances of the electrodes of different MOF materials and (inset) CV curves of the Cu-CAT NWAs electrode in a three-electrode cell. (g) SEM image of graphitic carbon and (inset) its schematic diagram. (h) TEM image of graphitic carbon and (inset) its HRTEM image. (i) The specific capacitance values obtained at a current density of 2 A g^{-1} and the respective capacitance retention ratios at a higher current density of 10 A g^{-1}. (j) SEM image of MoS_2@MPC and (inset) its schematic diagram. (k) TEM image of MoS_2@MPC and (inset) its HRTEM image. (l) Specific capacitances of the MoS_2@MPC sample, MPC, the mixture of MoS_2 and MPC and MoS_2 nanosheets. (a–c) Reproduced with permission from ref. 198. Copyright 2015, American Chemical Society. (d–f) Reproduced with permission from ref. 65. Copyright 2017, Wiley-VCH. (g–i) Reproduced with permission from ref. 55. Copyright 2015, American Chemical Society. (j–l) Reproduced with permission from ref. 201. Copyright 2015, Royal Society of Chemistry.

sheet structure (~3.5 nm thickness), high electrical conductivity of nickel foam, and hierarchical porosity, and the MOF materials had inherent molecular metal centers as active sites. After coating NiFe-MOF arrays on the bare nickel foam, the NiFe-MOF arrays exhibited significantly enhanced electrocatalytic performances towards alkaline HER and OER (Fig. 13c), such as high activity (overpotentials of 240 and 134 mV at 10 mA cm^{-2} for OER and HER, respectively), fast reaction kinetics and good durability (20 000 s for OER and 2000 s for HER). In the end, the electrolytic cell assembled by two NiFe-MOF arrays showed a low applied cell voltage of 1.55 V to sustain 10 mA cm^{-2} and stable water splitting performance which outperformed the Pt/C + IrO_2-based cell and demonstrated its practical applications. Chen *et al.* developed novel sublimation-vapor phase pseudomorphic transformation (CVPT) methodology to obtain the template-directed NiFe-MOF arrays coated on the nickel foam (NiFe-MOF@NF).[210] This strategy

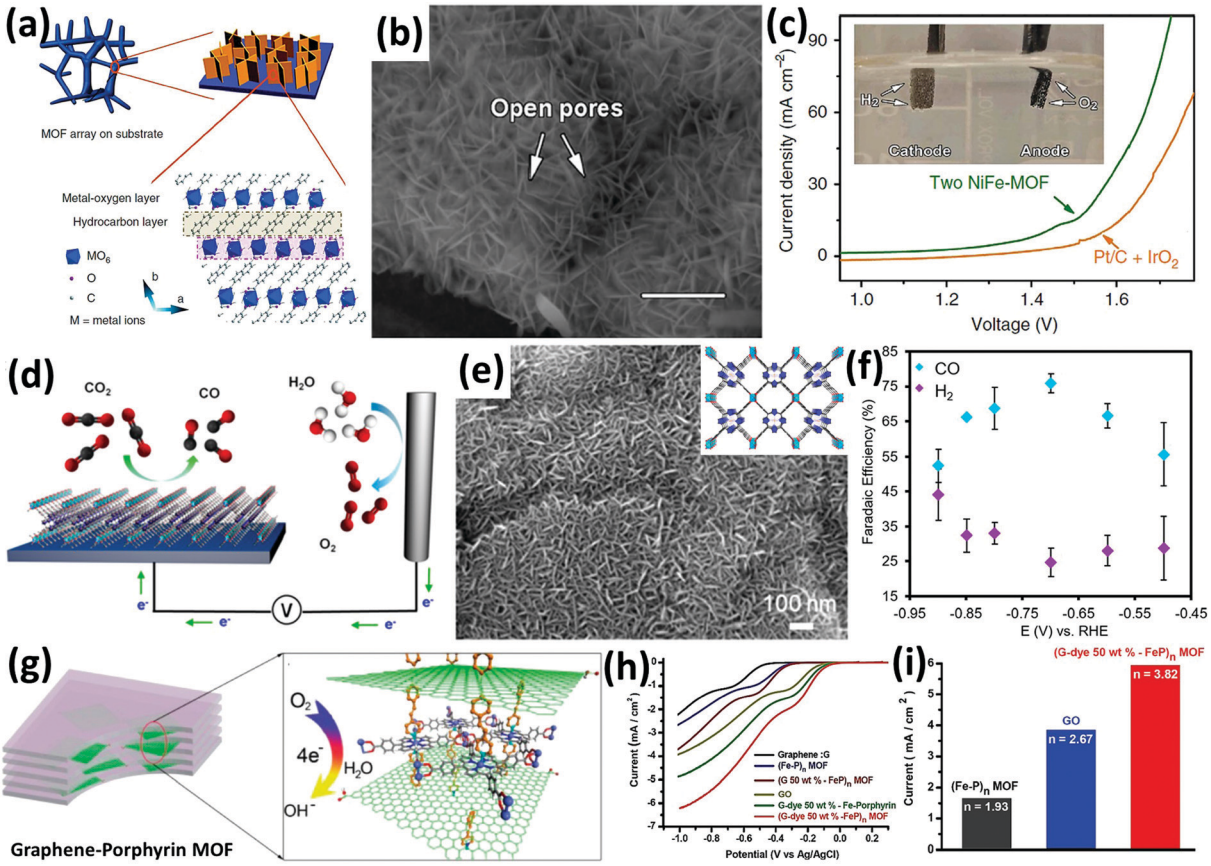

Fig. 13 (a) Schematic diagram and (b) SEM image of the NiFe-MOF array. (c) Water splitting performances of two NiFe-MOF electrodes and Pt/C + IrO_2 obtained at 10 mV s^{-1} in 0.1 M KOH and (inset) photograph of the NiFe-MOF electrodes at 1.6 V. (d) Schematic diagram of the integrated MOF on a conductive substrate to achieve a functional CO_2 electrochemical reduction system. (e) SEM image of the MOF catalyst film before electrolysis and (inset) the 3D MOF assembled by cobalt-metalated TCPP. (f) The selectivity for each product tested over −0.5 to −0.9 V *vs.* RHE. (g) Schematic diagram of the graphene–porphyrin MOF. (h) ORR performances at a rotation rate of 2000 rpm in O_2-saturated 0.1 M KOH. (i) Electrochemical activity given as the fully diffusion-limited current density (J_K) at −0.65 V. (a–c) Reproduced with permission from ref. 59. Copyright 2017, Nature Publishing Group. (d–f) Reproduced with permission from ref. 211. Copyright 2015, American Chemical Society. (g–i) Reproduced with permission from ref. 52. Copyright 2012, American Chemical Society.

could be widely extended and could transform oxides, hydroxides and polyoxometalates into MOF materials, demonstrating a viable plan to fabricate MOF arrays@substrate. Besides, this work also highlights the advantages of the perfect precursor morphology for the MOF@substrate catalyst, demonstrating its effectively enhanced OER performance.

Electrochemical conversion of atmospheric CO_2 into energy-dense carbon compounds is also an important reaction to provide carbon-neutral energy, in which high-efficiency electrocatalysts are the key to achieve such a target. Kornienko *et al.* designed a 3D MOF coated on a substrate to obtain a functional electrochemical CO_2 reduction system (Fig. 13d).[211] The selected 3D MOF was assembled by a nanosheet-structure [$Al_2(OH)_2$TCPP-Co] MOF (TCPP = 4,4′,4″,4‴-(porphyrin-5,10,15,20-tetrayl)tetrabenzoate) with a ultrathin structure and integrated on a conductive substrate (Fig. 13e). As a result, such a MOF@substrate composite exhibited high current selectivity for CO reaching up to 76% at −0.7 V *vs.* RHE (Fig. 13f). Besides, Jahan *et al.* also obtained a graphene–porphyrin MOF composite (Fig. 13g–i).[52] Further, when applied in alkaline ORR, the functional graphene–porphyrin MOF composite exhibited much higher selectivity for ORR and greatly reduced methanol crossover effects compared to noble Pt-based electrocatalysts.

Despite the fact that some advances have been achieved using MOF@substrate composites, the applied MOF materials are limited due to their instability in strong acid or alkali environments. By use of this feature, Zhang *et al.* fabricated defect-rich 2D material networks based on unstable MOF materials.[212] The Co-MOF nanosheet arrays on the nickel foam (Co-MOF@NF) were first prepared *via* the coordination reaction of Co^{2+} and 2-methylimidazole at room temperature, and then the defect-rich ultrathin $Co(OH)_2$@NF was obtained *via in situ* etching treatment. Due to the nanosized grains (sub-5 nm) and thus abundant boundaries, the as-fabricated $Co(OH)_2$/NF maximally exposed the amount of active sites to electrocatalysis reactions, which endows 3–4 times higher OER activity than that of the commercial RuO_2. Besides, the Co-MOF could be coated on various substrates (such as carbon cloth, glass beaker wall and titanium mesh) and the components of MOF could be adjustable (such as heteroatom doping or substitution). Therefore, this work

highlights the unique synthetic route to MOF@substrate derived defect-rich hierarchical catalyst arrays with abundant boundaries, tunable chemical compositions on versatile substrates and potential applications.

In other respects, similar to the battery applications, the more popular MOF-derived coating-based composites also possess potential for application in electrocatalysis due to their unique structure and robust durability.[213–222] Recently, Wu *et al.* reported a salt-template method to realize the successful transformation from ZIF-67 coating to monodispersed cobalt atoms anchored on nitrogen-doped graphene-like carbon (SCoNC) with a high loading of around 15.3% (Fig. 14a).[219] In addition, the obtained SCoNC nanosheets had good dispersibility in deionized water. The high loading of single Co atoms was definitively confirmed by the "Z-contrast" HAADF-STEM image (Fig. 14b). Benefiting from its ultrathin structure and high metal loading content, the SCoNC catalyst exhibited a more positive half-wave potential (0.91 V *vs.* RHE) than that of Pt/C (0.88 V), demonstrating its superior ORR activity (Fig. 14c). Besides, the thin MOF coating could be effectively *in situ* formed on the surface of various oxides by a low-pressure vapor superassembly strategy proposed by our group.[122] After heat treatment, the metal-based composites with several nanometer-thickness carbon coating were fabricated. The carbon-coated core–shell catalyst, with N-doped carbon coated CoNi (CoNi@NC) nanowire arrays as an example, possessed tunable HER and OER performance *via* adjusting the temperature parameters (Fig. 14d–f). In addition, Liu *et al.* developed a self-sacrificial template method to fabricate Co_3S_4/MOF hybrids coated on conductive carbon cloth (Co_3S_4/MOF/CC), which were derived from vapor phase synthesized Co-MOFs/CC and its surface vulcanization.[223] The obtained Co_3S_4/MOF/CC exhibits remarkable HER and OER activities, with small overpotentials of 84 and 226 mV at 10 mA cm^{-2}, respectively. Jia *et al.* developed 3D tri-functional hierarchical electrocatalysts *via* controlled pyrolysis of a ZIF-67 thin film coated on a 3D macroporous polymeric substrate (Fig. 14g and h).[224] Taking the application in ORR

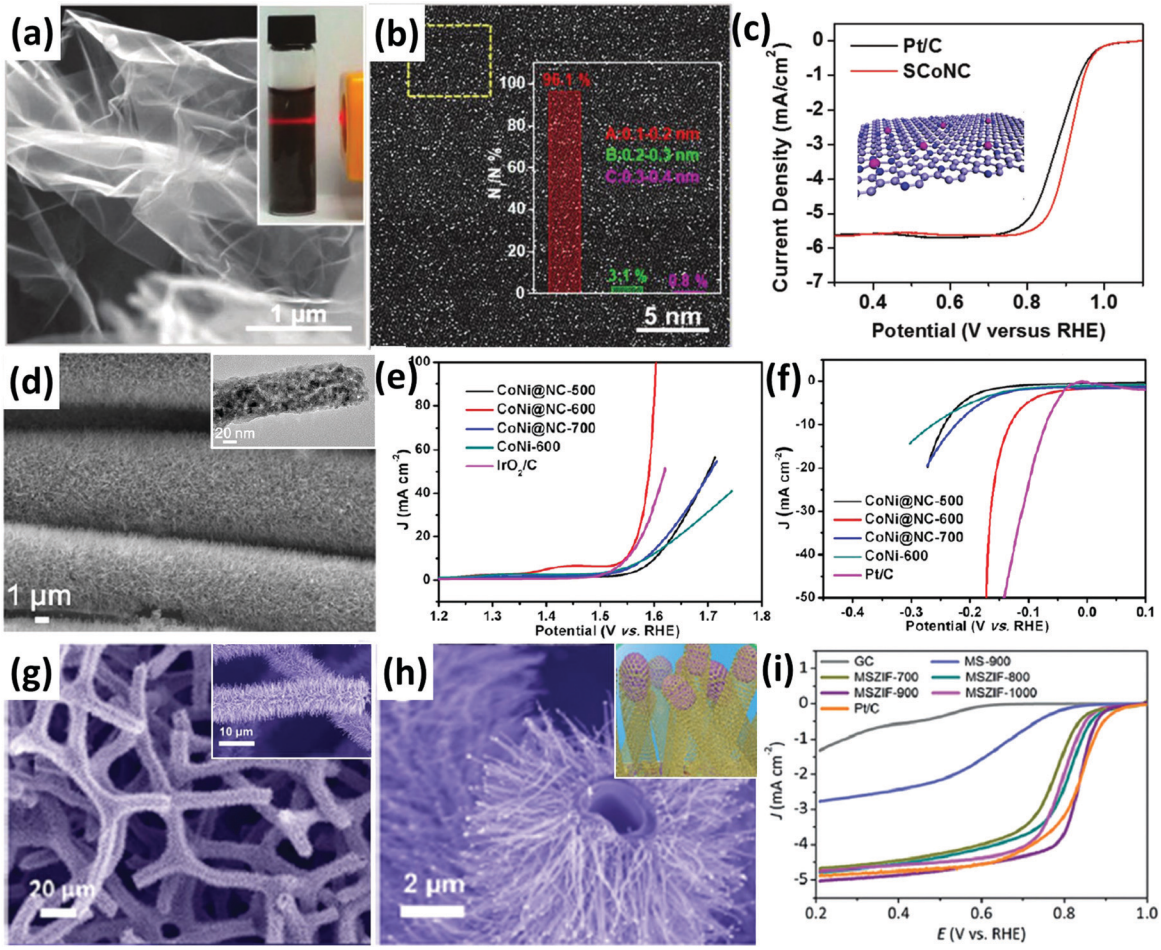

Fig. 14 (a) SEM image of the SCoNC catalyst. (b) High-resolution HAADF-STEM image of SCoNC, where the white dots represent Co atoms. (c) LSV curves of SCoNC and commercial Pt/C at a scan rate of 5 mV s^{-1} and 1600 rpm. (d) SEM image of CoNi@NC nanowire arrays on carbon cloth and (inset) TEM image of a single CoNi@NC nanowire. (e) OER and (f) HER performances in 1 M KOH at 5 mV s^{-1}. (g) SEM images of ZIF-67 thin film on melamine sponge (MS) treated at 900 °C (denoted as MSZIF-900) with (inset) an enlarged SEM image. (h) The enlarged SEM image of MSZIF-900 and (inset) its schematic diagram. (i) ORR polarization curves for the various electrocatalysts at 1600 rpm in N_2- and O_2-saturated 0.1 M KOH. (a–c) Reproduced with permission from ref. 219. Copyright 2019, Wiley-VCH. (d–f) Reproduced with permission from ref. 122. Copyright 2017, American Chemical Society. (g–i) Reproduced with permission from ref. 224. Copyright 2017, Wiley-VCH.

as an example, the obtained electrocatalyst exhibited comparable onset potential and half-wave potential to those of the commercial Pt/C catalyst (Fig. 14i). These illustrational works demonstrate potential water splitting and ORR applications based on MOF or MOF-derived coatings. For clarity, we have systematically summarized the HER/OER or ORR applications of these functional catalysts in Table 3.[59,79,82,84,122,204,205,210,212–215,223–230]

In conclusion, this part demonstrates the comparable electrocatalysis applications of composites containing the MOF coatings or MOF-derived carbon coatings for high-efficiency energy conversion performances in terms of abundant active sites, low overpotential, large catalytic current, and robust catalytic/component stability. These composites are considered as a kind of material with great potential, and are gradually being excavated and explored. For the MOF coated catalysts, the enormous molecular metal sites as catalytic centers, the thin coating layer with a highly exposed active area, as well as tunable porosity are attributed to their high catalytic performances. For the composite electrocatalysts containing MOF-derived carbon coatings, the high electron conductivity, numerous nanopores, and a robust heterogeneous shell endow the composites with abundant active sites, fast electron transport, good catalytic/component stability and synergistic tuning effect within the core–shell structure. The excellent electrocatalytic performances of these MOF coating/MOF coating-derived systems demonstrate their potential as candidates for various catalytic applications.

4.4 Gas separation

Gas separation is a critical industrial and energy intensive process for separating components of chemical mixtures in many fields.[231,232] Particularly, gas mixtures with similar properties are difficult to be well separated. Although much progress has been made, the development of high-performance gas separation materials and better processing/fabrication techniques is highly desired to achieve high separation efficiency and low cost. For microporous inorganic materials (*e.g.* carbon molecular sieves, zeolites, *etc.*), it is difficult to simultaneously realize high adsorption capacity (or permeability) and high selectivity for separating challenging gas mixtures, greatly restricting their separation efficiency. In addition, the number of crystal structures of zeolites and amorphous pore structures of carbon molecular sieves make them difficult to generalize. In the past decade, MOFs have attracted great interest for gas separation, which is attributed to two main characteristics as follows: (1) their pores can be rationally controlled by modulating both inorganic metal ions and organic linkers, and (2) their pore surfaces can be easily modified with abundant functional groups through a variety of approaches.[233–237] Generally, the gas separation is based on the size and shape of different molecules in gas mixtures, or on their interactions (*e.g.* hydrogen-bond interactions, van der Waals interactions, molecule interactions) with specific metals and organic linker molecules in MOFs.[238–244] For example, Cui *et al.* designed unique new MOFs with hexafluorosilicate for the purpose of preferential binding/interaction and orderly assembly of acetylene molecules, thus displaying high adsorption capacity and high selectivity from ethylene.[245] Researchers designed and constructed pore chemistry and size in functional MOFs for the separation of gas molecules of different sizes. In addition, to realize high separation selectivity, the development of high-quality and uniform MOF membranes/coatings on substrates is of great significance for large-scale industrial applications. Table 4 presents most of the examples of MOF membranes for gas separation.[62,246–262] Some typical examples are discussed in detail as follows.

To obtain high-quality and uniform MOF membranes, Tao *et al.* developed a hollow ceramic fiber supported ZIF-8 membrane *via* a hot dip-coating seeding method and subsequent secondary growth.[246] The key point for the synthesis of a uniform ZIF-8 membrane is the formation of a uniform and continuous ZIF-8 seed layer on preheated hollow ceramic fibers, which further induced the subsequent secondary growth. After secondary synthesis, the SEM image showed a compact ZIF-8 membrane without pinholes and cracks on the hollow ceramic fibers (Fig. 15a). Moreover, the SEM image from the cross section indicated good contact between the membrane layer and the support (Fig. 15b). Further, single gas permeation experiments for H_2, CH_4, N_2, O_2 and CO_2 were carried out to investigate its gas separation performance. As shown in Fig. 15c, the gas permeance sequence is $H_2 > CO_2 > O_2 > N_2 > CH_4$. The kinetic diameters of H_2, CO_2, O_2, N_2 and CH_4 are 0.289, 0.33, 0.346, 0.364, and 0.38 nm, respectively. The gas permeance sequence is inversely proportional to their kinetic diameter sequence, demonstrating a molecular sieving behaviour for the ZIF-8 membrane. This phenomenon is attributed to the intrinsic periodic frameworks of ZIF-8. ZIF-8 possesses a pore aperture of 0.34 nm, which is larger than the kinetic diameter of H_2 (0.289 nm), but smaller than that of N_2 (0.364), O_2 (0.346), and CH_4 (0.38 nm). Moreover, because of the size and shape of different molecules in gas mixtures, the ideal selectivity for H_2/CO_2, H_2/O_2, H_2/N_2 and H_2/CH_4 is calculated to be 5.4, 7.1, 9.2 and 10.8, respectively. The permeability of H_2 is up to 7.29×10^{-7} mol m^{-2} s^{-1} Pa^{-1}. However, due to the similar kinetic diameter of N_2 and O_2, the ZIF-8 membrane showed poor O_2/N_2 (1.3) selectivity. Therefore, in addition to the microstructure effect, the synthesized high-quality membrane without macroporous defects also plays an important role in its excellent H_2 selectivity.

Recently, Ma *et al.* designed and constructed a high-quality ZIF-8 membrane *via* a typical solid–gas method.[62] Well-known and easily-scalable α-alumina macroporous substrates coated with a ~5 mm γ-alumina mesoporous layer were used as supports. After 10 ALD cycles, the formed ZnO mainly existed at the top 200 nm of the γ-alumina layer and no signals were detected in the α-alumina layer. This phenomenon was attributed to the preferential deposition of ZnO outside the pores of the support. As shown in Fig. 15d, the high-magnification cross-sectional images showed that Zn distribution changed substantially because of the partial transformation from ZnO to ZIF after the mIm-vapor treatment. The mobility and diffusion of ALD-deposited ZnO throughout the 5 mm γ-alumina mesoporous layer are attributed to the *in situ* reconstruction during mIm-vapor treatment. As shown by the open symbols of Fig. 15e, along with increasing ALD cycles for ZnO, the propylene permeance gradually decreases. After 10 ALD cycles, the ZnO–alumina

Table 3 A summary of functional composites based on MOF/MOF-derived coatings for HER/OER and ORR

MOF/MOF-derived coatings	Synthesis methods for MOF coatings	Application	Activity; Tafel slope or TOF	Stability	Electrolyte	Ref.
NiFe-MOF@NF	Solid–gas method	OER	275.38 mV at 10 mV cm^{-2} and 318.38 mV at 50 mV cm^{-2}; 47 mV dec^{-1}	10 h at 10 mV cm^{-2}	1 M KOH	210
Co_3S_4/MOF/CC	Solid–gas method	HER	84 mV at 10 mA cm^{-2} and 183 mV at 100 mV cm^{-2}; 82 mV dec^{-1}	2000 CV cycles	Hydrogen-saturated 1 M KOH (30 °C)	223
		OER	226 mV at 10 mA cm^{-2} and 336 mV at 100 mV cm^{-2}; 132 mV dec^{-1}	2000 CV cycles	Nitrogen-saturated 1 M KOH (30 °C)	
		Symmetrical water splitting	Cell voltage of 1.55 V at 10 mA cm^{-2}	Chronopotentiometry test for 24 h; 3000 CV cycles	1 M KOH	
$Co(OH)_2$@NF (derived from Co-MOF@NF)	Liquid–liquid method	OER	223 mV at 10 mA cm^{-2} and 30.8 mV cm^{-2} at η of 300 mV; 131 mV dec^{-1}	20 h at 20 mA cm^{-2}	Argon-saturated 1 M KOH	212
NiFe-MOF@NF	Liquid–liquid method	OER	240 mV at 10 mA cm^{-2}; 34 mV dec^{-1}	20 000 s at 1.42 V *vs.* RHE	0.1 M KOH	59
		HER	134 mV at 10 mA cm^{-2}; TOF of 2.8 s^{-1} at η of 400 mV	2000 s at −0.2 V *vs.* RHE		
		Symmetrical water splitting	Cell voltage of 1.55 V at 10 mA cm^{-2}	20 h at 1.5 V		
CoNi@NC/CC (derived from CoO-NiO@ZIF/CC)	Solid–gas method	OER	317 mV at 10 mA cm^{-2} and 374 mV at 100 mV cm^{-2}; 59.3 mV dec^{-1}	40 000 s at 10 mA cm^{-2}	1 M KOH	122
		HER	132 mV at −10 mA cm^{-2}; 109.1 mV dec^{-1}	40 000 s at −10 mA cm^{-2}		
		Symmetrical water splitting	Cell voltage of 1.678 V at 10 mA cm^{-2}	70 000 s at 10 mA cm^{-2}		
MSZIF-900 (ZIF-67 thin film on melamine sponge)	Liquid–liquid method	OER	337 mV at 10 mA cm^{-2}	20 000 s at 10 mA cm^{-2}	1 M KOH	224
		HER	233 mV at 10 mA cm^{-2}	>80 000 s at 10 mA cm^{-2}	0.5 M H_2SO_4	
		ORR	Onset potential of 0.92 V *vs.* RHE; half-wave potential of 0.72 *vs.* RHE	>60 000 s at 0.6 V *vs.* RHE	O_2-Saturated 0.5 M H_2SO_4	
			Onset potential of 0.91 V *vs.* RHE; half-wave potential of 0.84 *vs.* RHE	>60 000 s	O_2-Saturated 0.1 M KOH	
CNT-NC-CoP (derived from ZIF-67 coated on CNT)	Liquid–liquid method	OER	251 mV at 10 mA cm^{-2}; 82.1 mV dec^{-1}	10 h at 10 mA cm^{-2}	1 M KOH	225
HC800 (derived from Ni/Mo-containing MOF)	Liquid–liquid method	HER	123 mV at 10 mA cm^{-2}; 83 mV dec^{-1}	7200 s at η of 230 mV	1 M KOH	215
Co-N-C nanowire network-800 (derived from MOF@cellulose)	Liquid–liquid method	OER	470 mV at 10 mA cm^{-2}; 191 mV dec^{-1}	—	O_2-Saturated 0.1 M KOH	214
		ORR	Onset potential of 1.05 V *vs.* RHE; limiting current density of 6.3 mA cm^{-2}	50 000 s at 0.6 V *vs.* RHE		
MoO_2-Ni@NC/CC (derived from MoNi-2-mim/CC)	Liquid–liquid method	HER	58 mV at 10 mA cm^{-2}; 35.1 mV dec^{-1}	80 000 s in all at −10 and −20 mA cm^{-2}	0.5 M H_2SO_4	226
FeNi@NC/rGO (derived from MOF/GO)	Liquid–liquid method	OER	261 mV at 10 mA cm^{-2}; 40 mV dec^{-1}	120 h in all at 10, 50 and 100 mA cm^{-2}	1 M KOH	213
Co/NC (derived from polystyrene@ZIF-67)	Liquid–liquid method	ORR	Half-wave potential of 0.87 *vs.* RHE	24 h at 0.5 V *vs.* RHE	O_2-Saturated 0.1 M KOH	79
Fe/Ni-BTC@NF	Liquid–liquid method	OER	270 mV at 10 mA cm^{-2}; 47 mV dec^{-1}	15 h at η of 300 mV	0.1 M KOH	205
Co-Mo_2N (derived from ZIF-67/Mo-MOFs)	Liquid–liquid method	HER	76, 106, 167 and 240 mV at 10, 20, 50 and 100 mA cm^{-2}, respectively; 47 mV dec^{-1}	48 h at η of 76 mV	1 M KOH	82
		OER	302, 334, 400 and 485 mV at 10, 20, 50 and 100 mA cm^{-2}, respectively; 90 mV dec^{-1}	24 h at 10 mA cm^{-2}		
		Symmetrical water splitting	Cell voltage of 1.576, 1.671 and 1.832 V at 10, 20 and 50 mA cm^{-2}, respectively	2000 CV cycles		
Ni-MOF@Fe-MOF	Liquid–liquid method	OER	265 mV at 10 mA cm^{-2}; 82 mV dec^{-1}	1000 CV cycles	O_2-Saturated 1 M KOH	204
Graphene-based nitrogen-doped porous carbon sheets (derived ZIF-8/GO)	Liquid–liquid method	ORR	Onset potential of 0.957 V *vs.* RHE; current density of −6 mA cm^{-2} at 0.45 V *vs.* RHE	28 000 s at −0.4 V *vs.* RHE	O_2-Saturated 1 M KOH	84

Table 3 (*continued*)

MOF/MOF-derived coatings	Synthesis methods for MOF coatings	Application	Activity; Tafel slope or TOF	Stability	Electrolyte	Ref.
NC-Co/CoN$_x$@carbon fiber (derived from Co-ZIF@carbon fiber)	Liquid–liquid method	OER ORR	289 mV at 10 mA cm^{-2}; 82 mV dec^{-1} Onset potential of 0.928 V *vs.* RHE; half-wave potential of 0.878 *vs.* RHE	— —	1 M KOH	227
Cobaloxime-based MOF@glassy carbon (GC)	Liquid–liquid method	HER	Onset potential of ~−0.15 V *vs.* RHE; 250 mV dec^{-1}	18 h at 1.7 mA cm^{-2}	Acetate buffer at pH 4	228
NU-1000_Ni-S coated on FTO (NU-1000: a Zr-based MOF)	Liquid–liquid method	HER	238 mV at 10 mA cm^{-2}; 111 mV dec^{-1}	2 h at 10 mA cm^{-2}	0.1 M HCl (pH 1)	229
Lattice-strained NiFe MOFs/NF	Liquid–liquid method	ORR	Onset potential of 0.92 V *vs.* RHE; 70 mV dec^{-1}	200 h at −100 mA cm^{-2}	0.1 M O_2-saturated KOH	230
		OER	~210 mV at 200 mA cm^{-2}; 68 mV dec^{-1}	200 h at 200 mA cm^{-2}	0.1 M N_2-saturated KOH	

composite displayed a very low propylene permeance of 2×10^{-11} mol Pa^{-1} m^{-2} s^{-1}, indicating the complete block of propylene in the substrate by the abundant ZnO deposition. More interestingly, after the ligand-vapor treatment for the above impermeable 10-cycle ALD-modified supports, the propylene permeance ($>10^{-8}$ mol Pa^{-1} m^{-2} s^{-1}) and propylene/propane selectivity (~100) increased by three and two orders of magnitude, respectively (Fig. 15e and f). This phenomenon was mainly attributed to the ligand induced transformation from an impermeable to selective MOF membrane. Moreover, after being treated at 60 °C for 36 hours, the membrane still kept the room-temperature membrane performance, demonstrating its stable performance. In addition, through a conservative process-scale assessment, this liquid/gel-free, seed-free and all-vapor-phase synthesis approach towards high-performance membranes also show great potential for large-scale application.

Further, to improve the gas separation performance of the ZIF-8 membrane by modulating its intrinsic microstructure, Zhou *et al.* prepared a unique ZIF-8 membrane with suppressed linker mobility by a fast current-driven synthesis strategy.[263] After this current-driven synthesis for 20 min, the resulting ZIF-8 layer displayed a uniform thickness of approximately 200 nm. The resulting ZIF-8 membrane consists of a majority of the polymorph monoclinic ZIF-8_*Cm*. The structure of the resulting ZIF-8_*Cm* is obviously different from that of the normal flexible ZIF-8_*I*$\bar{4}$3*m* phase in the solvothermal route. This difference was mainly attributed to the inborn lattice distortion under the local *in situ* electric field, thus resulting in the formation of the stiff polymorph ZIF-8_*Cm*. Furthermore, the Wicke–Kallenbach technique was carried out to investigate the C_3H_6/C_3H_8 separation performance of the resulting ZIF-8 membranes. The ZIF-8 membranes grown for 20 min exhibit a high separation factor of 304.8 with a C_3H_6 permeance of 1.74×10^{-8} mol Pa^{-1} m^{-2} s^{-1}. In addition, on the basis of molecular dynamics simulations, the C_3H_6/C_3H_8 selectivity of ZIF-8_*Cm* was approximately 530, much higher than that of ZIF-8_*I*$\bar{4}$3*m* (~150), demonstrating the highly selective propene sieving. The superhigh selectivity of the polymorph ZIF-8_*Cm* was mainly attributed to its stiffened lattice, distinctly distinguishing it from the flexible ZIF-8_*I*$\bar{4}$3*m*. This current-driven synthesis strategy opens a new avenue for the large-scale synthesis of high-quality and high-performance MOF membranes for gas separation.

Recently, to address the permeability/selectivity trade-off, Song *et al.* designed and constructed a novel core/shell porous crystalline structure (denoted as MOF@ZIF) using a UiO-66-NH_2 core with a large pore size of ~0.6 nm and a ZIF-8 shell (pore size ~0.4 nm) (Fig. 15g).[262] The formation of the core–shell MOF@ZIF composite was based on a layer-by-layer solution deposition method. Benefiting from its intrinsic structures, the resulting core/shell architecture exhibited enhanced synergistic advantages *via* pore engineering: (1) the large-pore UiO-66-NH_2 core provides facilitated transport pathways for molecules; (2) small-pore ZIF and/or the generated smaller pores from the core–shell incommensurate pore overlapping greatly improve the molecular sieving properties. As a proof-of-concept application,

Table 4 A summary of MOF coatings on substrates for gas separation

MOF species	Pore size (Å)	Substrates	Synthesis strategies	Applications	Separation factors	Performance (mol m^{-2} s^{-1} Pa^{-1})	Ref.
ZIF-8	3.4	α-Al_2O_3 tubes	Liquid–liquid method	H_2	H_2/CO_2 (5.4) H_2/O_2 (7.1) H_2/N_2 (9.2) H_2/CH_4 (10.8)	7.29×10^{-7}	246
ZIF-7	3	α-Al_2O_3 disks	Liquid–liquid method	H_2	H_2/CO_2 (13.6) H_2/N_2 (18) H_2/CH_4 (14)	4.55×10^{-8}	247
ZIF-8	3.4	Nylon support	Liquid–liquid method	H_2	H_2/N_2 (4.3)	1.97×10^{-6}	248
ZIF-78	3.8	Porous ZnO	Solid–liquid method	H_2	H_2/CO_2 (9.5) H_2/N_2 (5.7) H_2/CH_4 (10.4)	1.00×10^{-7}	249
MIL-53	7.3–7.7	α-Al_2O_3 disks	Liquid–liquid method	H_2	H_2/CO_2 (4) H_2/N_2 (2.5)	5.00×10^{-7}	250
MOF-5	7.8	α-Al_2O_3 disks	Liquid–liquid method	H_2	H_2/CO_2 (4.1) H_2/N_2 (4)	4.30×10^{-7}	251
MOF-5	7.8	α-Al_2O_3 disks	Liquid–liquid method	H_2	H_2/CO_2 (2.5) H_2/N_2 (2) H_2/CH_4 (7)	8.00×10^{-7}	252
MOF-74	11	α-Al_2O_3 disks	Liquid–liquid method	H_2	H_2/CO_2 (9.1) H_2/N_2 (3.1) H_2/CH_4 (2.9)	1.00×10^{-5}	253
HKUST-1	9	α-Al_2O_3 disks	Liquid–liquid method	H_2	H_2/CO_2 (4.6) H_2/N_2 (3.7) H_2/CH_4 (3)	$4.0–6.0 \times 10^{-7}$	254
ZIF-8	3.4	α-Al_2O_3 tubes	Liquid–liquid method	CO_2	CO_2/CH_4 (7)	2.40×10^{-5}	255
ZIF-69	7.8	α-Al_2O_3 disks	Liquid–liquid method	CO_2	CO_2/CO (3.5)	3.60×10^{-8}	256
SIM-1	8	α-Al_2O_3 tubes	Liquid–liquid method	CO_2	CO_2/N_2 (4.5)	8.00×10^{-8}	257
Bio-MOF-14	1.6–4	α-Al_2O_3 tubes	Liquid–liquid method	CO_2	CO_2/CH_4 (3.5)	4.10×10^{-6}	258
ZIF-8	3.4	α-Al_2O_3 tubes	Liquid–liquid method	Propylene	Propylene/propane (59)	2.50×10^{-9}	259
ZIF-8	3.4	α-Al_2O_3 disks	Liquid–liquid method	Propylene	Propylene/propane (30)	1.12×10^{-8}	260
ZIF-8	3.4	α-Al_2O_3 disks	Liquid–liquid method	Propylene	Propylene/propane (55)	2.00×10^{-8}	261
ZIF-8	3.4	α-Al_2O_3 and γ-Al_2O_3	Solid–gas method	Propylene	Propylene/propane (100)	1.00×10^{-8}	62
UiO-66-NH_2@ZIF-8	6@3.4	Polysulfone membranes	Liquid–liquid method	CO_2	CO_2/N_2 (39)	45.2 barrer	262

the resulting MOF@ZIF nanocomposites were integrated to construct hybrid polysulfone (PSF) membranes for CO_2 capture. The kinetic diameters of CO_2 and N_2 are 0.33 and 0.364 nm, respectively, showing that these two molecules have a kinetic radius difference of less than 10%. These similar properties led to difficult gas separation. The optimized PSF-MOF@ZIF membranes displayed 710% higher CO_2 permeability (45.2 barrer) and 50% higher CO_2/N_2 selectivity (39) than pure PSF polymer membranes, indicating remarkable CO_2 separation performance (Fig. 15h). Therefore, the dual-channel core/shell MOF@ZIF as a filler endows the resulting hybrid PSF membrane with enhanced gas permeability and CO_2/N_2 selectivity simultaneously. In addition, this core–shell design strategy with synergistic permeability/selectivity properties can be applied to solve other challenging separation problems.

4.5 Gas adsorption and storage

MOFs have attracted great interest in gas adsorption and storage (*e.g.* hydrogen, carbon dioxide, methane and noble gases) due to their exceptionally high surface areas and structural diversity.[264–268] In the past decade, great endeavors have been dedicated to developing efficient strategies to improve the relatively weak physisorption forces. One typical approach is to explore and construct unique functional MOF materials by the modification of pore size and the introduction of coordinatively unsaturated metal sites. Li *et al.* demonstrated several MOFs with specific Lewis basic nitrogen sites *via* the introduction of pyridine, pyridazine, and pyrimidine groups into the organic linkers.[269] These well-designed MOFs displayed high total volumetric methane storage capacities of around 249–257 cm^3 (STP) cm^{-3} at room temperature and 65 bar. However, due to their intrinsic and limited physisorption forces, the gas adsorption and storage performances in pure MOF materials remain unsatisfactory for further practical applications. Another efficient and promising strategy is to construct unique metal nanomaterials confined in MOFs by combining the strong adsorption ability of metal nanomaterials and high surface areas of MOFs.[270] These as-prepared core–shell architectures can greatly improve the interaction with target adsorbates and thus achieve excellent gas adsorption and storage properties. Most traditional porous materials store gases by weak van der Waals interactions, while transition metals can efficiently adsorb gases *via* strong metallic bonding and dissociation processes. For example, Liu *et al.* demonstrated the successful deposition of Ag nanoparticles in porous Ni-based MOF-74, exhibiting a higher Xe adsorption capacity (15.6% improvement) at STP compared to pure Ni-based MOF-74.[271] This improved performance was mainly attributed to the stronger interactions between polarizable Xe molecules and Ag nanoparticles. In addition, the good contacts between nanostructured metal cores and MOF coatings in well-designed core–shell composites have a great influence on their gas adsorption and storage performance.

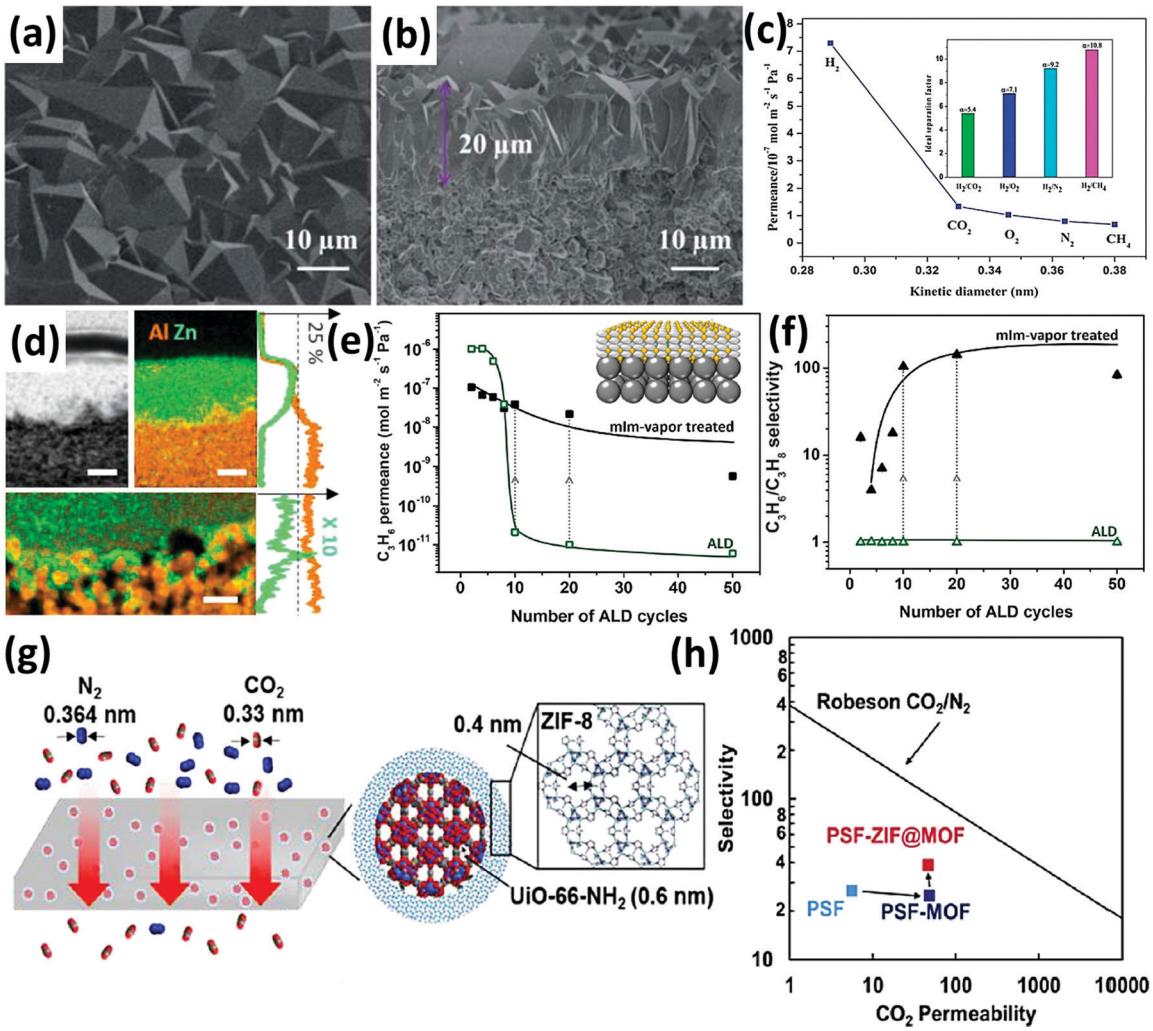

Fig. 15 (a and b) Top and cross-section views of the ZIF-8 membrane after secondary growth. (c) Single gas permeation properties of the as-prepared ZIF-8 membrane (inset: ideal separation factors for H_2 over CO_2, O_2, CH_4 and N_2). (d) Cross section analysis with ADF-STEM imaging after mIm ligand-vapor treatment, and the corresponding spatial distribution of aluminum (orange) and zinc (green). Zinc signal has been amplified 10 times for the γ-Al_2O_3/α-Al_2O_3 section for visibility. (e and f) Propylene permeance and propylene/propane single component selectivity of ZIF-8/γ-alumina nanocomposite membranes as a function of the number of ALD cycles (solid symbols). (g) Schematic illustration of core/shell UiO-66-NH_2@ZIF-8 as engineered fillers in hybrid polysulfone membranes for highly selective CO_2 separation. (h) CO_2/N_2 gas selectivity of UiO-66-NH_2, ZIF-8 and UiO-66-NH_2@ZIF-8 in hybrid PSF membranes. (a–c) Reproduced with permission from ref. 246. Copyright 2013, Royal Society of Chemistry. (d–f) Reproduced with permission from ref. 62. Copyright 2018, American Association for the Advancement of Science. (g and h) Reproduced with permission from ref. 262. Copyright 2017, American Chemical Society.

Palladium has attracted great interest as an ideal metal candidate for hydrogen storage and hydrogen-related catalytic reactions because of its intrinsic strong bonding with hydrogen.[272–274] To further improve the hydrogen storage properties of pure Pd, Li *et al.* designed and constructed as-prepared Pd nanocrystals confined in HKUST-1 (denoted as Pd@HKUST-1) with remarkably enhanced capacity and speed of hydrogen storage by a facile liquid–liquid synthesis method.[40] During the typical synthesis process, the Pd nanocrystals as seed sites oriented the growth of MOF coatings in the precursor solution (Fig. 16a). The TEM image showed that Pd nanocubes were well distributed in the HKUST-1 crystals (Fig. 16b). Furthermore, PC isotherm measurements at 303 K and 101.3 kPa were carried out to study the hydrogen storage properties of pure Pd and Pd@HKUST-1 samples (Fig. 16c). The numbers of hydrogen atoms per Pd atom for both of them were compared. Pd@HKUST-1 exhibited a higher total amount of hydrogen absorption of 0.87 H per Pd atom than bare Pd nanocubes (0.5 H per Pd atom). In addition, when comparing with their PC curves, Pd@HKUST-1 displayed a fully reversible absorption/desorption response, while bare Pd nanocubes showed an obvious hysteresis behavior, confirming an improved hydrogen absorption/desorption speed from outer HKUST-1 coating. To reveal the superior performance of Pd@HKUST-1, *in situ* XRD measurements were performed to detect the structural change of bare Pd nanocubes and Pd@HKUST-1 during the hydrogen absorption/desorption process. Along with the increase of H_2 concentration from 0 to 101.3 kPa, the two samples experienced Pd phase transition from the solid solution (α-phase) to the

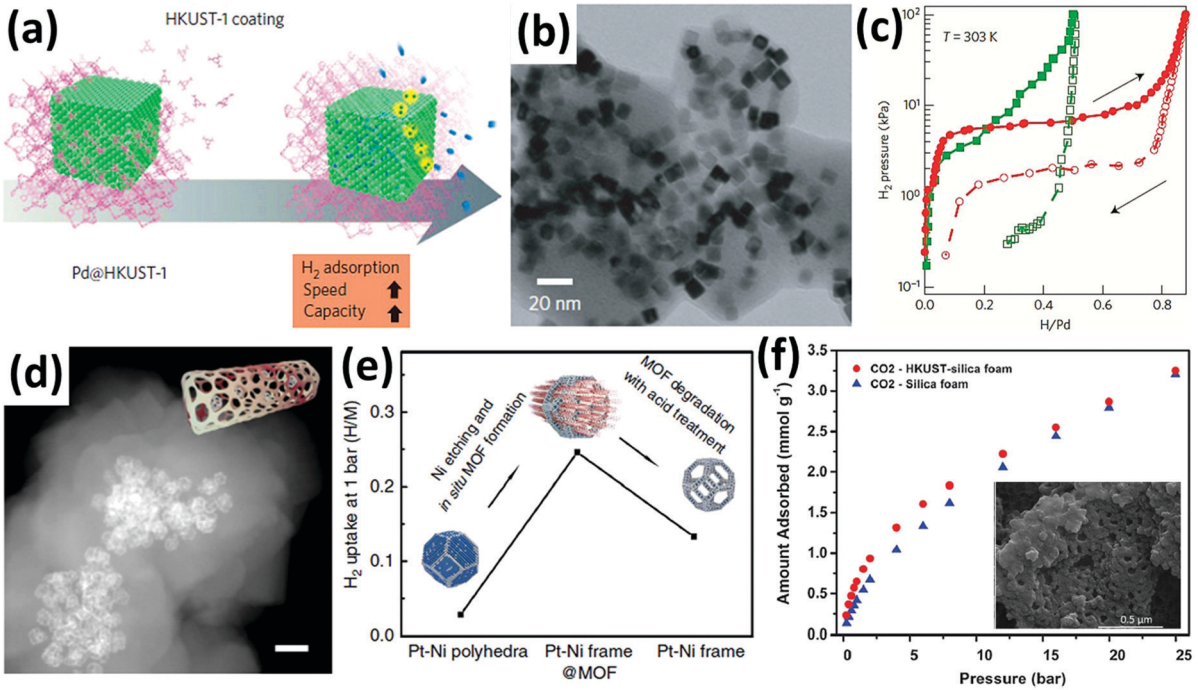

Fig. 16 (a) Schematic of the Pd nanocubes@HKUST-1 used for hydrogen storage with improved speed and capacity. (b) TEM image of Pd@HKUST-1. (c) PC isotherms of Pd nanocubes (green) and Pd@HKUST-1 (red) at 303 K. (d) HAADF-STEM image and ideal model of Pt–Ni frame@MOF. Scale bar: 50 nm. (e) Comparison of the H_2 uptake performance of Pt–Ni polyhedra, Pt–Ni frame and Pt–Ni frame@MOF at 273 K and 1 bar. (f) High pressure CO_2 isotherms of silica foam and HKUST-1 grown on silica foam using a LBL method. The inset of (f) is the SEM image of the HKUST-1 MOF grown on silica foam. (a–c) Reproduced with permission from ref. 40. Copyright 2014, Nature Publishing Group. (d and e) Reproduced with permission from ref. 275. Copyright 2015, Nature Publishing Group. (f) Reproduced with permission from ref. 276. Copyright 2012, Royal Society of Chemistry.

hydride (β-phase). For Pd nanocubes, the coexistence of α- and β-phases disappeared over a wide pressure region, whereas the coexistence in Pd@HKUST-1was observed in a narrow pressure region. After the H_2 concentration was returned to 0 kPa, the two phases coexisted for bare Pd nanocubes, while the Pd phase for Pd@HKUST-1 was back to its initial state. These phenomena suggested faster hydrogen absorption/desorption response and higher reversibility of Pd@HKUST-1 compared with bare Pd nanocubes. Therefore, this enhanced reactivity from MOF coatings can be applied to other core–shell metal@MOF systems for potential applications.

Similarly, to further improve the hydrogen adsorption and storage performance of as-prepared metal nanocrystals, Li *et al.* developed a facile and efficient strategy to synthesize unique bimetallic platinum–nickel frames confined in a functionalized metal–organic framework through the *in situ* etching of platinum–nickel alloys and a subsequent coordination reaction process.[275] The monodispersed Pt–Ni polyhedra with an average size of around 20 nm were used as starting precursors. During the solvothermal process, the solid Pt–Ni polyhedra became a hollow Pt–Ni frame because of the oxidative etching from Ni^0 to Ni^{2+} and the Kirkendall effect. Meanwhile, the released Ni^{2+} coordinated with the near-neighbour 2,5-dioxidoterephthalate (dobdc) to form Ni-MOF-74 (Ni_2dobdc) *in situ* on the Pt–Ni frame. As shown in Fig. 16d, the HAADF-STEM image shows the encapsulated hollow Pt–Ni frame with the interconnecting edges in space and outer good-contacted MOF coatings. Furthermore, H_2 adsorption isotherms at 273 K were performed to study the H_2 adsorption properties of Pt–Ni polyhedra, Pt–Ni frame and Pt–Ni frame@MOFs (Fig. 16e). The Pt–Ni frame@MOF composite exhibited a much larger number of hydrogen atoms absorbed on each metallic atom (0.25 H per metal atom) than bare Pt–Ni polyhedra (0.03 H per metal atom). Furthermore, after the removal of MOF coatings through acid treatment, a 46% degradation of H_2 storage was observed for the Pt–Ni frame. Therefore, the superior H_2 storage performance of the Pt–Ni frame@MOFs was mainly attributed to the as-grown MOF coatings, which not only acted as a 'breath shell' to improve hydrogen enrichment but also activated the confined platinum–nickel surface.

Besides the hydrogen adsorption/storage application, Shekhah *et al.* developed a general layer-by-layer method to achieve highly crystalline homogeneous MOF (*e.g.* HKUST-1 and ZIF-8) coatings grown on a mesoporous silica foam substrate, and demonstrated its enhanced CO_2 adsorption/storage performance.[276] During the layer-by-layer synthesis process of HKUST-1 coatings, the as-prepared mesoporous silica foam was immersed in two diluted ethanolic solutions of copper acetate pentahydrate and 1,3,5-benzenetricarboxylic acid, respectively. Compared with the traditional solution method, this layer-by-layer method directed the growth of uniform MOF thin films on confined surfaces without isolated microcrystals (inset of Fig. 16f). The thickness of HKUST-1 coatings can be controlled by modulating the substrate immersion time and reactant concentrations. As a proof-of-concept application, the HKUST-1-coated silica foam

showed a steeper CO_2 adsorption isotherm and enhanced CO_2 uptake compared with bare silica foam at 298 K and relatively high pressure (Fig. 16f). The enhanced CO_2 adsorption performance was attributed to the presence of unsaturated metal sites in HKUST-1, thus providing enhanced interactions with target CO_2 molecules.

In brief, the above-mentioned research into gas adsorption and storage in these composites highlights the advantages of both metal nanomaterials and functional MOFs. Therefore, to make best use of their synergistic merits, developing novel and efficient synthesis strategies for well-defined core–shell metal@MOF composites is highly desired. On the other hand, a better understanding of these systems will provide in-depth insights into the rational design of novel metal@MOF composites for high-performance gas adsorption and storage.

4.6 Photocatalysis

In chemistry, photocatalysis is the acceleration of a photoreaction in the presence of a catalyst, including light harvest for the formation of electrons and holes, and the catalytic reactions driven by the separated electrons.[277] In general, the catalytic efficiencies for specific reactions under light irradiation are highly dependent on photocatalysts. Because of their unique properties, MOFs used in photocatalysts show great promise for potential solar-to-chemical energy conversion reactions, including water splitting, CO_2 reduction and organic photosynthesis.[278–288] On the one hand, abundant and tunable catalytically active metal sites and/or functional organic linkers at the molecular level endow target MOFs with tailorable physical and chemical functions. On the other hand, the large surface area, unique micropores/mesopores and interconnected channels provide an ideal host for photosensitizers and catalytic moieties. Therefore, due to different characteristics and functions, MOFs can be respectively used as photocatalysts, co-catalysts, and hosts in the photocatalytic systems. In detail, when MOFs are directly used as photocatalysts, their organic bridging ligands can absorb light to produce photogenerated charge carriers under light irradiation for subsequent photoredox reactions. In terms of MOF co-catalysts, other photoharvesting components (for example, dyes and semiconductors) under light irradiation stimulate the formation of electrons and holes, and MOFs efficiently promote both charge separation and catalytic reactions. With regard to MOF hosts, inactive MOFs are used to anchor active and catalytic moieties for light-induced reactions. For example, Silva *et al.* demonstrated water-stable UiO-66 and NH_2-UiO-66 with photocatalytic activity for hydrogen generation under UV irradiation.[289] However, the catalytic hydrogen generation efficiencies of the two MOFs were still not satisfactory. Because of the boosting catalytic effect of Pt nanoparticles for hydrogen formation, the successful deposition of Pt nanoparticles on the surface of UiO-66 and NH_2-UiO-66 as a co-catalyst displayed a remarkably enhanced H_2 production. In addition, for MOF co-catalysts and hosts, the successful introduction of other active components into them to form well-defined and good-contacted composites plays an important role in their photocatalytic performance. Table 5 shows some typical examples of MOF coatings on functional core materials for photocatalysis.[75,290–301]

To address low efficiency in exciton generation, intrinsic inactivity, and the photocatalytic instability of most MOFs under light excitation, one efficient strategy is to combine high surface area and catalytic reactions from MOF co-catalysts with excellent exciton generation from photosensitizers, providing synergistic effects for high-performance photocatalytic reactions.[302] For example, Kataoka *et al.* demonstrated porous Ru-MOFs, $[Ru_2(p\text{-}BDC)_2]_n$, with excellent catalytic hydrogen production activity by the introduction of the $Ru(bpy)_3^{2+}$ (bpy = 2,2′-bipyridine) photosensitizer and the MV^{2+} (*N*,*N*′-dimethyl-4,4′-bipyridinium) electron relay into their open frameworks.[290] After visible light irradiation for 4 h, the turnover numbers based on Ru-MOFs and $Ru(bpy)_3^{3+}$ were 8.16 and 81.6, respectively. The whole photocatalytic process for H_2 evolution involves the excited state of $Ru(bpy)_3^{2+}$ under light

Table 5 A summary of MOF coatings on functional core materials for photocatalysis

MOF species	Functional core materials	Synthesis strategies	Roles of MOF coatings	Irradiation	Photocatalytic reactions	Products	References
$[Ru(p\text{-}BDC)_2]_n$	$Ru(bpy)_3^{2+}$	Template-implantation method	Co-catalysts	Visible light	Water splitting	H_2	290
UiO-66-[FeFe](dcbdt)$(CO)_6$	$Ru(bpy)_3^{2+}$	Template-implantation method	Co-catalysts	Monochromatic light (470 nm)	Water splitting	H_2	291
Co-ZIF-9	$Ru(bpy)_3^{2+}$	Template-implantation method	Co-catalysts	Monochromatic light (420 nm)	CO_2 and water reduction	CO, H_2	292
ZIF-8	Zn_2GeO_4	Liquid–liquid method	Co-catalysts	Visible light	CO_2 reduction	CH_3OH	293
Fe-MIL-100	Pd	Template-implantation method	Photocatalysts	Visible light	*N*-Alkylation reaction of amines	*N*-Alkyl amines	295
UiO-66(NH_2)	Au	Liquid–liquid method	Photocatalysts	Visible light	Oxidation of alcohols	Ketone	296
MIL-53	$NaYF_4$: Yb,Tm	Liquid–liquid method	Photocatalysts	Ultraviolet/visible/near-infrared light	Photodegradation	CO_2, H_2O	75
ZIF-67	$CsPbBr_3$	Liquid–liquid method	Photocatalysts	Visible light	CO_2 reduction	CO, CH_4	297
Al-TCPP	Pt atoms	Template-implantation method	Photocatalysts	Visible light	Photocatalytic H_2 production	H_2	298
UiO-66(Zr)	Pt	Template-implantation method	Photocatalysts	Visible light	Photocatalytic H_2 production	H_2	299
MIL-100(Fe)	Fe_3O_4	Liquid–liquid method	Photocatalysts	Visible light	Photodegradation	CO_2, H_2O	300
ZIF-8	CdS	Liquid–liquid method	Photocatalysts	Visible light	Photocatalytic H_2 production	H_2	294

irradiation, the electron relay for MV^{2+}, catalyzed by Ru-MOFs, and the reduction of $Ru(bpy)_3^{3+}$ by EDTA-2Na. Similarly, Pullen *et al.* reported a molecular proton reduction catalyst [FeFe]-(dcbdt)$(CO)_6$ (dcbdt = 1,4-dicarboxylbenzene-2,3-dithiolate) incorporated into robust Zr-based MOFs (UiO-66), displaying enhanced photochemical hydrogen production in the coexistence of the $Ru(bpy)_3^{2+}$ photosensitizer and the ascorbate electron donor.[291] The successful incorporation of the [FeFe]-(dcbdt)$(CO)_6$ complex mainly resulted in good stability of UiO-66 and protected reduced species from nonproductive charge recombination under photocatalysis conditions.

Besides the above-mentioned complex photosensitizers, functional nanostructured inorganic materials can also be used as potential photoharvesting candidates for photocatalysis because of their unique features, such as relatively high extinction coefficient, wide/controlled light absorption range, long charge diffusion length, and long carrier lifetime. Recently, Kong *et al.* designed and constructed a unique ZIF-coated halide perovskite quantum dot core–shell structure ($CsPbBr_3$@ZIF), exhibiting remarkably enhanced photocatalytic CO_2 reduction performance under visible light irradiation (Fig. 17a).[297] The $CsPbBr_3$@ZIF hybrids were synthesized by a typical liquid–liquid synthesis method. The as-prepared $CsPbBr_3$ quantum dots with an average diameter of ~5 nm were dispersed into the precursor solution and then directed the oriented growth of MOF shells on their surfaces. As shown in Fig. 17b, the TEM image shows that well-dispersed $CsPbBr_3$ quantum dots were confined completely in ZIF-8 crystals. The HRTEM image further shows $CsPbBr_3$ quantum dots with clear lattice spacings, confirming high crystallinity (inset of Fig. 17b). The photocatalytic CO_2 reduction performances of ZIF-8, ZIF-67, $CsPbBr_3$, $CsPbBr_3$@ZIF-8 and $CsPbBr_3$@ZIF-67 samples were measured for comparison (Fig. 17c). All samples displayed a

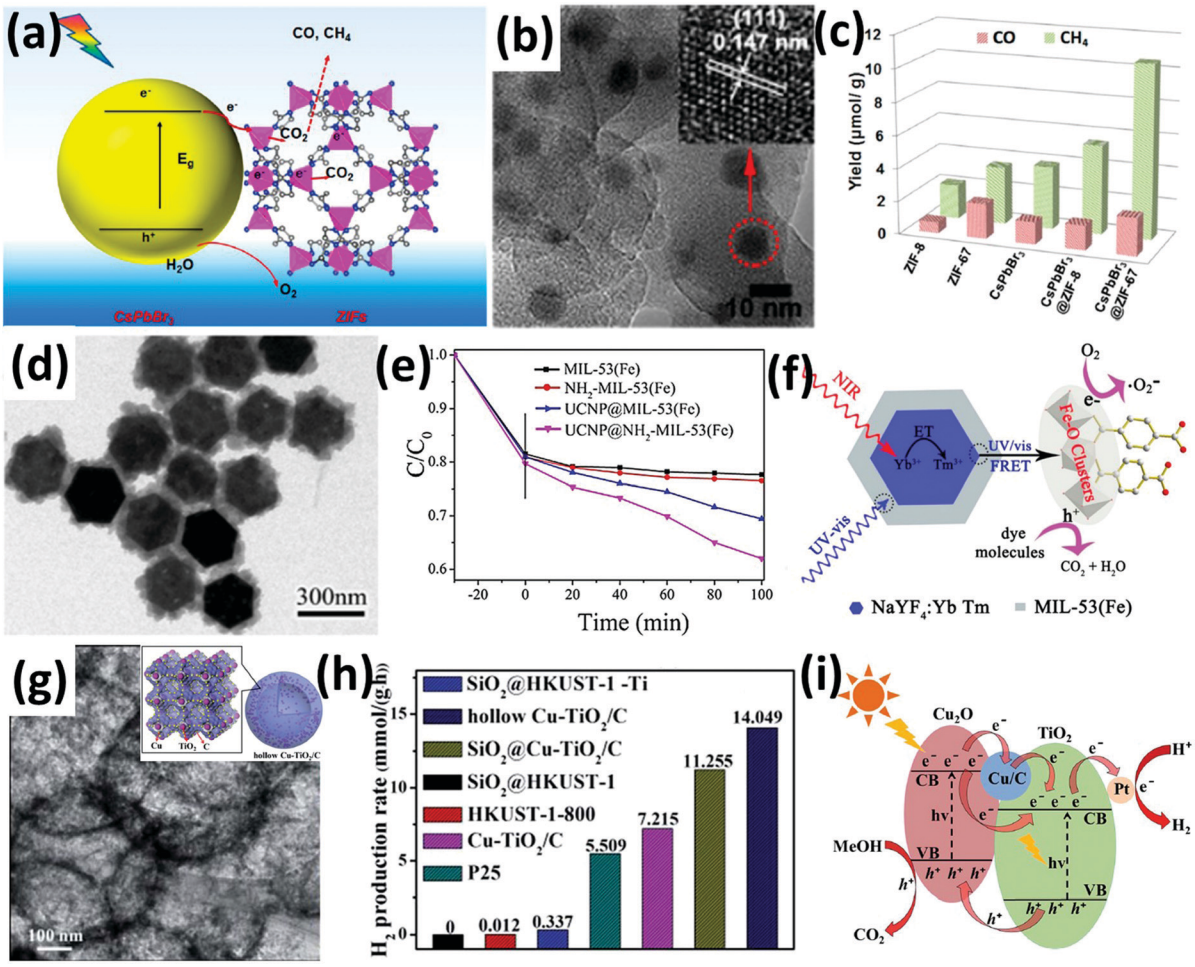

Fig. 17 (a) Schematic illustration of the CO_2 photoreduction process of $CsPbBr_3$/ZIFs. (b) TEM image of $CsPbBr_3$@ZIF-8. The inset of (b) is the high-resolution image of a single $CsPbBr_3$ QD marked with a red circle. (c) Product yield after 3 h of photocatalytic CO_2 reduction reaction under AM 1.5G and 150 mW cm^{-2}. (d) TEM image of upconversion nanoparticles coated with MIL-53(Fe). (e) A comparison of samples' activities under NIR light. (f) Schematic illustration of the photocatalytic mechanism of the prepared UCNP@MIL-53(Fe) NPs. (g) TEM image of hollow Cu–TiO_2/C nanospheres. (h) Photocatalytic H_2 production rate of HKUST-1-800, P25, SiO_2@HKUST-1, SiO_2@HKUST-1-Ti, SiO_2@Cu–TiO_2/C, solid Cu–TiO_2/C and hollow Cu–TiO_2/C nanospheres under simulated sunlight irradiation. (i) Photocatalytic mechanism of hollow Cu–TiO_2/C nanospheres under simulated sunlight irradiation. (a–c) Reproduced with permission from ref. 297. Copyright 2018, American Chemical Society. (d–f) Reproduced with permission from ref. 75. Copyright 2017, American Chemical Society. (g–i) Reproduced with permission from ref. 304. Copyright 2018, Royal Society of Chemistry.

relatively high yield of CH_4 and a low CO yield, which were attributed to the existence of sufficient protons from water vapor. The electron consumption rate ($R_{electron}$) was used to calculate the number of consumed electrons for each product molecule and evaluate the photocatalytic efficiency of the samples. By contrast, the $R_{electron}$ values of $CsPbBr_3$@ZIF-8 and $CsPbBr_3$@ZIF-67 were 15.498 and 29.630 μmol g^{-1} h^{-1}, respectively, which were accordingly 1.39 and 2.66 times that of $CsPbBr_3$ (11.14 μmol g^{-1} h^{-1}). This phenomenon confirmed the remarkable enhancement of ZIF coatings, specifically ZIF-67 coatings for $CsPbBr_3$. The superior photocatalytic reaction of the ZIF-67 coating was attributed to its catalytically active Co centers, thus greatly enhancing its activation and reduction reaction of CO_2. After 6 cycles, no obvious $R_{electron}$ decay of $CsPbBr_3$@ZIF-67 was observed, indicating its excellent catalytic stability. More importantly, the photocatalytic reaction mechanism/process of $CsPbBr_3$@ZIFs was proposed. First, the excited $CsPbBr_3$ generated electron–hole pairs under visible light irradiation, which were quickly separated at the $CsPbBr_3$ and ZIFs interfaces. Then, the transferred electrons from $CsPbBr_3$ and photogenerated electrons on ZIFs accelerated the CO_2 reduction reaction together. In addition, the holes were quenched by H_2O to generate O_2.

In addition to photocatalytic H_2 and CO_2 generation, the photocatalytic degradation of dye pollutions is also an important application. For instance, Li *et al.* reported upconversion nanoparticles (UCNPs) confined in MOFs (denoted as UCNP@MOFs) to build a NIR-responsive composite photocatalyst for efficient degradation of dye pollutions.[75] During the solution synthesis process, the introduction of PVP induced Fe^{3+} to be enriched on the UCNP surface *via* its strong coordination capability of pyrrolyl groups, and then the fixed Fe^{3+} coordinated with terephthalic acid by heterogeneous nucleation on the UCNP surface, thereby forming MIL-53(Fe) shells and avoiding the homogeneous nucleation in the solution. Similarly, by simply replacing the terephthalic acid with 2-aminoterephthalic acid, the core–shell $NaYF_4$:Yb,Tm@NH_2-MIL-53(Fe) nanoparticles can be easily obtained. TEM images showed obviously coarse and concave MOF coatings, confirming their core–shell structures (Fig. 17d). Furthermore, under NIR light, UCNP@MIL-53(Fe) and UCNP@NH_2-MIL-53(Fe) displayed an obvious photocatalytic degradation property in rhodamine B solution, while the pure MIL-53(Fe) and NH_2-MIL-53(Fe) showed no catalytic activity (Fig. 17e). In addition, before light irradiation, all the four samples exhibited obvious adsorption to the dye molecules because of the high surface area of MOFs. To further identify the synergistic effect of the UCNP@MIL-53(Fe) sample, a photocatalytic mechanism was proposed as shown in Fig. 17f. Under NIR light irradiation, the UCNPs absorbed the NIR photons, and then the excited electrons in Tm^{3+} were transferred to the surrounding MOF shell. Subsequently, the activated Fe(III)–O clusters of the MIL-53(Fe) shell produced photogenerated negative electrons and positive holes. Furthermore, the photogenerated electrons reacted with the surrounding O_2 molecules to form radicals, which together with holes acted as oxidants for dye degradation. In addition, the MOF shells can also be activated by UV and visible light. Thus, the well-designed core–shell UCNP@MOFs showed great potential for enhanced photocatalytic efficiency under the full solar spectrum.

MOF coatings are also good precursors for the synthesis of carbon-based composites or metal oxides with well-designed shapes and morphologies for photocatalysis.[303] Recently, Chen *et al.* designed and constructed hollow carbon nanospheres with Cu–TiO_2 nanocrystals (Cu–TiO_2/C) from a Ti-based precursor encapsulated MOF coating *via* a facile method, exhibiting high photocatalytic H_2 production and good recyclability under sunlight irradiation.[304] The formation of Cu–TiO_2/C hollow nanospheres involves a four-step process, including a liquid-phase epitaxial layer-by-layer synthesis approach for uniform MOF shells on SiO_2 nanospheres, the loading of a Ti-based precursor (titanium isopropylate) into MOF shells, controlled pyrolysis, and template removal. The TEM image shows the hollow structure of the resulting Cu–TiO_2/C product (Fig. 17g). Furthermore, photocatalytic H_2 production of different samples deposited with Pt nanoparticles as co-catalysts was evaluated under simulated sunlight irradiation (Fig. 17h). HKUST-1-800, SiO_2@HKUST-1 and SiO_2@-HKUST-1-Ti showed no photocatalytic H_2 evolution, while the photocatalytic H_2 evolution rates of P25, solid Cu–TiO_2/C, SiO_2@Cu–TiO_2/C, and hollow Cu–TiO_2/C nanospheres were 5.509, 7.215, 11.255 and 14.049 mmol g^{-1} h^{-1}, respectively. The superior H_2 evolution performance of hollow Cu–TiO_2/C nanospheres is mainly attributed to their hollow structure, uniform nanosize and rich active sites. Importantly, the mechanism of photocatalytic H_2 evolution of hollow Cu–TiO_2/C nanospheres with abundant p–n heterojunctions between TiO_2 and Cu_2O was proposed as shown in Fig. 17i. Under simulated sunlight irradiation, the photo-generated electrons in the conduction band of Cu_2O will enter the conduction band of TiO_2, while the photo-induced holes will conversely transfer from the valence band of TiO_2 to the valence band of Cu_2O. The carbon and Cu accelerated the mobility of electronic charge. This phenomenon is beneficial for the separation of electron–hole pairs. Furthermore, the photogenerated electrons from TiO_2 to Pt result in H_2 production. Meanwhile, the holes in the valence bond of Cu_2O convert the sacrificial methanol into carbonyl compounds. In brief, this work demonstrates that hollow hybrid carbon nanospheres from MOF shells show great potential in various photocatalytic reactions.

4.7 Sensors

Due to their tunable structures and functionalized properties, MOFs also show great potential in chemical sensors, which are superior to other conventional chemo-sensory materials.[305,306] By modifying organic ligands or metal ions/clusters, functionalized MOFs can be easily modulated for specific sensors. For example, the selected lanthanide metal ions in MOFs were usually used to construct luminescent MOFs for optical sensors. To achieve highly efficient and specific signal recognition, the incorporation of functional nanomaterials into MOFs was also demonstrated to be an efficient approach, endowing the composites with synergistic and multiple properties for diverse MOF-based sensors, including optical, electrochemical, mechanical, and photoelectrochemical sensors.[307–311]

To combine the high sensitivity of nanostructured metal oxides and the high selectivity and catalytic activity of MOFs, for the first time, Yao *et al.* designed and constructed a uniform hydrophobic and catalytic ZIF–CoZn thin coating on a ZnO nanowire array for a chemiresistor gas sensor (Fig. 18a).[312] During the solution synthesis process, the as-prepared ZnO nanowires with 50–100 nm diameter were employed as self-templates to induce the heterogeneous nucleation and growth of ZIF–CoZn thin film on their surfaces to form well-defined core–shell structures. The thickness of the target ZIF–CoZn thin film can be easily controlled by modulating different reaction parameters. After coating, the obtained ZnO@5 nm ZIF–CoZn nanowires with a length of 2–4 μm still remained vertical on the substrate (Fig. 18b). Furthermore, the gas sensing experiments were performed to evaluate the performance of the ZnO@ZIF–CoZn sensor *via* monitoring the resistance of the device in a sealed quartz chamber with different acetone concentrations and/or different relative humidity. From the dynamic responses of the ZnO@ZIF–CoZn sensor in Fig. 18c, the relative current increased along with the increase in acetone concentration (0.25–100 ppm), while the current in the different humidity range from 0% to 90% almost remained stable. This phenomenon indicated good response recovery to the acetone concentrations and high acetone selectivity. In addition, the ZnO@5 nm ZIF–CoZn sensor had the lowest detection limit (0.0019 ppm), which was improved by about two orders of magnitude compared with the bare ZnO nanowire array sensor. The superior sensing property was attributed to the synergistic effect between ZnO and ZIF–CoZn. The core ZnO nanowires acted as active materials for the oxidation reaction between adsorbed oxygen species and interfacial analytes, thereby resulting in the variation of ZnO conductivity. On the other hand, the ZIF–CoZn shell was employed as a molecular sieve to selectively allow the target analytes to pass through, endowing the core–shell composite with high selectivity for gas sensors. Besides, the Co^{2+} in the ZIF–CoZn shell possessed good catalytic property to enhance the response and recovery behavior of the integrated sensor. Therefore, this work on core–shell composites opens up a good avenue to achieve high-performance gas sensors.

Besides the electrochemical sensors, MOF-based optical sensors also have attracted much interest. To improve the surface-enhanced Raman scattering (SERS) sensitivity for analyte detection, Sugikawa *et al.* synthesized gold nanorods confined in MOF-5 nanocrystals (AuNR@MOF-5) by a facile solution method (Fig. 18d).[313] During the SERS process, the Raman scattering signals can be improved a millionfold or more when the analyte was adsorbed on gold nanorods. The resulting MOF-5 shell not only avoided the aggregation of golden nanorods, but also acted as a molecular sieve to selectively allow the small molecules to pass through, improving the activity and selectivity of golden nanorods. As a SERS sensor, the obtained AuNR@MOF-5 nanocrystals showed excellent SERS activity, stability and reproducibility for the detection of small pyridine and its derivatives, while large polymeric pyridine derivatives showed no SERS activity. Similarly, Kreno *et al.* demonstrated the enhanced localized surface plasmon resonance gas sensing property of the Ag nanoparticle sensor *via* a well-defined HKUST-1 coating.[314]

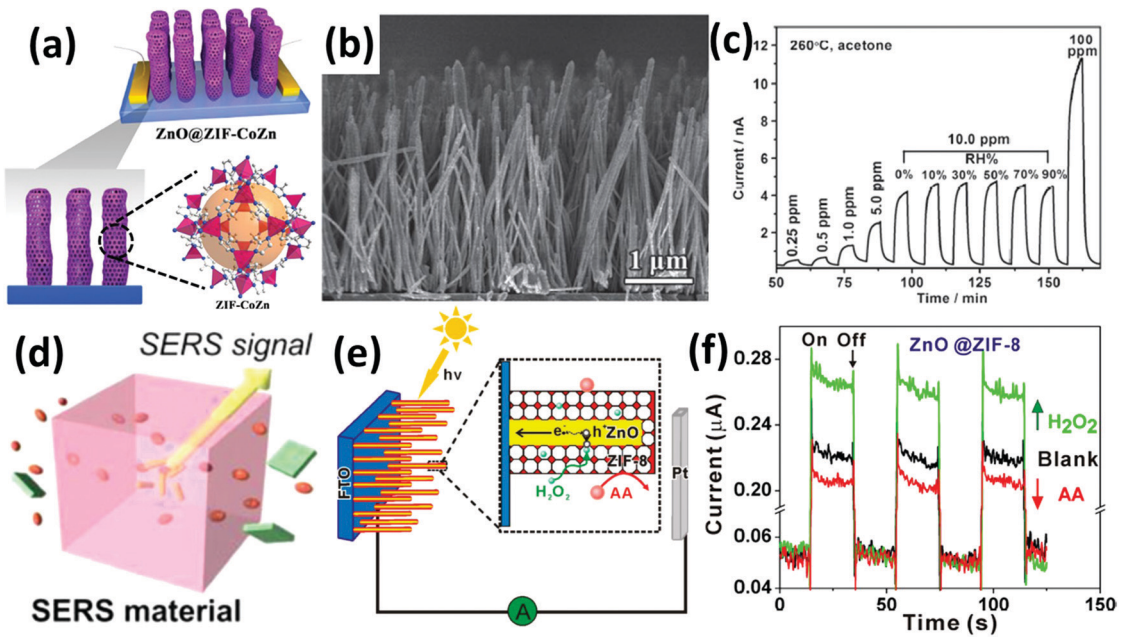

Fig. 18 (a) Schematic illustration of the core–shell ZnO@ZIF–CoZn nanowire arrays. (b) Cross-sectional SEM image of ZnO@5 nm ZIF–CoZn nanowire arrays. (c) Response-recovery curves of ZnO@5 nm ZIF–CoZn to acetone with different concentrations in dry air and to 10 ppm acetone with different relative humidity. (d) Schematic illustration of AuNR@MOF-5 nanocrystals for SERS sensors. (e) Schematic diagram of the PEC sensor with selectivity to H_2O_2. (f) Photocurrent responses of the ZnO@ZIF-8 nanorod array in the presence of H_2O_2 (0.1 mM) and AA (0.1 mM). (a–c) Reproduced with permission from ref. 312. Copyright 2016, Wiley-VCH. (d) Reproduced with permission from ref. 313. Copyright 2013, American Chemical Society. (e and f) Reproduced with permission from ref. 99. Copyright 2013, American Chemical Society.

To utilize the photoelectrochemical response of inorganic semiconductors, Zhan *et al.* designed and constructed core–shell ZnO@ZIF-8 nanorod arrays on a fluorine-doped tin oxide (FTO) doped glass *via* a simple self-template solid–liquid synthesis strategy and demonstrated their great potential in photoelectrochemical sensors.[99] During the synthesis process, the ZnO nanorod templates provided Zn^{2+} ions, thereby forming ZIF-8 thin coatings by a coordination reaction with organic ligands. Furthermore, as illustrated in Fig. 18e, the photoelectrochemical test of the resulting ZnO@ZIF-8 sample was carried out for photoelectrochemical sensors. Under light irradiation, the partial generated electrons and holes in ZnO nanorods can migrate to their surface and thereby react with the surrounding redox species in solution. Two reductive species, H_2O_2 and ascorbic acid (AA), were chosen as examples for comparison. The pore aperture of ZIF-8 is larger than that of H_2O_2 but smaller than that of AA. Therefore, only H_2O_2 can pass through the ZIF shell to reach the ZnO surface. The reaction equation is as follows: $H_2O_2 + 2h^+ \rightarrow 2H^+ + O_2$. As shown in Fig. 18f, the addition of H_2O_2 obviously enhanced the photocurrent response of the ZnO@ZIF-8 sample, while the addition of AA reduced its photocurrent response. This difference was because of the high selectivity of the ZIF-8 shell between H_2O_2 and AA. Therefore, the rational design of novel semiconductor@MOF core–shell heterostructures was demonstrated to be an efficient approach for high-selectivity photoelectrochemical sensors.

In brief, due to their synergistic effects, the well-defined composites by integrating MOF coatings with other functional core materials show great advantages than pure MOFs. Generally, the functions of MOF coatings include good dispersants for cores and high selectivity for target analytes. The delicate MOF coatings can be easily controlled for different target analytes, simultaneously improving the sensor activity and selectivity. For specific sensors, the choice of appropriate MOF species and functional materials and the design of good-contacted core–shell structures between them simultaneously play an important role in the integrated sensor performance.

4.8 Hydrogenation

Catalytic hydrogenation generally refers to a chemical reaction between hydrogen and unsaturated substrates on catalysts, which shows great potential in industrial processes.[315,316] Up to now, metal nanoparticles, especially noble metal nanoparticles, have attracted much attention as catalysts for molecular hydrogenation in ambient conditions because of their high surface area and high intrinsic activity. To achieve the high-efficiency hydrogenation performance of metal nanoparticles, unique MOF coatings on metal nanoparticles can endow the core–shell nanocomposites with specific merits as follows: (1) MOF coatings as a support and protection to prevent the aggregation of confined metal nanoparticles and stabilize their properties during the catalytic hydrogenation process; (2) MOF coatings as a molecular sieve to offer high selectivity for catalytic hydrogenation because of their tunable porosity to bridge the gap between zeolites and mesoporous materials; (3) MOF coatings with a synergistic role together with metal nanoparticles to improve the integrated catalytic hydrogenation owing to their unsaturated metal ions/clusters and functional organic linkers.[317] As a proof-of-concept application, Table 6 summarizes unique MOF coatings on functional metal nanoparticles as heterogeneous catalysts for the hydrogenation of various unsaturated molecular substrates (*e.g.* α-ketoesters, phenol, acetylene, 1-octene, 1-hexene, 1-chloro-2-nitrobenzene, styrene, nitrobenzene and benzaldehyde).[39,60,61,85,275,318–324] Furthermore, some typical examples and their structure–property relationships are highlighted and discussed.

Lu *et al.* reported a facile, general and controlled liquid–liquid synthesis strategy to encapsulate various PVP-capped nanomaterials (*e.g.* Pt, Fe_3O_4, $NaYF_4$, and CdTe) within ZIF-8.[39] As shown in Fig. 19a, 3.3 nm Pt nanoparticles were uniformly distributed in ZIF-8 crystals. ZIF-8 is a microporous material with uniform large cavities (11.6 Å) and small apertures (3.4 Å). When used in the liquid-phase hydrogenation of *n*-hexene *versus* *cis*-cyclooctene, the obtained Pt/PVP/ZIF-8 composite showed obvious catalytic hydrogenation of small *n*-hexene molecules and no hydrogenation property for large cyclooctene molecules (Fig. 19b). In contrast, pure ZIF-8 crystals displayed no catalytic activity for these two molecules, while pure Pt nanoparticles on CNT (Pt/CNT) exhibited relatively high hydrogenation without any selectivity. Therefore, the superior hydrogenation properties of the Pt/PVP/ZIF-8 composite were mainly attributed to the synergistic effect between the high catalytic activity of Pt nanoparticles and high selectivity from the molecular sieving capability of ZIF-8 coatings.

Table 6 A summary of MOF coatings on functional core materials for hydrogenation

MOF species	Pore size (Å)	Metal nanoparticles	Nanoparticle weight (wt%)	Synthesis strategies	Hydrogenation species	Conversion (%)	Ref.
MIL-101(Cr)	12	Pt	5	Template impregnation method	α-Ketoesters	96.8	318
MIL-101(Cr)	12	Pd	5	Template impregnation method	Phenol	98	319
MIL-101(Cr)	12	Pd	1	Template impregnation method	Acetylene	80–100	60
MIL-101(Cr)	12	Pt	5	Template impregnation method	1-Octene	100	61
ZIF-8	3.4	Pt	0.23–0.74	Liquid–liquid method	1-Hexene	95	320
ZIF-8	3.4	Pt	2	Liquid–liquid method	*n*-Hexene	100	321
ZIF-8	3.4	Pd	2	Template impregnation method	1-Hexene	100	39
ZIF-8	3.4	Pd	—	Liquid–liquid method	Ethylene, cyclohexene	100	322
MOF-5	7.8	Pd	1	Template impregnation method	Styrene	97	323
MOF-5	7.8	Ru	0.98	Template impregnation method	Cyclohexene and benzene	99	324
MOF-74	8.6	Pt/Ni	1.6	Solid–liquid method	1-Chloro-2-nitrobenzene, styrene, nitrobenzene and benzaldehyde	99	275
ZIF-8	3.4	Pd–mSiO_2	4.61	Liquid–liquid method	Styrene	71.1	85

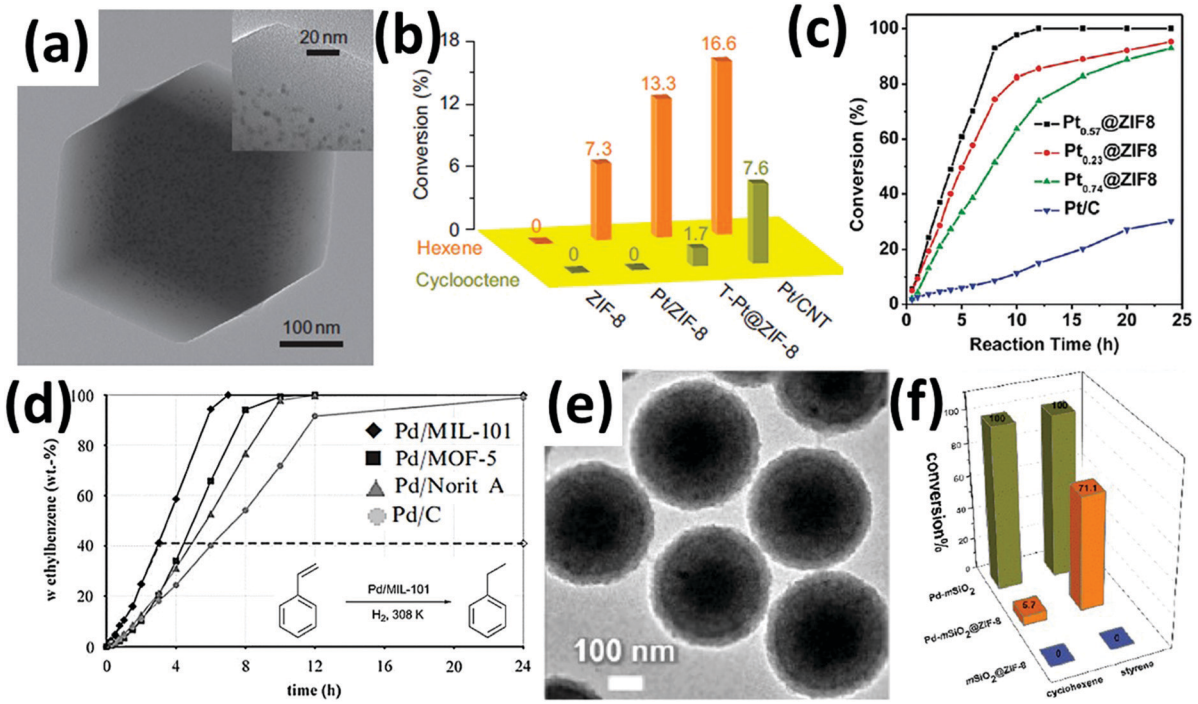

Fig. 19 (a) TEM image of the 3.3 nm Pt nanoparticles/ZIF-8 composite. The inset of (a) is a magnified TEM image. (b) Size-selective hydrogenation of *n*-hexene and *cis*-cyclooctene for Pt/ZIF-8 composite (3.3 nm Pt nanoparticles, Pt content 2%), pure ZIF-8, T-Pt@ZIF-8 composite (Pt content 2%) and Pt/CNT (Pt content 5%). (c) Kinetic curves of hydrogenation of 1-hexene over Pt_n@ZIF-8 (0.23, 0.57 and 0.73 stand for Pt content in ZIF-8) and Pt/C. (d) Hydrogenation of styrene of Pd/MIL-101, Pd/MOF-5, Pd/Norit A and Pd/C catalysts. (e) TEM image of monodisperse Pd–$mSiO_2$@ZIF-8 core–shell microspheres. (f) Catalytic performance of Pd–$mSiO_2$ spheres before and after ZIF-8 coating for liquid-phase hydrogenation of styrene and cyclohexene with pure $mSiO_2$@ZIF-8 as controls for comparison. (a and b) Reproduced with permission from ref. 39. Copyright 2012, Nature Publishing Group. (c) Reproduced with permission from ref. 320. Copyright 2013, Royal Society of Chemistry. (d) Reproduced with permission from ref. 60. Copyright 2008, Royal Society of Chemistry. (e and f) Reproduced with permission from ref. 85. Copyright 2015, American Chemical Society.

Similarly, to eliminate the negative effect of PVP surfactants, Wang *et al.* realized direct assembly of ZIF-8 coatings on as-prepared Pt nanoparticles to obtain a core–shell Pt@ZIF-8 composite with controlled weight percentages of Pt.[320] The combination of active Pt nanoparticles and the molecular sieving capability of ZIF-8 coatings endowed the Pt@ZIF-8 composite with size-selective and catalytic hydrogenation properties. As shown in Fig. 19c, the obtained Pt@ZIF-8 composites with different Pt weight percentages displayed obviously enhanced catalytic hydrogenation activity from 1-hexene to 1-hexane than commercial Pt/C. This phenomenon resulted from the highly dispersed ultrasmall Pt nanoparticles and the large surface area of ZIFs, which were beneficial for high catalytic activity and strong H_2 adsorption. In addition, the Pt@ZIF-8 composites exhibited no catalytic hydrogenation of *cis*-cyclooctene. This great difference was attributed to their different molecular width. By molecular simulation, the molecular width of 1-hexene and *cis*-cyclooctene was approximately 1.7 and 5.5 Å, respectively. Therefore, the 3.4 Å channels of ZIF coatings hindered large *cis*-cyclooctene from passing through to active Pt surfaces.

Furthermore, Henschel *et al.* synthesized a catalytic composite with palladium nanoparticles supported in MIL-101 crystals (denoted as Pd/MIL-101), and demonstrated its remarkable, synergistic and stable hydrogenation property towards styrene and cyclooctene.[60] As shown in Fig. 19d, the Pd/MIL-101 catalyst exhibited the highest hydrogenation activity with complete conversion from styrene to ethylbenzene after 7 h, compared with Pd/MOF-5 (~80 wt% yield), Pd/Norit A (~60 wt% yield) and Pd/C (less than 50 wt% yield) under the same reaction conditions. The higher activity of Pd/MIL-101 can be attributed to the larger pore size and efficient active sites in MIL-101. Besides, the Pd/MIL-101 catalyst showed remarkably slow deactivation under harsh reaction conditions, which was attributed to the protection of robust MIL-101 coatings.

To realize high-efficiency and high-flux hydrogenation, Xi *et al.* reported a versatile stepwise approach to synthesize monodispersed integrated metal–$mSiO_2$@ZIFs core–shell nanocatalysts (metal nanoparticles contain Pt, Ag, Ru, Pd, and $Pt_{53}Ru_{47}$; $mSiO_2$ represents mesoporous SiO_2).[85] Ultrafine metal nanoparticles with 2–5 nm size were first deposited uniformly onto the channels of mesoporous SiO_2 spheres, and then the formed metal–$mSiO_2$ guided the heterogeneous nucleation and growth of ZIF coatings on their outer surfaces. As shown in Fig. 19e, the clear contrast difference of the target product demonstrated the successful combination of the Pd–$mSiO_2$ core and the ZIF-8 shell. Furthermore, selective hydrogenation of alkenes was measured to investigate the structural superiority of the Pd–$mSiO_2$@ZIF-8 composite. $mSiO_2$@ZIF-8 and Pd–$mSiO_2$ were chosen as control samples for comparison. For the hydrogenation of styrene and cyclohexene, $mSiO_2$@ZIF-8 showed no catalytic activity for

both molecules, while Pd-mSiO_2 displayed high activity without selectivity (Fig. 19f). It indicated that the hydrogenation activity was highly dependent on Pd nanoparticles. The open frameworks in mesoporous SiO_2 were beneficial for the free diffusion of target substrates to Pd nanoparticles. Moreover, the core–shell Pd–mSiO_2@ZIF-8 composite showed high catalytic activity for styrene with 71.1% conversion and low activity for cyclohexene with only 5.7% conversion, indicating its high selectivity. Although styrene and cyclohexene have similar kinetic diameters of about 6.0 Å, their large activity difference was mainly attributed to the π–π stacking interaction between styrene and the aromatic framework of ZIF-8 shells to selectively pass through. In addition, compared with bulk ZIF coatings, the thin and uniform ZIF shell endowed the core–shell composite simultaneously with high conversion efficiency for styrene and high selectivity.

4.9 Drug delivery/cytoprotection

In recent years, MOFs have been considered as promising candidates and hosts for drug delivery/cytoprotection.[325–330] Some distinguished features are discussed as follows. First, by modulating metal ions/clusters and inorganic linkers, the as-prepared functional MOFs possess diverse morphologies, tunable sizes and abundant compositions, thereby endowing them with specific physical/chemical properties. Synthesis chemistry can also be used to obtain well-defined composites integrating MOFs with target drugs/cells towards high-efficiency biological applications. Second, compared with traditional inorganic materials, the ultrahigh surface area and porosity endow MOF carriers with high mass loading especially for small molecule drugs. Third, weak coordination bonds of MOFs realize their easy biodegradation for target drug/cell release. Stimuli-responsive MOFs can be controlled for drug release by different ambient conditions (*e.g.* pH, magnetic field, ions, temperature, light, and pressure). For example, pH-responsive MOFs have been the most widely investigated.[331] Zhu *et al.* reported pH-responsive Zr-based MOF nanoparticles as an efficient carrier for alendronate delivery, and demonstrated its mediated release.[332] In addition, the introduction of functional inorganic materials into MOFs can also endow the well-defined all-in-one composites with more synergistic properties.

Drug delivery in the body using non-toxic nanocarriers plays an important role in disease therapies and body health. To realize synchronous delivery of the dihydroartemisinin (DHA) drug and Fe(III) ions into tumor cells, Wang *et al.* designed and constructed core–shell Fe_3O_4@C@MIL-100(Fe) (FCM) nanoparticles as an efficient host to load hydrophobic DHA for cancer therapy.[333] The core Fe_3O_4@C nanoparticles exhibited magnetic-targeting ability from Fe_3O_4 and two-photon fluorescence imaging (TPFI) ability from small carbon dots of the carbon layer. The resulting FCM could be controlled using an external magnetic field, and simultaneously be minored using TPFI. On the other hand, under acidic conditions, the release of DHA and Fe(III) ions occurred simultaneously from the outer MIL-100(Fe) shell *via* degradation. Subsequently, the reduced Fe ions reacted with DHA along with the generation of reactive oxygen species (ROS), which further led to tumor cell death (Fig. 20a). Compared with the control, DHA and DHA@FCM samples, DHA@FCM with magnetic treatment resulted in the strongest fluorescence intensity in tissue, indicating the highest ROS yield (Fig. 20b). Therefore, the well-designed bio-composites possessed multifunctional properties, showing great potential for drug delivery. Similarly, Bian *et al.* designed and constructed multifunctional Fe_3O_4@polyacrylic acid/Au nanoclusters/ZIF-8 nanoparticles for drug delivery (Fig. 20c).[334] The integrated nanoparticles exhibited high doxorubicin loading capability, tri-modal cancer imaging ability, good biocompatibility as well as pH-responsive and magnet-targeting drug-release.

To enhance the robustness of functional biomacromolecules in biotechnology, Liang *et al.* reported a novel biomimetic mineralization method to encapsulate biomacromolecules (for example, proteins, enzymes and DNA) within MOFs (Fig. 20d).[63] During the mineralization synthesis process, various biomacromolecules can induce MOF formation on their surfaces and control the resultant MOF morphology under physiological conditions. This versatile method was also successfully extended to biomimetically mineralize the growth of a series of MOFs on biomacromolecules, including ZIF-8, HKUST-1, $Eu_2(1,4\text{-BDC})_3(H_2O)_4$, $Tb_2(1,4\text{-BDC})_3(H_2O)_4$ and MIL-88A. In addition, by using a series of biomacromolecules, the morphologies of biomimetically mineralized ZIF-8 crystals were quite different. These observations were highly dependent on unique biomacromolecules due to their different size and molecular structure. Furthermore, taking the ZIF-8/HRP biocomposite as an example, the enhanced protective performance of ZIF-8 coatings on well-studied enzymes (HRP) was measured in comparison with other controls under different conditions (Fig. 20e). In the presence of trypsin, the ZIF-8/HRP biocomposite exhibited remarkable HRP bioactivity with an 88% conversion from pyrogallol to purporogallin, higher than that of non-protected HRP (22%). In addition, in boiling water and boiling DMF conditions, the ZIF-8/HRP biocomposite showed a much higher conversion of $>88\%$ compared with $CaCO_3$/HRP, SiO_2/HRP, and pure HRP samples. To explore the activity of the occluded biomacromolecule after removing the MOF shells, two ZIF-8/DQ-OVA and ZIF-8/trypsin biocomposites were treated in different pH solutions (Fig. 20f). DQ-OVA and trypsin are a fluorogenic protein and a proteolytic enzyme, respectively, which can react and thus release fluorescence signals. In pH 7.4 solution, no fluorescence signals were observed, indicating that the two biomacromolecules were stable within the MOF shells. However, in pH 6 solution, strong fluorescence intensity appeared and was analogous to that of free DQ-OVA and trypsin, which was attributed to the complete release of bioactive trypsin and DQ-OVA from the respective MOF coatings (Fig. 20g). Therefore, MOF coatings show great potential in protecting and delivering functional biomacromolecules for frontier biologic fields.

In addition, to address the inherent fragility of living cells under environmental conditions (*e.g.*, ultraviolet radiation, malnutrition, dehydration, and elevated temperatures), stable and biocompatible MOF coatings have attracted much attention for cytoprotection.[335,336] For example, Liang *et al.* reported a biomimetic mineralization process to fabricate crystalline MOF protective coatings for living cells, which protected them against the damage from external environments and the loss of cell activity (Fig. 20h).[41] During the liquid–liquid synthesis process,

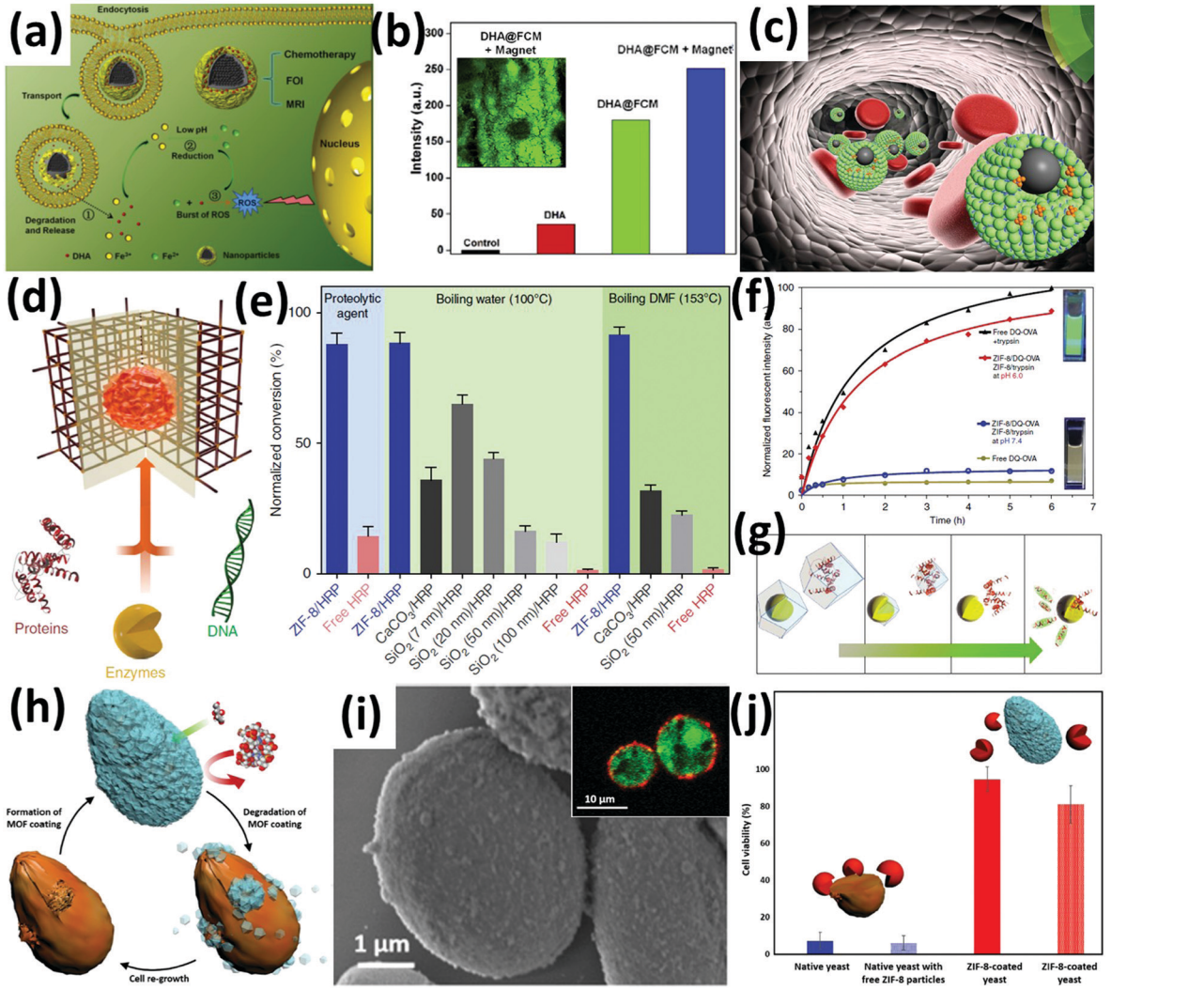

Fig. 20 (a) Schematic illustration of the anticancer mechanism of the DHA delivery system. (b) Fluorescence intensity of the emission spectrum of different treatments in the range of 490–600 nm of different tumor slices under 488 nm laser excitation. The inset of (b) is the ROS stained tumor slices of the mice after being treated by DHA@FCM + magnet. (c) Schematic illustration of multifunctional DOX-loaded Fe_3O_4@polyacrylic acid/Au nanoclusters/ZIF-8 nanoparticles integrating tri-modal cancer imaging and chemotherapy into one system. (d) Schematic illustration of various biomacromolecules, encapsulated within the porous and crystalline MOF shell. (e) Protective performance of ZIF-8 coatings on HRP compared with other controls under different conditions. (f) Fluorescence measurement of the PBS solution containing ZIF-8/DQ-OVA and ZIF-8/trypsin particles. (g) Schematic illustration showing the release of DQ-OVA (red) and trypsin (yellow) from ZIF-8 biocomposites at pH 6.0, and degradation of DQ-OVA into fluorescent fragments as a result of proteolysis by trypsin. (h) Schematic illustration of biomimetic crystallization of cytoprotective MOF coatings on living cells. (i) SEM image of ZIF-8 coated yeast. The inset of (i) is cellular cross section. (j) Cell viability (%) of native yeast (blue) and native yeast with free ZIF-8 particles (patterned blue) in the presence of cell lysis enzyme lyticase for 3 h, and ZIF-8 coated yeast in the presence of lyticase for 3 h (red) and 24 h (patterned red). (a and b) Reproduced with permission from ref. 333. Copyright 2016, Elsevier Ltd. (c) Reproduced with permission from ref. 334. Copyright 2015, Royal Society of Chemistry. (d–g) Reproduced with permission from ref. 63. Copyright 2015, Nature Publishing Group. (h–j) Reproduced with permission from ref. 41. Copyright 2016, Wiley-VCH.

the biomolecule-rich surface of living yeast cells induced the heterogeneous nucleation and growth of a robust ZIF-8 coating. As shown in Fig. 20i, the individual yeast cells were homogeneously coated with ZIF-8 nanoparticles, making them possess rough surfaces. To investigate the protection from MOF coatings, the cell viability of ZIF-8 coated yeast was monitored in the presence of a cell lysis enzyme (lyticase). The cell viability ratios of ZIF-8 coated yeast after being treated for 3 and 24 h were 94.5% and 81%, respectively (Fig. 20j). However, the cell viability ratios of native yeast and native yeast with free ZIF-8 particles were less than 10%. This difference was mainly attributed to the selective permeability of the ZIF-8 shell against the cytotoxic enzymatic agent. Furthermore, after removal of the ZIF-8 shell *via* EDTA, the cells immediately grew and regained full functionality. Therefore, the ZIF-8 shell can efficiently suppress cell division without activity loss and thus extend the lifetime of the cell.

5. Conclusions and outlook

This review systemically summarizes the recent advances in versatile synthesis strategies and broad applications of

MOF coatings. An in-depth understanding of the fundamental chemistry, classifications and functions of MOF coatings are also provided. From the perspective of synthesis chemistry, five synthesis methods for MOF coatings are summarized and emphasized, including liquid–liquid, solid–liquid, solid–solid, solid–gas and gas–gas synthesis methods. Importantly, based on their structural features, well-defined MOF coatings integrated with other functional materials show great potential in many frontier applications, including batteries, supercapacitors, electrocatalysis, gas separation, gas adsorption and storage, sensors, photocatalysis, hydrogenation and drug delivery/cytoprotection. Some typical examples and their structure–property correlations are highlighted and discussed in detail. Although great progress in MOF coatings has been acquired in the past decade, there is still a long way to go for practical and emerging applications. For the future research of MOF coatings, some important aspects and opportunities need to be considered.

(1) Precise control of functional MOF coatings for high-performance applications in terms of their tunable components, porosity, structural arrangement, size and/or morphology. Up to now, the ever and increasing number of MOFs provide great space for MOF coatings. Many MOFs with unique functions have been successfully developed, including catalytic MOFs, photoactive MOFs, magnetic MOFs, bio-mimicking MOFs, and conductive MOFs. However, to acquire high performance, more modifications of MOF coatings should be performed, including with respect to components, porosity, structural arrangement, size and/or morphology. For example, by modulating metal ions in MOFs, bimetallic Co,Ni-MOFs showed greatly enhanced electrocatalytic OER activity compared with single Co-MOFs and Ni-MOFs due to the coupling effect between Co and Ni. In addition, nanostructured MOFs possess rich coordinatively unsaturated metal atoms as the dominating active sites for the electrocatalytic OER, resulting in superior OER activity than bulk MOFs.

(2) Exploration of new functional materials integrated with MOF coatings. Currently, the already reported integrated functional materials include inorganic compounds, carbon materials, hard substrates, metal nanocrystals, MOF crystals, polymers, molecules, biomaterials and so on. As discussed above, functional materials with a variety of properties (*e.g.* electrocatalytic, biological, photonic, magnetic, plasmonic, thermochromic, up- and down-conversion properties) are successfully introduced into MOF coatings, endowing the composites with these additional functions. Therefore, the exploration of functional materials with new properties for integration into the composites is important for new applications, which opens up new avenues to achieve high-performance and multifunctional composites.

(3) New strategies to engineer the spatial distribution and interfacial interactions between MOFs and functional materials. The performances of the obtained composites are strongly influenced by their guest–host structures and interactions. During the liquid–liquid synthesis process, modulation of some parameters (*e.g.* concentration, temperature, time, pH and solvent) and surface modifications (*e.g.* surfactants, polymers and additives) are usually carried out to modulate the growth kinetics and spatial distribution of MOF coatings, thereby forming well-defined composites. Furthermore, more efficient strategies to realize controlled spatial distribution and strong host–guest interactions of the composites are highly desired in the near future research.

(4) In-depth understanding of the structure–property relationships in MOF-coated composites. In comprehensive applications, the obtained MOF-coated composites displayed many unique properties/phenomena, including electron coupling effect, adsorption kinetics, synergistic effect, spillover effect, photoresponse, heat transfer mechanism, and energy gap modulation. Furthermore, advanced *in/ex situ* techniques and calculated simulations as powerful tools are carried out to reveal their host–guest interactions and working mechanisms, greatly improving the fundamental understanding.[230,337,338] The fundamental understanding will guide the design of high-performance MOF-coated composites.

(5) The introduction of MOF-coated composites into new interdisciplinary fields. In addition to the applications highlighted in Part 4, unique MOF coatings with distinguishing features have also shown great potential for new interdisciplinary fields in recent years. For example, Zr-based MOF coatings efficiently protect anaerobic bacteria *via* decomposition of reactive oxygen species, thereby improving their life throughout reproduction in artificial photosynthesis.[335] ZIF-8 coatings as air filters could simultaneously realize particulate matter filtration and bacteria-killing function due to their pore structures and photocatalytic bactericidal activity.[339,340] MIL-101-SO_3 coatings reduce the magnetism of Fe_3O_4 cores *via* their oxidation effect.[341] Therefore, high performances and new properties in new interdisciplinary fields are highly dependent on the best use of MOF coatings.

(6) Low cost and high throughput towards large-scale practical applications. The synthesis cost of MOF coatings mainly comes from both raw materials and fabrication processes. To realize low cost, the raw materials of MOF coatings should be from earth-abundant elements and/or compounds. On the other hand, the fabrication strategy requires easy operation, simple experimental facilities, less by-products and high throughput.[342,343] By comparing the synthesis strategies mentioned in Part 3, solid–solid and solid–gas synthesis methods show greater potential than others in terms of cost and throughput. But unfortunately, the obtained MOF coatings are of unsatisfactory quality. The choice of synthesis strategies for one special application is a trade-off among cost, throughput and quality. For widespread industry applications, the development of new, efficient, low-cost and high-throughput strategies is highly desired in future research.

Although many challenges still exist, the rapid development of MOF coatings in the last decade has brought better directions into the rational design of high-performance MOF-coated composites. A systematic summary and comprehensive understanding highlighted in this review will build a solid platform towards the engineering of novel MOF coatings and open up new opportunities for practical MOF applications.

Conflicts of interest

There are no conflicts to declare.

Acknowledgements

This work was supported by the National Natural Science Foundation of China (51832004 and 51521001), the National Key Research and Development Program of China (2016YFA0202603), the Natural Science Foundation of Hubei Province (2019CFA001), the Programme of Introducing Talents of Discipline to Universities (B17034), and the Yellow Crane Talent (Science & Technology) Program of Wuhan City.

Notes and references

1 H. C. Zhou, J. R. Long and O. M. Yaghi, *Chem. Rev.*, 2012, **112**, 673–674.
2 Q. L. Zhu and Q. Xu, *Chem. Soc. Rev.*, 2014, **43**, 5468–5512.
3 N. Stock and S. Biswas, *Chem. Rev.*, 2012, **112**, 933–969.
4 M. Eddaoudi, D. F. Sava, J. F. Eubank, K. Adil and V. Guillerm, *Chem. Soc. Rev.*, 2015, **44**, 228–249.
5 S. Furukawa, J. Reboul, S. Diring, K. Sumida and S. Kitagawa, *Chem. Soc. Rev.*, 2014, **43**, 5700–5734.
6 W. Y. Gao, M. Chrzanowski and S. Ma, *Chem. Soc. Rev.*, 2014, **43**, 5841–5866.
7 Y. Sun and H. C. Zhou, *Sci. Technol. Adv. Mater.*, 2015, **16**, 054202.
8 P. Falcaro, R. Ricco, C. M. Doherty, K. Liang, A. J. Hill and M. J. Styles, *Chem. Soc. Rev.*, 2014, **43**, 5513–5560.
9 J. Bitzer and W. Kleist, *Chem. – Eur. J.*, 2019, **25**, 1866–1882.
10 Y.-z. Li, Z.-h. Fu and G. Xu, *Coord. Chem. Rev.*, 2019, **388**, 79–106.
11 P. Yang, W. Zhao, A. Shkurenko, Y. Belmabkhout, M. Eddaoudi, X. Dong, H. N. Alshareef and N. M. Khashab, *J. Am. Chem. Soc.*, 2019, **141**, 1847–1851.
12 Y. Cui, B. Li, H. He, W. Zhou, B. Chen and G. Qian, *Acc. Chem. Res.*, 2016, **49**, 483–493.
13 J. Zhou and B. Wang, *Chem. Soc. Rev.*, 2017, **46**, 6927–6945.
14 V. Stavila, A. A. Talin and M. D. Allendorf, *Chem. Soc. Rev.*, 2014, **43**, 5994–6010.
15 P. Ramaswamy, N. E. Wong and G. K. Shimizu, *Chem. Soc. Rev.*, 2014, **43**, 5913–5932.
16 H. N. Miras, L. Vila-Nadal and L. Cronin, *Chem. Soc. Rev.*, 2014, **43**, 5679–5699.
17 W. G. Lu, Z. W. Wei, Z. Y. Gu, T. F. Liu, J. Park, J. Park, J. Tian, M. W. Zhang, Q. Zhang, T. Gentle, M. Bosch and H. C. Zhou, *Chem. Soc. Rev.*, 2014, **43**, 5561–5593.
18 M. Usman, S. Mendiratta and K. L. Lu, *Adv. Mater.*, 2017, **29**, 1605071.
19 X. Wu, J. J. Hong, W. Shin, L. Ma, T. Liu, X. Bi, Y. Yuan, Y. Qi, T. W. Surta, W. Huang, J. Neuefeind, T. Wu, P. A. Greaney, J. Lu and X. Ji, *Nat. Energy*, 2019, **4**, 123–130.
20 Z. Xue, Y. Li, Y. Zhang, W. Geng, B. Jia, J. Tang, S. Bao, H.-P. Wang, Y. Fan, Z.-W. Wei, Z. Zhang, Z. Ke, G. Li and C.-Y. Su, *Adv. Energy Mater.*, 2018, **8**, 1801564.
21 S.-L. Li and Q. Xu, *Energy Environ. Sci.*, 2013, **6**, 1656–1683.
22 X. Li, S. Zheng, L. Jin, Y. Li, P. Geng, H. Xue, H. Pang and Q. Xu, *Adv. Energy Mater.*, 2018, **8**, 1800716.
23 K. J. Lee, J. H. Lee, S. Jeoung and H. R. Moon, *Acc. Chem. Res.*, 2017, **50**, 2684–2692.
24 Z. G. Gu, D. X. Zhang, W. Q. Fu, Z. H. Fu, M. I. Vohra, L. Zhang, C. Woll and J. Zhang, *Inorg. Chem.*, 2017, **56**, 3526–3531.
25 R. R. Salunkhe, Y. V. Kaneti, J. Kim, J. H. Kim and Y. Yamauchi, *Acc. Chem. Res.*, 2016, **49**, 2796–2806.
26 J. Meng, C. Niu, L. Xu, J. Li, X. Liu, X. Wang, Y. Wu, X. Xu, W. Chen, Q. Li, Z. Zhu, D. Zhao and L. Mai, *J. Am. Chem. Soc.*, 2017, **139**, 8212–8221.
27 H. Sun, Y. Lian, C. Yang, L. Xiong, P. Qi, Q. Mu, X. Zhao, J. Guo, Z. Deng and Y. Peng, *Energy Environ. Sci.*, 2018, **11**, 2363–2371.
28 L. Zou, C. C. Hou, Z. Liu, H. Pang and Q. Xu, *J. Am. Chem. Soc.*, 2018, **140**, 15393–15401.
29 S. Kempahanumakkagari, K. Vellingiri, A. Deep, E. E. Kwon, N. Bolan and K.-H. Kim, *Coord. Chem. Rev.*, 2018, **357**, 105–129.
30 Y. Liu and Z. Tang, *Adv. Mater.*, 2013, **25**, 5819–5825.
31 P. Falcaro, R. Ricco, A. Yazdi, I. Imaz, S. Furukawa, D. Maspoch, R. Ameloot, J. D. Evans and C. J. Doonan, *Coord. Chem. Rev.*, 2016, **307**, 237–254.
32 T. Kitao, Y. Zhang, S. Kitagawa, B. Wang and T. Uemura, *Chem. Soc. Rev.*, 2017, **46**, 3108–3133.
33 Z. Liang, C. Qu, W. Guo, R. Zou and Q. Xu, *Adv. Mater.*, 2018, **30**, 1702891.
34 Y. Zhao, Z. Song, X. Li, Q. Sun, N. Cheng, S. Lawes and X. Sun, *Energy Storage Mater.*, 2016, **2**, 35–62.
35 L. Chen and Q. Xu, *Matter*, 2019, **1**, 57–89.
36 Q. Zhang, Z. Yang, B. Chen and X. Liang, *Chem. Commun.*, 2019, **55**, 8450–8453.
37 M. D. Tikekar, S. Choudhury, Z. Tu and L. A. Archer, *Nat. Energy*, 2016, **1**, 16114.
38 D. Larcher and J. M. Tarascon, *Nat. Chem.*, 2015, **7**, 19–29.
39 G. Lu, S. Li, Z. Guo, O. K. Farha, B. G. Hauser, X. Qi, Y. Wang, X. Wang, S. Han, X. Liu, J. S. DuChene, H. Zhang, Q. Zhang, X. Chen, J. Ma, S. C. Loo, W. D. Wei, Y. Yang, J. T. Hupp and F. Huo, *Nat. Chem.*, 2012, **4**, 310–316.
40 G. Li, H. Kobayashi, J. M. Taylor, R. Ikeda, Y. Kubota, K. Kato, M. Takata, T. Yamamoto, S. Toh, S. Matsumura and H. Kitagawa, *Nat. Mater.*, 2014, **13**, 802–806.
41 K. Liang, J. J. Richardson, J. Cui, F. Caruso, C. J. Doonan and P. Falcaro, *Adv. Mater.*, 2016, **28**, 7910–7914.
42 Y. Liu, Y. Ban and W. Yang, *Adv. Mater.*, 2017, **29**, 1606949.
43 R. Zhao, Z. Liang, R. Zou and Q. Xu, *Joule*, 2018, **2**, 2235–2259.
44 Y. Yan, T. He, B. Zhao, K. Qi, H. Liu and B. Y. Xia, *J. Mater. Chem. A*, 2018, **6**, 15905–15926.
45 G. Xu, P. Nie, H. Dou, B. Ding, L. Li and X. Zhang, *Mater. Today*, 2017, **20**, 191–209.
46 H. Wang, Q.-L. Zhu, R. Zou and Q. Xu, *Chem*, 2017, **2**, 52–80.
47 D. Liu, J. Wan, G. Pang and Z. Tang, *Adv. Mater.*, 2018, **30**, 1803291.
48 W. Yang, X. Li, Y. Li, R. Zhu and H. Pang, *Adv. Mater.*, 2019, **31**, 1804740.
49 H. Wu and X. Lou, *Sci. Adv.*, 2017, **3**, eaap9252.

50 G. Ferey, C. Mellot-Draznieks, C. Serre, F. Millange, J. Dutour, S. Surble and I. Margiolaki, *Science*, 2005, **309**, 2040–2042.
51 K. S. Park, Z. Ni, A. P. Cote, J. Y. Choi, R. Huang, F. J. Uribe-Romo, H. K. Chae, M. O'Keeffe and O. M. Yaghi, *Proc. Natl. Acad. Sci. U. S. A.*, 2006, **103**, 10186–10191.
52 M. Jahan, Q. Bao and K. P. Loh, *J. Am. Chem. Soc.*, 2012, **134**, 6707–6713.
53 X. Huang, B. Zheng, Z. D. Liu, C. L. Tan, J. Q. Liu, B. Chen, H. Li, J. Z. Chen, X. Zhang, Z. X. Fan, W. N. Zhang, Z. Guo, F. W. Huo, Y. H. Yang, L. H. Xie, W. Huang and H. Zhang, *ACS Nano*, 2014, **8**, 8695–8701.
54 Q. He, J. Liu, Z. Li, Q. Li, L. Xu, B. Zhang, J. Meng, Y. Wu and L. Mai, *Small*, 2017, **13**, 1701504.
55 J. Tang, R. R. Salunkhe, J. Liu, N. L. Torad, M. Imura, S. Furukawa and Y. Yamauchi, *J. Am. Chem. Soc.*, 2015, **137**, 1572–1580.
56 B. Li, H. M. Wen, H. Wang, H. Wu, M. Tyagi, T. Yildirim, W. Zhou and B. Chen, *J. Am. Chem. Soc.*, 2014, **136**, 6207–6210.
57 D. Sheberla, J. C. Bachman, J. S. Elias, C. J. Sun, Y. Shao-Horn and M. Dinca, *Nat. Mater.*, 2017, **16**, 220–224.
58 F. L. Li, Q. Shao, X. Huang and J. P. Lang, *Angew. Chem., Int. Ed.*, 2018, **57**, 1888–1892.
59 J. Duan, S. Chen and C. Zhao, *Nat. Commun.*, 2017, **8**, 15341.
60 A. Henschel, K. Gedrich, R. Kraehnert and S. Kaskel, *Chem. Commun.*, 2008, 4192–4194, DOI: 10.1039/b718371b.
61 H. Khajavi, H. A. Stil, H. P. C. E. Kuipers, J. Gascon and F. Kapteijn, *ACS Catal.*, 2013, **3**, 2617–2626.
62 X. L. Ma, P. Kumar, N. Mittal, A. Khlyustova, P. Daoutidis, K. A. Mkhoyan and M. Tsapatsis, *Science*, 2018, **361**, 1008–1011.
63 K. Liang, R. Ricco, C. M. Doherty, M. J. Styles, S. Bell, N. Kirby, S. Mudie, D. Haylock, A. J. Hill, C. J. Doonan and P. Falcaro, *Nat. Commun.*, 2015, **6**, 7240.
64 J. Wang, G. Han, L. Wang, L. Du, G. Chen, Y. Gao, Y. Ma, C. Du, X. Cheng, P. Zuo and G. Yin, *Small*, 2018, **14**, e1704282.
65 W.-H. Li, K. Ding, H.-R. Tian, M.-S. Yao, B. Nath, W.-H. Deng, Y. Wang and G. Xu, *Adv. Funct. Mater.*, 2017, **27**, 1702067.
66 L. Sun, M. G. Campbell and M. Dincă, *Angew. Chem., Int. Ed.*, 2016, **55**, 3566–3579.
67 D. M. D'Alessandro, J. R. Kanga and J. S. Caddy, *Aust. J. Chem.*, 2011, **64**, 718–722.
68 H. L. Jiang, Q. P. Lin, T. Akita, B. Liu, H. Ohashi, H. Oji, T. Honma, T. Takei, M. Haruta and Q. Xu, *Chem. – Eur. J.*, 2011, **17**, 78–81.
69 Q. L. Zhu, J. Li and Q. Xu, *J. Am. Chem. Soc.*, 2013, **135**, 10210–10213.
70 P. Hu, J. V. Morabito and C.-K. Tsung, *ACS Catal.*, 2014, **4**, 4409–4419.
71 J. Yu, C. Mu, B. Yan, X. Qin, C. Shen, H. Xue and H. Pang, *Mater. Horiz.*, 2017, **4**, 557–569.
72 J. Aguilera-Sigalat and D. Bradshaw, *Coord. Chem. Rev.*, 2016, **307**, 267–291.
73 L. Zhang, H. Chen, X. Bai, S. Wang, L. Li, L. Shao, W. He, Y. Li, T. Wang, X. Zhang, J. Chen and Y. Fu, *Chem. Commun.*, 2019, **55**, 8293–8296.
74 O. Shekhah, H. Wang, S. Kowarik, F. Schreiber, M. Paulus, M. Tolan, C. Sternemann, F. Evers, D. Zacher, R. A. Fischer and C. Woll, *J. Am. Chem. Soc.*, 2007, **129**, 15118–15119.
75 M. Li, Z. Zheng, Y. Zheng, C. Cui, C. Li and Z. Li, *ACS Appl. Mater. Interfaces*, 2017, **9**, 2899–2905.
76 Z.-G. Gu and J. Zhang, *Coord. Chem. Rev.*, 2019, **378**, 513–532.
77 S. Khanjani and A. Morsali, *Ultrason. Sonochem.*, 2014, **21**, 1424–1429.
78 Y. Han, D. Yu, J. Zhou, P. Xu, P. Qi, Q. Wang, S. Li, X. Fu, X. Gao, C. Jiang, X. Feng and B. Wang, *Chem. – Eur. J.*, 2017, **23**, 11513–11518.
79 B. Y. Guan, L. Yu and X. W. D. Lou, *Adv. Sci.*, 2017, **4**, 1700247.
80 Z. Li and H. C. Zeng, *J. Am. Chem. Soc.*, 2014, **136**, 5631–5639.
81 P. Rocio-Bautista, I. Pacheco-Fernandez, J. Pasan and V. Pino, *Anal. Chim. Acta*, 2016, **939**, 26–41.
82 X. Shi, A. Wu, H. Yan, L. Zhang, C. Tian, L. Wang and H. Fu, *J. Mater. Chem. A*, 2018, **6**, 20100–20109.
83 J. Zhao, B. Gong, W. T. Nunn, P. C. Lemaire, E. C. Stevens, F. I. Sidi, P. S. Williams, C. J. Oldham, H. J. Walls, S. D. Shepherd, M. A. Browe, G. W. Peterson, M. D. Losego and G. N. Parsons, *J. Mater. Chem. A*, 2015, **3**, 1458–1464.
84 H. X. Zhong, J. Wang, Y. W. Zhang, W. L. Xu, W. Xing, D. Xu, Y. F. Zhang and X. B. Zhang, *Angew. Chem., Int. Ed.*, 2014, **53**, 14235–14239.
85 B. Xi, Y. C. Tan and H. C. Zeng, *Chem. Mater.*, 2015, **28**, 326–336.
86 P. Hu, J. Zhuang, L. Y. Chou, H. K. Lee, X. Y. Ling, Y. C. Chuang and C. K. Tsung, *J. Am. Chem. Soc.*, 2014, **136**, 10561–10564.
87 Y. Long, L. Xiao, Q. Cao, X. Shi and Y. Wang, *Chem. Commun.*, 2017, **53**, 10831–10834.
88 G. Huang, D. M. Yin and L. M. Wang, *J. Mater. Chem. A*, 2016, **4**, 15106–15116.
89 N. Campagnol, T. R. C. Van Assche, M. Li, L. Stappers, M. Dincă, J. F. M. Denayer, K. Binnemans, D. E. De Vos and J. Fransaer, *J. Mater. Chem. A*, 2016, **4**, 3914–3925.
90 I. Hod, W. Bury, D. M. Karlin, P. Deria, C. W. Kung, M. J. Katz, M. So, B. Klahr, D. Jin, Y. W. Chung, T. W. Odom, O. K. Farha and J. T. Hupp, *Adv. Mater.*, 2014, **26**, 6295–6300.
91 W.-J. Li, M. Tu, R. Cao and R. A. Fischer, *J. Mater. Chem. A*, 2016, **4**, 12356–12369.
92 H. Lan, D. Pan, Y. Sun, Y. Guo and Z. Wu, *Anal. Chim. Acta*, 2016, **937**, 53–60.
93 H. Al-Kutubi, J. Gascon, E. J. R. Sudhölter and L. Rassaei, *ChemElectroChem*, 2015, **2**, 462–474.
94 W.-J. Li, J. Lu, S.-Y. Gao, Q.-H. Li and R. Cao, *J. Mater. Chem. A*, 2014, **2**, 19473–19478.
95 M. Li and M. Dincă, *Chem. Mater.*, 2015, **27**, 3203–3206.
96 S. El-Hankari, J. Aguilera-Sigalat and D. Bradshaw, *J. Mater. Chem. A*, 2016, **4**, 13509–13518.
97 Y. Z. Zhang, T. Cheng, Y. Wang, W. Y. Lai, H. Pang and W. Huang, *Adv. Mater.*, 2016, **28**, 5242–5248.
98 G. Zhang, S. Hou, H. Zhang, W. Zeng, F. Yan, C. C. Li and H. Duan, *Adv. Mater.*, 2015, **27**, 2400–2405.

99 W. W. Zhan, Q. Kuang, J. Z. Zhou, X. J. Kong, Z. X. Xie and L. S. Zheng, *J. Am. Chem. Soc.*, 2013, **135**, 1926–1933.
100 G. Cai, W. Zhang, L. Jiao, S.-H. Yu and H.-L. Jiang, *Chem*, 2017, **2**, 791–802.
101 Y. Zheng and S.-Z. Qiao, *Chem*, 2017, **2**, 751–752.
102 X. Song, S. Chen, L. Guo, Y. Sun, X. Li, X. Cao, Z. Wang, J. Sun, C. Lin and Y. Wang, *Adv. Energy Mater.*, 2018, **8**, 1801101.
103 Q. Gan, H. He, K. Zhao, Z. He and S. Liu, *Electrochim. Acta*, 2018, **266**, 254–262.
104 Q. Gan, K. Zhao, S. Liu and Z. He, *Electrochim. Acta*, 2017, **250**, 292–301.
105 G. Zou, H. Hou, G. Zhao, P. Ge, D. Yin and X. Ji, *J. Mater. Chem. A*, 2018, **6**, 4839–4847.
106 G. Zhan and H. C. Zeng, *Chem. Commun.*, 2016, **53**, 72–81.
107 S. M. Meckler, C. Li, W. L. Queen, T. E. Williams, J. R. Long, R. Buonsanti, D. J. Milliron and B. A. Helms, *Chem. Mater.*, 2015, **27**, 7673–7679.
108 C. Mottillo and T. Friscic, *Molecules*, 2017, **22**, 144.
109 W. Yuan, J. O'Connor and S. L. James, *CrystEngComm*, 2010, **12**, 3515–3517.
110 C. Mottillo, Y. N. Lu, M. H. Pham, M. J. Cliffe, T. O. Do and T. Friscic, *Green Chem.*, 2013, **15**, 2121–2131.
111 P. J. Beldon, L. Fabian, R. S. Stein, A. Thirumurugan, A. K. Cheetham and T. Friscic, *Angew. Chem., Int. Ed.*, 2010, **49**, 9640–9643.
112 L. Paseta, G. Potier, S. Sorribas and J. Coronas, *ACS Sustainable Chem. Eng.*, 2016, **4**, 3780–3785.
113 S. Tanaka, K. Kida, T. Nagaoka, T. Ota and Y. Miyake, *Chem. Commun.*, 2013, **49**, 7884–7886.
114 M. J. Cliffe, C. Mottillo, R. S. Stein, D.-K. Bučar and T. Friščić, *Chem. Sci.*, 2012, **3**, 2495–2500.
115 Y. F. Chen, S. Q. Li, X. K. Pei, J. W. Zhou, X. Feng, S. H. Zhang, Y. Y. Cheng, H. W. Li, R. D. Han and B. Wang, *Angew. Chem., Int. Ed.*, 2016, **55**, 3419–3423.
116 C. Young, J. Wang, J. Kim, Y. Sugahara, J. Henzie and Y. Yamauchi, *Chem. Mater.*, 2018, **30**, 3379–3386.
117 X. Meng, *J. Mater. Chem. A*, 2017, **5**, 18326–18378.
118 S. Hermes, D. Zacher, A. Baunemann, C. Woll and R. A. Fischer, *Chem. Mater.*, 2007, **19**, 2168–2173.
119 W. Li, P. Su, Z. Li, Z. Xu, F. Wang, H. Ou, J. Zhang, G. Zhang and E. Zeng, *Nat. Commun.*, 2017, **8**, 406.
120 Z. Xiao, J. Meng, Q. Li, X. Wang, M. Huang, Z. Liu, C. Han and L. Mai, *Sci. Bull.*, 2018, **63**, 46–53.
121 I. Stassen, M. Styles, G. Grenci, H. V. Gorp, W. Vanderlinden, S. D. Feyter, P. Falcaro, D. D. Vos, P. Vereecken and R. Ameloot, *Nat. Mater.*, 2016, **15**, 304–310.
122 J. Meng, X. Liu, J. Li, Q. Li, C. Zhao, L. Xu, X. Wang, F. Liu, W. Yang, X. Xu, Z. Liu, C. Niu and L. Mai, *Nano Lett.*, 2017, **17**, 7773–7781.
123 D. T. Lee, J. Zhao, G. W. Peterson and G. N. Parsons, *Chem. Mater.*, 2017, **29**, 4894–4903.
124 E. Ahvenniemi and M. Karppinen, *Chem. Commun.*, 2016, **52**, 1139–1142.
125 E. Ahvenniemi and M. Karppinen, *Chem. Mater.*, 2016, **28**, 6260–6265.
126 Y. S. Park, H. Kim, B. Cho, C. Lee, S. E. Choi, M. M. Sung and J. S. Lee, *ACS Appl. Mater. Interfaces*, 2016, **8**, 17489–17498.
127 Q. Peng, B. Gong, R. M. VanGundy and G. N. Parsons, *Chem. Mater.*, 2009, **21**, 820–830.
128 K. B. Lausund and O. Nilsen, *Nat. Commun.*, 2016, **7**, 13578.
129 J. Liu, Z. Bao, Y. Cui, E. J. Dufek, J. B. Goodenough, P. Khalifah, Q. Li, B. Y. Liaw, P. Liu, A. Manthiram, Y. S. Meng, V. R. Subramanian, M. F. Toney, V. V. Viswanathan, M. S. Whittingham, J. Xiao, W. Xu, J. Yang, X.-Q. Yang and J.-G. Zhang, *Nat. Energy*, 2019, **4**, 180–186.
130 J. Meng, H. Guo, C. Niu, Y. Zhao, L. Xu, Q. Li and L. Mai, *Joule*, 2017, **1**, 522–547.
131 C. Niu, H. Pan, W. Xu, J. Xiao, J. G. Zhang, L. Luo, C. Wang, D. Mei, J. Meng, X. Wang, Z. Liu, L. Mai and J. Liu, *Nat. Nanotechnol.*, 2019, **14**, 594–601.
132 X. Zeng, M. Li, D. Abd El-Hady, W. Alshitari, A. S. Al-Bogami, J. Lu and K. Amine, *Adv. Energy Mater.*, 2019, **9**, 1900161.
133 J. Meng, Z. Liu, C. Niu, L. Xu, X. Wang, Q. Li, X. Wei, W. Yang, L. Huang and L. Mai, *Mater. Horiz.*, 2018, **5**, 78–85.
134 Y. Liu, Y. Zhu and Y. Cui, *Nat. Energy*, 2019, **4**, 540–550.
135 C. S. Yan, H. Y. Gao, L. Le Gong, L. F. Ma, L. L. Dang, L. Zhang, P. P. Meng and F. Luo, *J. Mater. Chem. A*, 2016, **4**, 13603–13610.
136 L. Yang, Y. Tian, P. Ge, G. Zhao, T. Pu, Y. Yang, G. Zou, H. Hou, L. Huang and X. Ji, *ChemElectroChem*, 2018, **5**, 3426–3436.
137 K. Wang, S. Pei, Z. He, L.-A. Huang, S. Zhu, J. Guo, H. Shao and J. Wang, *Chem. Eng. J.*, 2019, **356**, 272–281.
138 B. Tang, A. Li, Y. Tong, H. Song, X. Chen, J. Zhou and Z. Ma, *J. Alloys Compd.*, 2017, **708**, 6–13.
139 Y. Liao, C. Li, X. Lou, X. Hu, Y. Ning, F. Yuan, B. Chen, M. Shen and B. Hu, *Electrochim. Acta*, 2018, **271**, 608–616.
140 J. Meng, Q. He, L. Xu, X. Zhang, F. Liu, X. Wang, Q. Li, X. Xu, G. Zhang, C. Niu, Z. Xiao, Z. Liu, Z. Zhu, Y. Zhao and L. Mai, *Adv. Energy Mater.*, 2019, **9**, 1802695.
141 Y. Wu, J. Meng, Q. Li, C. Niu, X. Wang, W. Yang, W. Li and L. Mai, *Nano Res.*, 2017, **10**, 2364–2376.
142 W. Sun, X. Tang, Q. Yang, Y. Xu, F. Wu, S. Guo, Y. Zhang, M. Wu and Y. Wang, *Adv. Mater.*, 2019, **31**, e1903176.
143 C. Zhu, R. E. Usiskin, Y. Yu and J. Maier, *Science*, 2017, **358**, eaao2808.
144 W. Li, S. Hu, X. Luo, Z. Li, X. Sun, M. Li, F. Liu and Y. Yu, *Adv. Mater.*, 2017, **29**, 1605820.
145 X. Zhou, L. Chen, W. Zhang, J. Wang, Z. Liu, S. Zeng, R. Xu, Y. Wu, S. Ye, Y. Feng, X. Cheng, Z. Peng, X. Li and Y. Yu, *Nano Lett.*, 2019, **19**, 4965–4973.
146 X. Sun, G. Gao, D. Yan and C. Feng, *Appl. Surf. Sci.*, 2017, **405**, 52–59.
147 Z. Chen, D. Chao, J. Lin and Z. Shen, *Mater. Res. Bull.*, 2017, **96**, 491–502.
148 Q.-Q. Qiao, G.-R. Li, Y.-L. Wang and X.-P. Gao, *J. Mater. Chem. A*, 2016, **4**, 4440–4447.
149 K. Hurlbutt, S. Wheeler, I. Capone and M. Pasta, *Joule*, 2018, **2**, 1950–1960.

150 B. Wang, Y. Han, X. Wang, N. Bahlawaneet, H. Pan, M. Yan and Y. Jiang, *iScience*, 2018, **3**, 110–133.
151 Y. Lu, L. Wang, J. Cheng and J. B. Goodenough, *Chem. Commun.*, 2012, **48**, 6544–6546.
152 M. Morant-Giner, R. Sanchis-Gual, J. Romero, A. Alberola, L. García-Cruz, S. Agouram, M. Galbiati, N. M. Padial, J. C. Waerenborgh, C. Martí-Gastaldo, S. Tatay, A. Forment-Aliaga and E. Coronado, *Adv. Funct. Mater.*, 2018, **28**, 1706125.
153 P. Li, K. Zhang and J. H. Park, *J. Mater. Chem. A*, 2018, **6**, 1900–1914.
154 D. Yin, G. Huang, Q. Sun, Q. Li, X. Wang, D. Yuan, C. Wang and L. Wang, *Electrochim. Acta*, 2016, **215**, 410–419.
155 S. Li, X. Fu, J. Zhou, Y. Han, P. Qi, X. Gao, X. Feng and B. Wang, *J. Mater. Chem. A*, 2016, **4**, 5823–5827.
156 Y. Jin, C. Zhao, Z. Sun, Y. Lin, L. Chen, D. Wang and C. Shen, *RSC Adv.*, 2016, **6**, 30763–30768.
157 Y. Han, P. Qi, J. Zhou, X. Feng, S. Li, X. Fu, J. Zhao, D. Yu and B. Wang, *ACS Appl. Mater. Interfaces*, 2015, **7**, 26608–26613.
158 Y. Yu, C. Yue, X. Lin, S. Sun, J. Gu, X. He, C. Zhang, W. Lin, D. Lin, X. Liao, B. Xu, S. Wu, M. Zheng, J. Li, J. Kang and L. Lin, *ACS Appl. Mater. Interfaces*, 2016, **8**, 3992–3999.
159 P. Qi, Y. Han, J. Zhou, X. Fu, S. Li, J. Zhao, L. Wang, X. Fan, X. Feng and B. Wang, *Chem. Commun.*, 2015, **51**, 12391–12394.
160 Y. Han, P. Qi, X. Feng, S. Li, X. Fu, H. Li, Y. Chen, J. Zhou, X. Li and B. Wang, *ACS Appl. Mater. Interfaces*, 2015, **7**, 2178–2182.
161 Q. Gan, K. Zhao, S. Liu and Z. He, *J. Mater. Sci.*, 2017, **52**, 7768–7780.
162 Z.-D. Huang, Z. Gong, Q. Kang, Y. Fang, X.-S. Yang, R. Liu, X. Lin, X. Feng, Y. Ma and D. Wang, *Mater. Chem. Front.*, 2017, **1**, 1975–1981.
163 X. Liu, S. Zhang, Y. Xing, S. Wang, P. Yang and H. Li, *New J. Chem.*, 2016, **40**, 9679–9683.
164 F. Li, J. Du, H. Yang, W. Shi and P. Cheng, *RSC Adv.*, 2017, **7**, 20062–20067.
165 M. Zhong, D. Yang, C. Xie, Z. Zhang, Z. Zhou and X. H. Bu, *Small*, 2016, **12**, 5564–5571.
166 X. Xu, C. Qi, Z. Hao, H. Wang, J. Jiu, J. Liu, H. Yan and K. Suganuma, *Nano-Micro Lett.*, 2018, **10**, 1.
167 S. K. Park and Y. C. Kang, *ACS Appl. Mater. Interfaces*, 2018, **10**, 17203–17213.
168 Z. Jiang, T. Liu, L. Yan, J. Liu, F. Dong, M. Ling, C. Liang and Z. Lin, *Energy Storage Mater.*, 2018, **11**, 267–273.
169 D. H. Lee, J. H. Ahn, M.-S. Park, A. Eftekhari and D.-W. Kim, *Electrochim. Acta*, 2018, **283**, 1291–1299.
170 M. Li, Y. Wan, J.-K. Huang, A. H. Assen, C.-E. Hsiung, H. Jiang, Y. Han, M. Eddaoudi, Z. Lai, J. Ming and L.-J. Li, *ACS Energy Lett.*, 2017, **2**, 2362–2367.
171 S. Suriyakumar, A. M. Stephan, N. Angulakshmi, M. H. Hassan and M. H. Alkordi, *J. Mater. Chem. A*, 2018, **6**, 14623–14632.
172 J. Balach, J. Linnemann, T. Jaumann and L. Giebeler, *J. Mater. Chem. A*, 2018, **6**, 23127–23168.
173 G. Xu, Y. Zuo and B. Huang, *J. Electroanal. Chem.*, 2018, **830–831**, 43–49.
174 J. Zhou, R. Li, X. Fan, Y. Chen, R. Han, W. Li, J. Zheng, B. Wang and X. Li, *Energy Environ. Sci.*, 2014, **7**, 2715–2724.
175 Y. X. Yin, S. Xin, Y. G. Guo and L. J. Wan, *Angew. Chem., Int. Ed.*, 2013, **52**, 13186–13200.
176 Q. Pang, X. Liang, C. Y. Kwok and L. F. Nazar, *Nat. Energy*, 2016, **1**, 16132.
177 S. Bai, X. Liu, K. Zhu, S. Wu and H. Zhou, *Nat. Energy*, 2016, **1**, 16094.
178 H. Jiang, X.-C. Liu, Y. Wu, Y. Shu, X. Gong, F.-S. Ke and H. Deng, *Angew. Chem., Int. Ed.*, 2018, **57**, 3916–3921.
179 Y. Mao, G. Li, Y. Guo, Z. Li, C. Liang, X. Peng and Z. Lin, *Nat. Commun.*, 2017, **8**, 14628.
180 T. Pan, Z. Li, Q. He, X. Xu, L. He, J. Meng, C. Zhou, Y. Zhao and L. Mai, *Energy Storage Mater.*, 2019, **23**, 55–61.
181 Z. Zhao, S. Wang, R. Liang, Z. Li, Z. Shi and G. Chen, *J. Mater. Chem. A*, 2014, **2**, 13509–13512.
182 J. Zhou, R. Li, X. Fan, Y. Chen, R. Han, W. Li, J. Zheng, B. Wang and X. Li, *Energy Environ. Sci.*, 2014, **7**, 2715–2724.
183 G. Fang, J. Zhou, A. Pan and S. Liang, *ACS Energy Lett.*, 2018, **3**, 2480–2501.
184 Y. Li, J. Fu, C. Zhong, T. Wu, Z. Chen, W. Hu, K. Amine and J. Lu, *Adv. Energy Mater.*, 2019, **9**, 1802605.
185 D. Selvakumaran, A. Pan, S. Liang and G. Cao, *J. Mater. Chem. A*, 2019, **7**, 18209–18236.
186 M. Song, H. Tan, D. Chao and H. J. Fan, *Adv. Funct. Mater.*, 2018, **28**, 1802564.
187 Y. Fu, Q. Wei, G. Zhang, X. Wang, J. Zhang, Y. Hu, D. Wang, L. Zuin, T. Zhou, Y. Wu and S. Sun, *Adv. Energy Mater.*, 2018, **8**, 1801445.
188 M. Li, J. Meng, Q. Li, M. Huang, X. Liu, K. A. Owusu, Z. Liu and L. Mai, *Adv. Funct. Mater.*, 2018, **28**, 1802016.
189 W. Liu, Y. Mi, Z. Weng, Y. Zhong, Z. Wu and H. Wang, *Chem. Sci.*, 2017, **8**, 4285–4291.
190 L. Wang, Y. Han, X. Feng, J. Zhou, P. Qi and B. Wang, *Coord. Chem. Rev.*, 2016, **307**, 361–381.
191 K. M. Choi, H. M. Jeong, J. H. Park, Y. B. Zhang, J. K. Kang and O. M. Yaghi, *ACS Nano*, 2014, **8**, 7451–7457.
192 S. D. Worrall, H. Mann, A. Rogers, M. A. Bissett, M. P. Attfield and R. A. W. Dryfe, *Electrochim. Acta*, 2016, **197**, 228–240.
193 J. Xu, S. Liu and Y. Liu, *RSC Adv.*, 2016, **6**, 52137–52142.
194 W. Zeng, L. Wang, H. Shi, G. Zhang, K. Zhang, H. Zhang, F. Gong, T. Wang and H. Duan, *J. Mater. Chem. A*, 2016, **4**, 8233–8241.
195 Y. Zhou, Z. Mao, W. Wang, Z. Yang and X. Liu, *ACS Appl. Mater. Interfaces*, 2016, **8**, 28904–28916.
196 P. Wen, P. Gong, J. Sun, J. Wang and S. Yang, *J. Mater. Chem. A*, 2015, **3**, 13874–13883.
197 P. Srimuk, S. Luanwuthi, A. Krittayavathananon and M. Sawangphruk, *Electrochim. Acta*, 2015, **157**, 69–77.
198 L. Wang, X. Feng, L. Ren, Q. Piao, J. Zhong, Y. Wang, H. Li, Y. Chen and B. Wang, *J. Am. Chem. Soc.*, 2015, **137**, 4920–4923.
199 D. K. Nguyen, I. M. Schepisi and F. Z. Amir, *Chem. Eng. J.*, 2019, **378**, 122150.
200 R. Hou, M. Miao, Q. Wang, T. Yue, H. Liu, H. S. Park, K. Qi and B. Y. Xia, *Adv. Energy Mater.*, 2019, **9**, 1901892.
201 Q. Weng, X. Wang, X. Wang, C. Zhang, X. Jiang, Y. Bando and D. Golberg, *J. Mater. Chem. A*, 2015, **3**, 3097–3102.

202 S. Jin, *ACS Energy Lett.*, 2019, **4**, 1443–1445.
203 A. Mahmood, W. Guo, H. Tabassum and R. Zou, *Adv. Energy Mater.*, 2016, **6**, 1600423.
204 K. Rui, G. Zhao, Y. Chen, Y. Lin, Q. Zhou, J. Chen, J. Zhu, W. Sun, W. Huang and S. X. Dou, *Adv. Funct. Mater.*, 2018, **28**, 1801554.
205 L. Wang, Y. Wu, R. Cao, L. Ren, M. Chen, X. Feng, J. Zhou and B. Wang, *ACS Appl. Mater. Interfaces*, 2016, **8**, 16736–16743.
206 L. Ye, J. Liu, Y. Gao, C. Gong, M. Addicoat, T. Heine, C. Wöll and L. Sun, *J. Mater. Chem. A*, 2016, **4**, 15320–15326.
207 Y. Xue, S. Zheng, H. Xue and H. Pang, *J. Mater. Chem. A*, 2019, **7**, 7301–7327.
208 B. Jia, Z. Xue, Q. Liu, Q. Liu, K. Liu, M. Liu, T.-S. Chan, Y. Li, Z. Li, C.-Y. Su and G. Li, *J. Mater. Chem. A*, 2019, **7**, 15073–15078.
209 T. Y. Ma, S. Dai, M. Jaroniec and S. Z. Qiao, *J. Am. Chem. Soc.*, 2014, **136**, 13925–13931.
210 J. Chen, P. Zhuang, Y. Ge, H. Chu, L. Yao, Y. Cao, Z. Wang, M. O. L. Chee, P. Dong, J. Shen, M. Ye and P. M. Ajayan, *Adv. Funct. Mater.*, 2019, **29**, 1903875.
211 N. Kornienko, Y. Zhao, C. S. Kley, C. Zhu, D. Kim, S. Lin, C. J. Chang, O. M. Yaghi and P. Yang, *J. Am. Chem. Soc.*, 2015, **137**, 14129–14135.
212 B. Zhang, Z. Qi, Z. Wu, Y. H. Lui, T.-H. Kim, X. Tang, L. Zhou, W. Huang and S. Hu, *ACS Energy Lett.*, 2018, **4**, 328–336.
213 F. Bu, W. Chen, J. Gu, P. O. Agboola, N. F. Al-Khalli, I. Shakir and Y. Xu, *Chem. Sci.*, 2018, **9**, 7009–7016.
214 R. Wang, J. Cao, S. Cai, X. Yan, J. Li, W. M. Yourey, W. Tong and H. Tang, *ACS Appl. Energy Mater.*, 2018, **1**, 1060–1068.
215 X. Xu, F. Nosheen and X. Wang, *Chem. Mater.*, 2016, **28**, 6313–6320.
216 X. Huang, X. Xu, C. Li, D. Wu, D. Cheng and D. Cao, *Adv. Energy Mater.*, 2019, **9**, 1803970.
217 T. Liu, P. Li, N. Yao, G. Cheng, S. Chen, W. Luo and Y. Yin, *Angew. Chem., Int. Ed.*, 2019, **58**, 4679–4684.
218 X. Sun, S. Sun, S. Gu, Z. Liang, J. Zhang, Y. Yang, Z. Deng, P. Wei, J. Peng, Y. Xu, C. Fang, Q. Li, J. Han, Z. Jiang and Y. Huang, *Nano Energy*, 2019, **61**, 245–250.
219 J. Wu, H. Zhou, Q. Li, M. Chen, J. Wan, N. Zhang, L. Xiong, S. Li, B. Y. Xia, G. Feng, M. Liu and L. Huang, *Adv. Energy Mater.*, 2019, **9**, 1900149.
220 L. Zhao, B. Dong, S. Li, L. Zhou, L. Lai, Z. Wang, S. Zhao, M. Han, K. Gao, M. Lu, X. Xie, B. Chen, Z. Liu, X. Wang, H. Zhang, H. Li, J. Liu, H. Zhang, X. Huang and W. Huang, *ACS Nano*, 2017, **11**, 5800–5807.
221 S. Fu, C. Zhu, J. Song, D. Du and Y. Lin, *Adv. Energy Mater.*, 2017, **7**, 1700363.
222 C. Zhu, S. Fu, Q. Shi, D. Du and Y. Lin, *Angew. Chem., Int. Ed.*, 2017, **56**, 13944–13960.
223 T. Liu, P. Li, N. Yao, T. Kong, G. Cheng, S. Chen and W. Luo, *Adv. Mater.*, 2019, **31**, e1806672.
224 G. Jia, W. Zhang, G. Z. Fan, Z. S. Li, D. G. Fu, W. C. Hao, C. W. Yuan and Z. G. Zou, *Angew. Chem., Int. Ed.*, 2017, **56**, 13781–13785.
225 X. Wang, Z. Ma, L. Chai, L. Xu, Z. Zhu, Y. Hu, J. Qian and S. Huang, *Carbon*, 2019, **141**, 643–651.
226 X. Liu, K. Ni, B. Wen, C. Niu, J. Meng, R. Guo, Q. Li, J. Li, Y. Zhu, X. Wu, D. Zhao and L. Mai, *J. Mater. Chem. A*, 2018, **6**, 17874–17881.
227 C. Guan, A. Sumboja, W. Zang, Y. Qian, H. Zhang, X. Liu, Z. Liu, D. Zhao, S. J. Pennycook and J. Wang, *Energy Storage Mater.*, 2019, **16**, 243–250.
228 S. Roy, Z. Huang, A. Bhunia, A. Castner, A. Kumar Gupta, X. Zou and S. Ott, *J. Am. Chem. Soc.*, 2019, **141**, 15942–15950.
229 I. Hod, P. Deria, W. Bury, J. E. Mondloch, C. W. Kung, M. So, M. D. Sampson, A. W. Peters, C. P. Kubiak, O. K. Farha and J. T. Hupp, *Nat. Commun.*, 2015, **6**, 8304.
230 W. Cheng, X. Zhao, H. Su, F. Tang, W. Che, H. Zhang and Q. Liu, *Nat. Energy*, 2019, **4**, 115–122.
231 O. Shekhah, J. Liu, R. A. Fischer and C. Woll, *Chem. Soc. Rev.*, 2011, **40**, 1081–1106.
232 J. Y. Lin, *Science*, 2016, **353**, 121–122.
233 H. Furukawa, K. E. Cordova, M. O'Keeffe and O. M. Yaghi, *Science*, 2013, **341**, 1230444.
234 X. Zhao, Y. Wang, D. S. Li, X. Bu and P. Feng, *Adv. Mater.*, 2018, **30**, 1705189.
235 T. Ben, C. Lu, C. Pei, S. Xu and S. Qiu, *Chem. – Eur. J.*, 2012, **18**, 10250–10253.
236 A. Cadiau, K. Adil, P. M. Bhatt, Y. Belmabkhout and M. Eddaoudi, *Science*, 2016, **353**, 137–140.
237 S. Castarlenas, C. Téllez and J. Coronas, *J. Membr. Sci.*, 2017, **526**, 205–211.
238 S. Qiu, M. Xue and G. Zhu, *Chem. Soc. Rev.*, 2014, **43**, 6116–6140.
239 N. Kosinov, J. Gascon, F. Kapteijn and E. J. M. Hensen, *J. Membr. Sci.*, 2016, **499**, 65–79.
240 H. T. Kwon and H. K. Jeong, *Chem. Commun.*, 2013, **49**, 3854–3856.
241 S. Lawson, A. A. Rownaghi and F. Rezaei, *Energy Technol.*, 2018, **6**, 694–701.
242 D. Nagaraju, D. G. Bhagat, R. Banerjee and U. K. Kharul, *J. Mater. Chem. A*, 2013, **1**, 8828–8835.
243 F. Rezaei, S. Lawson, H. Hosseini, H. Thakkar, A. Hajari, S. Monjezi and A. A. Rownaghi, *Chem. Eng. J.*, 2017, **313**, 1346–1353.
244 Z. Xie, J. Yang, J. Wang, J. Bai, H. Yin, B. Yuan, J. Lu, Y. Zhang, L. Zhou and C. Duan, *Chem. Commun.*, 2012, **48**, 5977–5979.
245 X. L. Cui, K. J. Chen, H. B. Xing, Q. W. Yang, R. Krishna, Z. B. Bao, H. Wu, W. Zhou, X. L. Dong, Y. Han, B. Li, Q. L. Ren, M. J. Zaworotko and B. L. Chen, *Science*, 2016, **353**, 141–144.
246 K. Tao, L. J. Cao, Y. C. Lin, C. L. Kong and L. Chen, *J. Mater. Chem. A*, 2013, **1**, 13046–13049.
247 Y. S. Li, H. Bux, A. Feldhoff, G. L. Li, W. S. Yang and J. Caro, *Adv. Mater.*, 2010, **22**, 3322–3326.
248 J. Yao, D. Dong, D. Li, L. He, G. Xu and H. Wang, *Chem. Commun.*, 2011, **47**, 2559–2561.
249 X. Dong, K. Huang, S. Liu, R. Ren, W. Jin and Y. S. Lin, *J. Mater. Chem.*, 2012, **22**, 19222.
250 Y. Hu, X. Dong, J. Nan, W. Jin, X. Ren, N. Xu and Y. M. Lee, *Chem. Commun.*, 2011, **47**, 737–739.

251 Z. Zhao, X. Ma, Z. Li and Y. S. Lin, *J. Membr. Sci.*, 2011, **382**, 82–90.
252 Y. Yoo, Z. Lai and H.-K. Jeong, *Microporous Mesoporous Mater.*, 2009, **123**, 100–106.
253 D.-J. Lee, Q. Li, H. Kim and K. Lee, *Microporous Mesoporous Mater.*, 2012, **163**, 169–177.
254 J. Nan, X. Dong, W. Wang, W. Jin and N. Xu, *Langmuir*, 2011, **27**, 4309–4312.
255 S. R. Venna and M. A. Carreon, *J. Am. Chem. Soc.*, 2010, **132**, 76–78.
256 Y. Liu, E. Hu, E. A. Khan and Z. Lai, *J. Membr. Sci.*, 2010, **353**, 36–40.
257 S. Aguado, C.-H. Nicolas, V. Moizan-Baslé, C. Nieto, H. Amrouche, N. Bats, N. Audebrand and D. Farrusseng, *New J. Chem.*, 2011, **35**, 41–44.
258 Z. Xie, T. Li, N. L. Rosi and M. A. Carreon, *J. Mater. Chem. A*, 2014, **2**, 1239–1241.
259 N. Hara, M. Yoshimune, H. Negishi, K. Haraya, S. Hara and T. Yamaguchi, *J. Membr. Sci.*, 2014, **450**, 215–223.
260 D. Liu, X. Ma, H. Xi and Y. S. Lin, *J. Membr. Sci.*, 2014, **451**, 85–93.
261 H. T. Kwon and H. K. Jeong, *J. Am. Chem. Soc.*, 2013, **135**, 10763–10768.
262 Z. Song, F. Qiu, E. W. Zaia, Z. Wang, M. Kunz, J. Guo, M. Brady, B. Mi and J. J. Urban, *Nano Lett.*, 2017, **17**, 6752–6758.
263 S. Zhou, Y. Y. Wei, L. B. Li, Y. F. Duan, Q. Q. Hou, L. L. Zhang, L. X. Ding, J. Xue, H. H. Wang and J. Caro, *Sci. Adv.*, 2018, **4**, eaau1393.
264 A. Schoedel, Z. Ji and O. M. Yaghi, *Nat. Energy*, 2016, **1**, 16034.
265 Y. He, W. Zhou, G. Qian and B. Chen, *Chem. Soc. Rev.*, 2014, **43**, 5657–5678.
266 A. J. Howarth, Y. Liu, P. Li, Z. Li, T. C. Wang, J. T. Hupp and O. K. Farha, *Nat. Rev. Mater.*, 2016, **1**, 15018.
267 B. Li, H.-M. Wen, W. Zhou, J. Q. Xu and B. Chen, *Chem*, 2016, **1**, 557–580.
268 X. Zhao, B. Xiao, A. J. Fletcher, K. M. Thomas, D. Bradshaw and M. J. Rosseinsky, *Science*, 2004, **306**, 1012–1015.
269 B. Li, H.-M. Wen, H. Wang, H. Wu, T. Yildirim, W. Zhou and B. Chen, *Energy Environ. Sci.*, 2015, **8**, 2504–2511.
270 J. G. Hinman, J. G. Turner, D. M. Hofmann and C. J. Murphy, *Chem. Mater.*, 2018, **30**, 7255–7261.
271 J. Liu, D. M. Strachan and P. K. Thallapally, *Chem. Commun.*, 2014, **50**, 466–468.
272 C. Zlotea, R. Campesi, F. Cuevas, E. Leroy, P. Dibandjo, C. Volkringer, T. Loiseau, G. Ferey and M. Latroche, *J. Am. Chem. Soc.*, 2010, **132**, 2991–2997.
273 Y. E. Cheon and M. P. Suh, *Angew. Chem., Int. Ed.*, 2009, **48**, 2899–2903.
274 Y. Nanba, T. Tsutsumi, T. Ishimoto and M. Koyama, *J. Phys. Chem. C*, 2017, **121**, 14611–14617.
275 Z. Li, R. Yu, J. Huang, Y. Shi, D. Zhang, X. Zhong, D. Wang, Y. Wu and Y. Li, *Nat. Commun.*, 2015, **6**, 8248.
276 O. Shekhah, L. Fu, R. Sougrat, Y. Belmabkhout, A. J. Cairns, E. P. Giannelis and M. Eddaoudi, *Chem. Commun.*, 2012, **48**, 11434–11436.
277 K. Wenderich and G. Mul, *Chem. Rev.*, 2016, **116**, 14587–14619.
278 Y. Horiuchi, T. Toyao, M. Takeuchi, M. Matsuoka and M. Anpo, *Phys. Chem. Chem. Phys.*, 2013, **15**, 13243–13253.
279 Y. Li, H. Xu, S. Ouyang and J. Ye, *Phys. Chem. Chem. Phys.*, 2016, **18**, 7563–7572.
280 M. A. Nasalevich, M. van der Veen, F. Kapteijn and J. Gascon, *CrystEngComm*, 2014, **16**, 4919–4926.
281 L. J. Shen, R. W. Liang and L. Wu, *Chin. J. Catal.*, 2015, **36**, 2071–2088.
282 C.-C. Wang, J.-R. Li, X.-L. Lv, Y.-Q. Zhang and G. Guo, *Energy Environ. Sci.*, 2014, **7**, 2831–2867.
283 J.-L. Wang, C. Wang and W. Lin, *ACS Catal.*, 2012, **2**, 2630–2640.
284 S. Wang and X. Wang, *Small*, 2015, **11**, 3097–3112.
285 W. Wang, X. Xu, W. Zhou and Z. Shao, *Adv. Sci.*, 2017, **4**, 1600371.
286 L. Zhang, P. Cui, H. Yang, J. Chen, F. Xiao, Y. Guo, Y. Liu, W. Zhang, F. Huo and B. Liu, *Adv. Sci.*, 2016, **3**, 1500243.
287 T. Zhang and W. Lin, *Chem. Soc. Rev.*, 2014, **43**, 5982–5993.
288 L. Shi, T. Wang, H. Zhang, K. Chang, X. Meng, H. Liu and J. Ye, *Adv. Sci.*, 2015, **2**, 1500006.
289 C. Gomes Silva, I. Luz, F. X. Llabres i Xamena, A. Corma and H. Garcia, *Chem. – Eur. J.*, 2010, **16**, 11133–11138.
290 Y. Kataoka, K. Sato, Y. Miyazaki, K. Masuda, H. Tanaka, S. Naito and W. Mori, *Energy Environ. Sci.*, 2009, **2**, 397–400.
291 S. Pullen, H. Fei, A. Orthaber, S. M. Cohen and S. Ott, *J. Am. Chem. Soc.*, 2013, **135**, 16997–17003.
292 S. Wang, W. Yao, J. Lin, Z. Ding and X. Wang, *Angew. Chem., Int. Ed.*, 2014, **53**, 1034–1038.
293 Q. Liu, Z.-X. Low, L. Li, A. Razmjou, K. Wang, J. Yao and H. Wang, *J. Mater. Chem. A*, 2013, **1**, 11563–11569.
294 F. Ke, L. Wang and J. Zhu, *Nano Res.*, 2015, **8**, 1834–1846.
295 D. Wang and Z. Li, *J. Catal.*, 2016, **342**, 151–157.
296 Z. Gu, L. Chen, B. Duan, Q. Luo, J. Liu and C. Duan, *Chem. Commun.*, 2016, **52**, 116–119.
297 Z.-C. Kong, J.-F. Liao, Y.-J. Dong, Y.-F. Xu, H.-Y. Chen, D.-B. Kuang and C.-Y. Su, *ACS Energy Lett.*, 2018, **3**, 2656–2662.
298 X. Fang, Q. Shang, Y. Wang, L. Jiao, T. Yao, Y. Li, Q. Zhang, Y. Luo and H. L. Jiang, *Adv. Mater.*, 2018, **30**, 1705112.
299 J. He, J. Wang, Y. Chen, J. Zhang, D. Duan, Y. Wang and Z. Yan, *Chem. Commun.*, 2014, **50**, 7063–7066.
300 H. Zhao, L. Qian, H. Lv, Y. Wang and G. Zhao, *ChemCatChem*, 2015, **7**, 4148–4155.
301 M. Zeng, Z. Chai, X. Deng, Q. Li, S. Feng, J. Wang and D. Xu, *Nano Res.*, 2016, **9**, 2729–2734.
302 H. Fei, M. D. Sampson, Y. Lee, C. P. Kubiak and S. M. Cohen, *Inorg. Chem.*, 2015, **54**, 6821–6828.
303 Q. Lan, Z. M. Zhang, C. Qin, X. L. Wang, Y. G. Li, H. Q. Tan and E. B. Wang, *Chem. – Eur. J.*, 2016, **22**, 15513–15520.
304 H. Chen, Z.-G. Gu, S. Mirza, S.-H. Zhang and J. Zhang, *J. Mater. Chem. A*, 2018, **6**, 7175–7181.
305 J. Lei, R. Qian, P. Ling, L. Cui and H. Ju, *TrAC-Trend Anal. Chem.*, 2014, **58**, 71–78.
306 Q. Qiu, H. Chen, Y. Wang and Y. Ying, *Coord. Chem. Rev.*, 2019, **387**, 60–78.
307 I. Ellern, P. Hesketh, V. Stavila, J.-H. Lee, M. Allendorf, A. Venkatasubramanian and A. Robinson, *Micro Nano Lett.*, 2013, **8**, 766–769.

308 H. Guo, S. Zhu, D. Cai and C. Liu, *Inorg. Chem. Commun.*, 2014, **41**, 29–32.
309 X. Liu, W. Fu and E. Bouwman, *Chem. Commun.*, 2016, **52**, 6926–6929.
310 A. L. Robinson, V. Stavila, T. R. Zeitler, M. I. White, S. M. Thornberg, J. A. Greathouse and M. D. Allendorf, *Anal. Chem.*, 2012, **84**, 7043–7051.
311 P. Á. Szilágyi, R. J. Westerwaal, R. van de Krol, H. Geerlings and B. Dam, *J. Mater. Chem. C*, 2013, **1**, 8146–8155.
312 M. S. Yao, W. X. Tang, G. E. Wang, B. Nath and G. Xu, *Adv. Mater.*, 2016, **28**, 5229–5234.
313 K. Sugikawa, S. Nagata, Y. Furukawa, K. Kokado and K. Sada, *Chem. Mater.*, 2013, **25**, 2565–2570.
314 L. E. Kreno, J. T. Hupp and R. P. Van Duyne, *Anal. Chem.*, 2010, **82**, 8042–8046.
315 W. Wang, S. Wang, X. Ma and J. Gong, *Chem. Soc. Rev.*, 2011, **40**, 3703–3727.
316 S. Kattel, P. J. Ramirez, J. G. Chen, J. A. Rodriguez and P. Liu, *Science*, 2017, **355**, 1296–1299.
317 M. Zhao, K. Yuan, Y. Wang, G. Li, J. Guo, L. Gu, W. Hu, H. Zhao and Z. Tang, *Nature*, 2016, **539**, 76–80.
318 H. Pan, X. Li, D. Zhang, Y. Guan and P. Wu, *J. Mol. Catal. A: Chem.*, 2013, **377**, 108–114.
319 D. Zhang, Y. Guan, E. J. M. Hensen, L. Chen and Y. Wang, *Catal. Commun.*, 2013, **41**, 47–51.
320 P. Wang, J. Zhao, X. Li, Y. Yang, Q. Yang and C. Li, *Chem. Commun.*, 2013, **49**, 3330–3332.
321 C. J. Stephenson, J. T. Hupp and O. K. Farha, *Inorg. Chem. Front.*, 2015, **2**, 448–452.
322 C. H. Kuo, Y. Tang, L. Y. Chou, B. T. Sneed, C. N. Brodsky, Z. Zhao and C. K. Tsung, *J. Am. Chem. Soc.*, 2012, **134**, 14345–14348.
323 M. Sabo, A. Henschel, H. Fröde, E. Klemm and S. Kaskel, *J. Mater. Chem.*, 2007, **17**, 3827–3832.
324 Y. Zhao, J. Zhang, J. Song, J. Li, J. Liu, T. Wu, P. Zhang and B. Han, *Green Chem.*, 2011, **13**, 2078–2082.
325 M. X. Wu and Y. W. Yang, *Adv. Mater.*, 2017, **29**, 1606134.
326 P. Horcajada, T. Chalati, C. Serre, B. Gillet, C. Sebrie, T. Baati, J. F. Eubank, D. Heurtaux, P. Clayette, C. Kreuz, J. S. Chang, Y. K. Hwang, V. Marsaud, P. N. Bories, L. Cynober, S. Gil, G. Ferey, P. Couvreur and R. Gref, *Nat. Mater.*, 2010, **9**, 172–178.
327 S. Li, M. Dharmarwardana, R. P. Welch, Y. Ren, C. M. Thompson, R. A. Smaldone and J. J. Gassensmith, *Angew. Chem., Int. Ed.*, 2016, **55**, 10691–10696.
328 W. Liang, R. Ricco, N. K. Maddigan, R. P. Dickinson, H. Xu, Q. Li, C. J. Sumby, S. G. Bell, P. Falcaro and C. J. Doonan, *Chem. Mater.*, 2018, **30**, 1069–1077.
329 H. An, M. Li, J. Gao, Z. Zhang, S. Ma and Y. Chen, *Coord. Chem. Rev.*, 2019, **384**, 90–106.
330 T. H. Wei, S. H. Wu, Y. D. Huang, W. S. Lo, B. P. Williams, S. Y. Chen, H. C. Yang, Y. S. Hsu, Z. Y. Lin, X. H. Chen, P. E. Kuo, L. Y. Chou, C. K. Tsung and F. K. Shieh, *Nat. Commun.*, 2019, **10**, 5002.
331 W. Cai, J. Wang, C. Chu, W. Chen, C. Wu and G. Liu, *Adv. Sci.*, 2019, **6**, 1801526.
332 X. Y. Zhu, J. L. Gu, Y. Wang, B. Li, Y. S. Li, W. R. Zhao and J. L. Shi, *Chem. Commun.*, 2014, **50**, 8779–8782.
333 D. Wang, J. Zhou, R. Chen, R. Shi, G. Xia, S. Zhou, Z. Liu, N. Zhang, H. Wang, Z. Guo and Q. Chen, *Biomaterials*, 2016, **107**, 88–101.
334 R. Bian, T. Wang, L. Zhang, L. Li and C. Wang, *Biomater. Sci.*, 2015, **3**, 1270–1278.
335 Z. Ji, H. Zhang, H. Liu, O. M. Yaghi and P. Yang, *Proc. Natl. Acad. Sci. U. S. A.*, 2018, **115**, 10582–10587.
336 K. Liang, J. J. Richardson, C. J. Doonan, X. Mulet, Y. Ju, J. Cui, F. Caruso and P. Falcaro, *Angew. Chem., Int. Ed.*, 2017, **56**, 8510–8515.
337 H. S. Cho, J. Yang, X. Gong, Y. B. Zhang, K. Momma, B. M. Weckhuysen, H. Deng, J. K. Kang, O. M. Yaghi and O. Terasaki, *Nat. Chem.*, 2019, **11**, 562–570.
338 H. Zhang, J. Hou, Y. Hu, P. Wang, R. Ou, L. Jiang, J. Z. Liu, B. D. Freeman, A. J. Hill and H. Wang, *Sci. Adv.*, 2018, **4**, eaaq0066.
339 P. Li, J. Li, X. Feng, J. Li, Y. Hao, J. Zhang, H. Wang, A. Yin, J. Zhou, X. Ma and B. Wang, *Nat. Commun.*, 2019, **10**, 2177.
340 X. Ma, Y. Chai, P. Li and B. Wang, *Acc. Chem. Res.*, 2019, **52**, 1461–1470.
341 S. K. Elsaidi, M. A. Sinnwell, D. Banerjee, A. Devaraj, R. K. Kukkadapu, T. C. Droubay, Z. Nie, L. Kovarik, M. Vijayakumar, S. Manandhar, M. Nandasiri, B. P. McGrail and P. K. Thallapally, *Nano Lett.*, 2017, **17**, 6968–6973.
342 H. K. Arslan, O. Shekhah, J. Wohlgemuth, M. Franzreb, R. A. Fischer and C. Wöll, *Adv. Funct. Mater.*, 2011, **21**, 4228–4231.
343 F. Maya, C. Palomino Cabello, S. Clavijo, J. M. Estela, V. Cerda and G. Turnes Palomino, *Chem. Commun.*, 2015, **51**, 8169–8172.